

# 学位論文

Carrier dynamics in graphene on SiC  
studied by time-resolved photoemission spectroscopy

(時間分解光電子分光法による SiC 基板上  
グラフェンのキャリアダイナミクス研究)

平成 29 年度 12 月博士 (理学) 申請

東京大学大学院理学系研究科

物理学専攻 染谷隆史

# Abstract

Graphene, a two-dimensional material composed of carbon honeycomb structure, possesses remarkable electric and optical properties such as broadband photoabsorption, high carrier mobility and ultrafast optical response. These anomalous properties stem from massless Dirac Fermions showing a linear energy-momentum dispersion called “Dirac cone”. Since a recent discovery of graphene, studies of fundamental properties of graphene have been always center of the attention in the wide range of academic fields. Owing to accumulation of many researches, some graphene-based devices started to be used in a commercial way. An opto-electronic application of graphene is also highly promising, but a comprehensive understanding of carrier dynamics in graphene is still missing.

In the present study, we systematically studied carrier dynamics in graphene on SiC substrate by time-resolved photoemission spectroscopy. First, a characteristic carrier scattering of Dirac Fermions was examined for the first time in graphene on Si-face SiC(0001) surface, which shows strong electron doping and electron-electron scattering in the time scale of several hundred femtoseconds. Furthermore, electron-phonon scattering and electron-defect scattering are circumstantially investigated in graphene on C-face SiC(0001). A combination technique of time-resolved photoemission spectroscopy and numerical model analysis revealed the whole relaxation picture within the time scale of femtoseconds to several picoseconds. Finally, charge transfer dynamics at graphene/SiC interface and the influence of the interface structure was examined up to sub-microsecond region utilizing a laser-pump synchrotron radiation-probe time-resolved photoemission measurement.

As a consequence of a series of time-resolved photoemission measurements, we clearly identified individual relaxation pathways and uncover the overall time structure of carrier dynamics in graphene/SiC system ranging from femtosecond to microsecond time scale.

# Contents

|          |  |           |
|----------|--|-----------|
| <b>1</b> | <b>Introduction</b>  | <b>1</b>  |
| 1.1      | Background . . . . .                                       | 1         |
| 1.2      | Purpose of the present study . . . . .                     | 2         |
| 1.3      | Outline . . . . .  | 3         |
| <b>2</b> | <b>Fundamental properties of graphene</b>                  | <b>5</b>  |
| 2.1      | Crystal structure . . . . .                                | 5         |
| 2.2      | Electronic structure . . . . .                             | 6         |
| 2.2.1    | Monolayer graphene . . . . .                               | 6         |
| 2.2.2    | Bilayer graphene . . . . .                                 | 11        |
| 2.3      | Optical properties . . . . .                               | 14        |
| 2.4      | Epitaxial graphene on SiC substrate . . . . .              | 14        |
| 2.4.1    | Epitaxial graphene on Si-face SiC(0001) . . . . .          | 15        |
| 2.4.2    | Epitaxial graphene on C-face SiC(000 $\bar{1}$ ) . . . . . | 19        |
| 2.4.3    | Quasi free-standing epitaxial graphene . . . . .           | 20        |
| <b>3</b> | <b>Experimental method</b>                                 | <b>23</b> |
| 3.1      | Measurement . . . . .                                      | 23        |
| 3.1.1    | Photoemission spectroscopy . . . . .                       | 23        |
| 3.1.2    | Angle-resolved photoemission spectroscopy . . . . .        | 27        |
| 3.1.3    | Time-resolved photoemission spectroscopy . . . . .         | 30        |
| 3.2      | Light sources . . . . .                                    | 31        |
| 3.2.1    | High-harmonic generation . . . . .                         | 31        |

|          |  |           |
|----------|--|-----------|
| 3.2.2    | Synchrotron radiation . . . . .  | 32        |
| 3.3      | Measurement systems . . . . .  | 33        |
| 3.3.1    | HHG beamline . . . . .   | 34        |
| 3.3.2    | SR beamline . . . . .  | 37        |
| <b>4</b> | <b>Ultrafast carrier dynamics in epitaxial graphene on Si-face SiC(0001)</b>                   | <b>39</b> |
| 4.1      | Introduction . . . . .   | 39        |
| 4.2      | Experimental . . . . .   | 40        |
| 4.3      | Results and discussion . . . . .   | 41        |
| 4.3.1    | Space Charge Effect . . . . .  | 41        |
| 4.3.2    | Time evolution of the electronic temperature . . . . .   | 42        |
| 4.3.3    | Transient chemical potential . . . . .   | 43        |
| 4.3.4    | Carrier multiplication in n-type monolayer graphene . . . . .                                  | 45        |
| 4.4      | Conclusion . . . . .   | 47        |
| <b>5</b> | <b>Ultrafast carrier dynamics in epitaxial graphene on C-face SiC(000<math>\bar{1}</math>)</b> | <b>49</b> |
| 5.1      | Introduction . . . . .   | 49        |
| 5.2      | Experimental . . . . .   | 51        |
| 5.3      | Results and discussion . . . . .   | 52        |
| 5.3.1    | Transient hot carrier distribution in the Dirac cone . . . . .                                 | 52        |
| 5.3.2    | Relaxation model for electron-phonon and electron-defect scatterings . . . . .                 | 53        |
| 5.3.3    | Suppression of supercollision carrier cooling process . . . . .                                | 57        |
| 5.3.4    | Carrier cooling mechanism in high mobility graphene . . . . .                                  | 58        |
| 5.4      | Conclusion . . . . .   | 61        |
| <b>6</b> | <b>Charge transfer dynamics at graphene/SiC interface</b>                                      | <b>63</b> |
| 6.1      | Introduction . . . . .   | 63        |
| 6.2      | Experimental . . . . .   | 64        |
| 6.3      | Results and discussion . . . . .   | 65        |
| 6.3.1    | Surface photovoltage effect in Si-face and C-face graphene . . . . .                           | 65        |

|          |  |           |
|----------|--|-----------|
| 6.3.2    | Analysis by thermionic emission model . . . . .                  | 66        |
| 6.3.3    | Comparison of carrier lifetime and effect of the interface layer | 68        |
| 6.4      | Conclusion . . . . .   | 70        |
| <b>7</b> | <b>Summary and future prospect</b>                               | <b>71</b> |
| 7.1      | Summary . . . . .  | 71        |
| 7.2      | Future prospect . . . . .  | 72        |
| <b>A</b> | <b>Electronic temperature fitting</b>                            | <b>75</b> |
| <b>B</b> | <b>Derivation of the supercollision cooling rate</b>             | <b>77</b> |
| <b>C</b> | <b>Details of the fitting parameters</b>                         | <b>79</b> |
| <b>D</b> | <b>Long-delay data</b>   | <b>81</b> |

## Acknowledgments

First of all, I would like to express my greatest appreciation to my supervisor, **Prof. Iwao Matsuda** for everything he has done for me. During the last five years, I was able to have many scientific experiences, such as participation of experiments at overseas synchrotron radiation and X-ray free electron laser facilities. I am grateful that he has given me these opportunities.

I would like to thank **Dr. Susumu Yamamoto** for kindly answering many of my questions. He also taught me a lot of experimental techniques during staying at SPring-8.

I would like to thank **Prof. Hirokazu Fukidome**, **Prof. Maki Suemitsu** and their group members **Mr. Kazutoshi Funakubo**, **Mr. Ryota Suto**, **Mr. Keiichiro Tashima**, **Ms. Mika Hasegawa**, **Mr. Nobuaki Ohtani**, **Mr. Norifumi Endoh** and **Mr. Kensuke Takahashi** for collaboration researches on graphene and always providing me with high quality graphene samples.

I would like to thank **Prof. Shik Shin** and **Prof. Kozo Okazaki** for giving me many opportunities to perform time-resolved photoemission experiments by using “4 gouki”. I also would like to thank **Dr. Yukiaki Ishida**, **Dr. Rikiya Yoshida**, **Dr. Takashi Yamamoto**, **Dr. Takeshi Suzuki**, **Dr. Hakuto Suzuki**, **Mr. Masaru Okada**, **Mr. Yu Ogawa**, **Mr. Shoya Michimae**, **Ms. Mari Watanabe** and other members of Profs. Shin and Okazaki’s laboratory for helping my experiments and working together at 4 gouki.

I would like to thank **Prof. Jiro Itatani**, **Dr. Nobuhisa Ishii** and **Mr. Teruto Kanai** for collaboration research using HHG laser and giving me many pieces of technological advice.

I would like to thank **Prof. Fumio Komori** for fruitful advice at the group seminar and offering me a lot of opportunities to conduct graphene experiments. I also would like to express my gratitude to **Mr. Takushi Imori** for kind help and teaching technological advice to me.

I would like to thank **Dr. Hiroshi Watanabe** for great assistance in constructing a numerical model used in Chapter 5.

I would like to thank **Prof. Yoshihisa Harada, Prof. Hiroki Wadati, Dr. Yasuyuki Hirata, Dr. Jun Miyawaki, Dr. Hideharu Niwa, Dr. Kou Takubo, Dr. Yitao Cui, Dr. Keishi Akada, Dr. Hisao Kiuchi, Dr. kosuke Yamozoe, Mr. Yuichi Yokoyama, Mr. Junki Nakajima, Mr. Tomoyuki Tsuyama, Mr. Haruki Itamoto, Mr. Kohei Yamamoto, Mr. Takanobu Inoue, Mr. Wang Hao, Mr. Tomoyuki Tsukada** for sharing wonderful time at SPring-8.

I would like to thank **Dr. Koichiro Yaji, Mr. Masami Fujisawa** and **Ms. Ayumi Harasawa** for technical supports in Kashiwa and **Ms. Mihoko Araki, Ms. Yuka Kosegawa** in SPring-8.

I would like to thank all the members in group of Prof. Matsuda: **Dr. Ryu Yukawa, Dr. Baojie Feng, Dr. Shingo Yamamoto, Dr. Kubota Yuya, Mr. Kazushi Fujikawa, Dr. Ro-ya Liu, Mr. Kazuma Akikubo, Mr. Suguru Ito** and **Ms. Kaori Takeuchi** for their kind help and advice during the postgraduate course, and sharing pleasurable experiences in my daily life. I would also like to thank secretaries of SOR office: **Ms. Yumiko Aihara, Ms. Motoko Yoshizawa, Ms. Kuniko Ikeda, Ms. Yumiko Tsutsumi, Ms. Yohie Kaneko, Ms. Akiko Someya, Ms. Misa Harada, Ms. Yukimi Yamamoto, Ms. Chiho Hiromoto** and **Ms. Emi Harada** for great assistance in my clerical duties.

Finally, I am deeply grateful to my family for always sporting and encouraging me.

# Chapter 1

## Introduction

### 1.1 Background

Graphene, a two-dimensional carbon sheet, is a material that is the thinnest, lightest, and strongest material with prominent electrical and optical properties. The history of graphene is quite old in the field of theoretical physics. However, experimental studies were launched from 2004, triggered by the first discovery of manufacturing graphene sheet by A. K. Geim and K. S. Novoselov, who were the Nobel Prize winner in 2010 [1]. Since then, many researches have been dedicated to understand fundamental properties of graphene for future device applications.

Opto-electronic device is one of the most promising candidate for graphene application owing to its unique electrical and optical properties. In spite of the growing demand for opto-electronic applications, however, there exist many difficulties for realizing them. For example, understanding of ultrafast phenomena in graphene, such as carrier scatterings, phonon scatterings and charge transfer with other materials is lacking. Moreover, extrinsic effects arising from sample qualities, e.g. defects, strain, carrier doping, substrate etc., further complicate the problem.

Recently, developments in both experimental and fabrication methods allow us to investigate details of carrier dynamics occurring in graphene. Here, I will briefly overview some previous studies.

In 2013, K. J. Tielrooij *et al.* studied carrier-carrier scatterings by performing

visible-pump terahertz (THz)-probe experiment in an n-doped monolayer graphene [2]. They found an anomalous transient absorption in the graphene which shows strong dependence on excitation energies. They concluded that the observed results can be explained by cascade carrier scattering, called “carrier multiplication (CM)”. This is a unique phenomenon in graphene because the linear energy dispersion of graphene enhances carrier-carrier scatterings, resulting in efficient photon-carrier conversion, which is available for photodetectors and photoelectric conversion devices.

In the same year, J. C. Johannsen *et al.* reported the first direct observation of photo-excited carrier dynamics in a p-doped monolayer graphene [3]. They used a combined technique of a pump-probe method and angle-resolved photoemission spectroscopy. However, they could not achieve multiple carrier generation probably due to the excitation energy because fluence were not optimum.

As for a theoretical study, J. C. Song *et al.* pointed out that the presence of defects has significant influence on carrier relaxation dynamics in substrate-supported graphene samples which are usually used in pump-probe experiments [4]. They claimed the importance of defect-mediated carrier scattering, called “supercollision”, giving new insight into carrier relaxation mechanics in graphene.

Until now, the study of carrier dynamics in graphene is only half done; in spite of a number of studies so far, comprehensive understanding of carrier dynamics is still not obtained. For example, there is no consistency among reported relaxation time constant; some studies reported it to be several hundred femtoseconds while others reported one hundred picosecond, which has a difference of several orders of magnitude within these reports.

## 1.2 Purpose of the present study

To comprehensively investigate and give new insight into carrier dynamics in graphene, we systemically studied the carrier dynamics of graphene, especially grown on a SiC substrate. There are two types of graphene samples depending on a grown surface of SiC: (1) graphene grown on SiC(0001), whose top most surface is terminated by Si

atoms (we will refer to it as Si-face graphene in this thesis) and (2) graphene grown on SiC(000 $\bar{1}$ ), whose top most surface is terminated by C atoms (we will refer to it as C-face graphene).

Si-face graphene accompanies a characteristic interface structure during its fabrication process, called “buffer layer”. Due to the presence of a buffer layer at the graphene/SiC interface, excess electrons are transferred from SiC to graphene, resulting in strong n-type doping. Therefore, carrier-carrier scattering plays an important role in relaxation of photo-excited carriers because there are dense electrons near the Fermi level, which can participate in electron-electron scattering.

On the other hand, graphene grown on SiC(000 $\bar{1}$ ) exhibits a nearly ideal graphene feature due to the absence of a buffer layer. In this case, electron-phonon scattering and electron-defect scattering compete as a main relaxation channel. This allows us to access both intrinsic and extrinsic carrier dynamics which has been uncovered by effects of a carrier doping and/or a strain, etc.

Moreover, the presence of the buffer layer affects charge transfer dynamics at graphene/SiC interface which occurs in the photo-excited graphene/SiC system with a time scale of picoseconds to microseconds.

Based on these facts, I set the purposes of the present study as follows:

- (1) observing carrier-carrier scattering in graphene on Si-face SiC(0001) (femtosecond dynamics);
- (2) uncovering whole relaxation dynamics in graphene on C-face SiC(000 $\bar{1}$ ) (femtosecond to picosecond dynamics);
- (3) clarifying the effect of a buffer layer on charge transfer dynamics of photo-excited carriers at graphene/SiC interface (picosecond to microsecond dynamics).

## 1.3 Outline

In this thesis, I will report systematic studies of carrier dynamics in graphene especially grown on a SiC substrate by time-resolved photoemission spectroscopy.

First, fundamental properties of graphene are introduced in Chapter 2.

Chapter 3 overviews experimental techniques used in this thesis.

Chapter 4 describes a first demonstration of a direct observation of photo-excited carrier dynamics in epitaxial graphene on Si-face SiC(0001). By using a high harmonic generation as a probe light, ultrafast carrier dynamics of graphene is revealed within the time scale of several hundreds of femtoseconds.

Detailed mechanism of ultrafast carrier dynamics in graphene on C-face SiC(000 $\bar{1}$ ) is then discussed in Chapter 5. A combination study of time- and angle-resolved photoemission spectroscopy and numerical simulation allows us to access intrinsic and extrinsic relaxation processes individually, which has been a challenging problem so far.

Chapter 6 describes the charge transfer dynamics at graphene/SiC interface. I will report a significant influence of the presence of a buffer layer on carrier recombination processes.

Finally, general overview and future prospect are given in Chapter 7.

# Chapter 2

## Fundamental properties of graphene

### 2.1 Crystal structure

Graphene consists of a two-dimensional (2D) honeycomb lattice of carbon  $sp_2$  network as described in Figure 2-1. A 2D unit cell of graphene involves two carbon atoms, one of which is usually referred to as a site-A carbon and the other is a site-B carbon as illustrated by black and gray circles in Fig. 2-1, respectively. In Fig. 2-1,  $\mathbf{a}_1$  and  $\mathbf{a}_2$  represent the primitive translation vectors with norm  $|\mathbf{a}_{1,2}| = 2.46 \text{ \AA}$  and  $\mathbf{t}_1, \mathbf{t}_2, \mathbf{t}_3$  denote the vectors to the nearest neighbor carbon atoms with norm  $|\mathbf{t}_{1,2,3}| = 1.42 \text{ \AA}$ . One carbon atom creates three  $sp_2$  hybrid orbitals and these orbitals covalently bind next carbon atoms forming strong  $\sigma$  bonds. The  $sp_2$  hybrid orbitals consists of an  $s$  orbital, a  $p_x$  orbital, and a  $p_y$  orbital and oriented in the same plane with orientation angle  $120^\circ$  while the remaining  $p_z$  orbitals form  $\pi$  bonds.

The  $\sigma$  bonds maintain the framework of honeycomb structure of graphene and the electrons are localized between carbon atoms resulting in deep binding energy. On the other hand, the electrons in  $\pi$  bands are delocalized from the parent carbon atom. In graphene, these delocalized electrons form a characteristic band structure, namely the Dirac cone, which gives abundant properties to graphene as seen in the following sections.

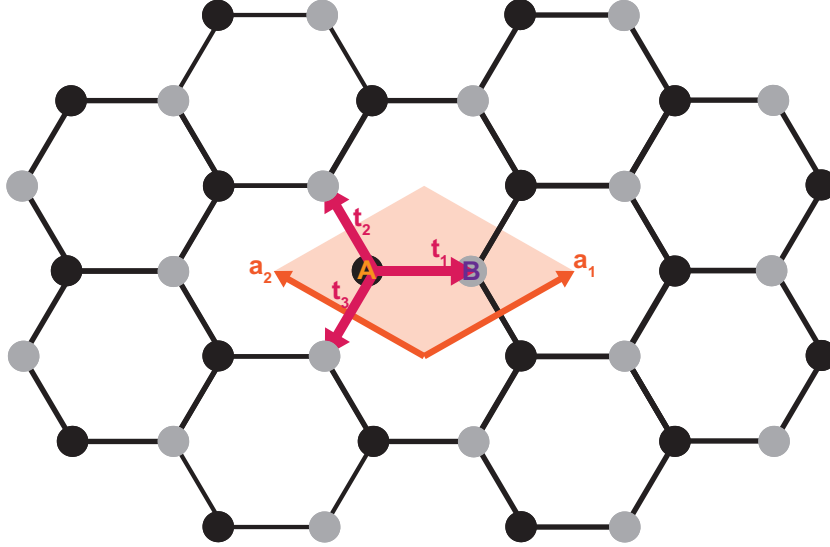


Figure 2-1: Schematic drawing of the crystal structure of graphene. A unit cell is shown by the shaded area. Black (gray) circles represent carbon atoms on a site A (B).

## 2.2 Electronic structure

### 2.2.1 Monolayer graphene

As shown in Fig. 2-1, carbon atoms form the honeycomb structure by  $sp^2$  hybridization. The unit cell consists of two fundamental unit vectors ( $\mathbf{a}_1$ ,  $\mathbf{a}_2$ ) making a diamond shape and contains two carbon atoms (labeled A and B in Fig. 2-1).

We denote the wave function of electrons in the valence band by  $\phi(\mathbf{r})$  and consider that  $\phi(\mathbf{r})$  is represented by the following form:

$$\Psi_{\mathbf{k}}(\mathbf{r}) = C_A \sum_{R_A} e^{i\mathbf{k}\cdot\mathbf{R}_A} \phi(\mathbf{r} - \mathbf{R}_A) + C_B \sum_{R_B} e^{i\mathbf{k}\cdot\mathbf{R}_B} \phi(\mathbf{r} - \mathbf{R}_B), \quad (2.1)$$

where  $\mathbf{k}$  is the wave number vector,  $C_A$  and  $C_B$  are constants for atoms A and B, and  $R_A$  and  $R_B$  denote the positions of carbon atoms A and B in the unit cell, respectively. The phase factors  $e^{i\mathbf{k}\cdot\mathbf{R}_A}$  and  $e^{i\mathbf{k}\cdot\mathbf{R}_B}$  come from the periodic phase matching condition

of the Bloch theorem. This wave function satisfies the following Schrödinger equation:

$$H\Psi_k(\mathbf{r}) = E(\mathbf{k})\Psi_k(\mathbf{r}). \quad (2.2)$$

Then, we obtain the following relation:

$$\begin{aligned} & C_A \sum_{R_A} e^{i\mathbf{k}\cdot\mathbf{R}_A} H\phi(\mathbf{r} - \mathbf{R}_A) + C_B \sum_{R_B} e^{i\mathbf{k}\cdot\mathbf{R}_B} H\phi(\mathbf{r} - \mathbf{R}_B) = \\ & C_A E(k) \sum_{R_A} e^{i\mathbf{k}\cdot\mathbf{R}_A} \phi(\mathbf{r} - \mathbf{R}_A) + C_B E(k) \sum_{R_B} e^{i\mathbf{k}\cdot\mathbf{R}_B} \phi(\mathbf{r} - \mathbf{R}_B). \end{aligned} \quad (2.3)$$

Integrating Eq. (2.3) in the whole space after multiplication of  $\phi^*(\mathbf{r} - \mathbf{R}_{A'})$  from the left side, we obtain the following two equations:

$$\begin{aligned} \text{the left-hand side} &= \langle \phi(\mathbf{r} - \mathbf{R}_{A'}) | H | \Psi_k(\mathbf{r}) \rangle \\ &= C_A \sum_{R_A} e^{i\mathbf{k}\cdot\mathbf{R}_A} \langle \phi(\mathbf{r} - \mathbf{R}_{A'}) | H | \phi(\mathbf{r} - \mathbf{R}_A) \rangle \\ &+ C_B \sum_{R_B} e^{i\mathbf{k}\cdot\mathbf{R}_B} \langle \phi(\mathbf{r} - \mathbf{R}_{B'}) | H | \phi(\mathbf{r} - \mathbf{R}_B) \rangle, \end{aligned} \quad (2.4)$$

$$\begin{aligned} \text{the right-hand side} &= \langle \phi(\mathbf{r} - \mathbf{R}_{B'}) | E(k) | \Psi_k(\mathbf{r}) \rangle \\ &= C_A E(k) \sum_{R_A} e^{i\mathbf{k}\cdot\mathbf{R}_A} \langle \phi(\mathbf{r} - \mathbf{R}_{A'}) | \phi(\mathbf{r} - \mathbf{R}_A) \rangle \\ &+ C_B E(k) \sum_{R_B} e^{i\mathbf{k}\cdot\mathbf{R}_B} \langle \phi(\mathbf{r} - \mathbf{R}_{B'}) | \phi(\mathbf{r} - \mathbf{R}_B) \rangle. \end{aligned} \quad (2.5)$$

Under the tight-binding approximation, the matrix elements have non-zero values

when the bra and the ket vectors are for the nearest-neighbor pairs or for the same site, i.e.

$$\left\{ \begin{array}{ll} \langle \phi(\mathbf{r} - \mathbf{R}_{A'}) | H | \phi(\mathbf{r} - \mathbf{R}_A) \rangle = \alpha_A \delta_{A',A}, & \\ \langle \phi(\mathbf{r} - \mathbf{R}_{B'}) | H | \phi(\mathbf{r} - \mathbf{R}_B) \rangle = \alpha_B \delta_{B',B}, & \\ \langle \phi(\mathbf{r} - \mathbf{R}_{A'}) | H | \phi(\mathbf{r} - \mathbf{R}_B) \rangle = \Delta, & A' \text{ and } B \text{ are the nearest-neighbor atoms,} \\ & = 0, \text{ otherwise,} \\ \langle \phi(\mathbf{r} - \mathbf{R}_{B'}) | H | \phi(\mathbf{r} - \mathbf{R}_A) \rangle = \Delta, & B' \text{ and } A \text{ are the nearest-neighbor atoms,} \\ & = 0, \text{ otherwise,} \\ \langle \phi(\mathbf{r} - \mathbf{R}_{A'}) | \phi(\mathbf{r} - \mathbf{R}_A) \rangle = \delta_{A',A}, & \\ \langle \phi(\mathbf{r} - \mathbf{R}_{B'}) | \phi(\mathbf{r} - \mathbf{R}_B) \rangle = \delta_{B',B}. & \end{array} \right.$$

Inserting the above results to Eqs. (2.4) and (2.5), we obtain

$$C_A(\alpha_A - E(\mathbf{k})) + C_B \Gamma(\mathbf{k}) \Delta = 0, \quad (2.6)$$

where  $\Gamma(\mathbf{k})$  is

$$\Gamma(\mathbf{k}) = e^{i\mathbf{k}\cdot\mathbf{t}_1} + e^{i\mathbf{k}\cdot\mathbf{t}_2} + e^{i\mathbf{k}\cdot\mathbf{t}_3}. \quad (2.7)$$

In the same way, we obtain the following result from the integration of  $\phi^*(\mathbf{r} - \mathbf{R}_{B'})$  times Eq. (2.3):

$$C_A \Gamma^*(\mathbf{k}) \Delta + C_B(\alpha_B - E(\mathbf{k})) = 0. \quad (2.8)$$

In order for arbitrary values of  $C_A$  and  $C_B$  to satisfy Eqs. (2.6) and (2.8), the following

equality should hold:

$$\det \begin{vmatrix} \alpha_A - E(\mathbf{k}) & \Gamma(\mathbf{k})\Delta \\ \Gamma^*(\mathbf{k})\Delta & \alpha_B - E(\mathbf{k}) \end{vmatrix} = 0.$$

From this, we obtain the band dispersion  $E(k)$  of a valence electron of graphene in the form

$$E(k) = \frac{\alpha_A + \alpha_B}{2} \pm \sqrt{\left(\frac{\alpha_A - \alpha_B}{2}\right)^2 + \Delta^2 |\Gamma(\mathbf{k})|^2}. \quad (2.9)$$

Especially in the case of ideal graphene, carbon atoms at the site A and site B are equivalent, and therefore  $\alpha_A = \alpha_B \equiv \alpha$ . Hence we can rewrite Eq. (2.9) in the following simple form:

$$E(k) = \alpha \pm \Delta |\Gamma(\mathbf{k})|. \quad (2.10)$$

Let us consider detailed calculation of  $|\Gamma(\mathbf{k})|$  in Eq. (2.7). The nearest-neighbor vectors  $\mathbf{t}_i$  ( $i=1, 2, 3$ ) are represented by the following expressions:

$$\begin{cases} \mathbf{t}_1 = \frac{a}{\sqrt{3}}\left(\frac{\sqrt{3}}{2}, -\frac{1}{2}\right), \\ \mathbf{t}_2 = \frac{a}{\sqrt{3}}(0, 1), \\ \mathbf{t}_3 = \frac{a}{\sqrt{3}}\left(-\frac{\sqrt{3}}{2}, -\frac{1}{2}\right), \end{cases}$$

from which we have

$$|\Gamma(\mathbf{k})| = \sqrt{3 + 2 \cos k_x a + 4 \cos \frac{k_x a}{2} \cos \frac{\sqrt{3} k_y a}{2}}. \quad (2.11)$$

This gives the band structure (2.10) as follows:

$$E(k) = \alpha \pm \Delta \sqrt{3 + 2 \cos k_x a + 4 \cos \frac{k_x a}{2} \cos \frac{\sqrt{3} k_y a}{2}}. \quad (2.12)$$

For example,  $E(k)$  has the following values at the high symmetry points:

$$E(\bar{\Gamma}) = \alpha \pm 3\Delta,$$

$$E(\bar{M}) = \alpha \pm \Delta,$$

$$E(\bar{K}) = \alpha.$$

Figure 2-2 shows the band dispersion along the  $\bar{\Gamma}-\bar{K}$  and  $\bar{\Gamma}-\bar{M}$  directions through the above symmetry points. In Fig. 2-2, one can clearly see gapless and linear dispersion at the  $\bar{K}$  point.

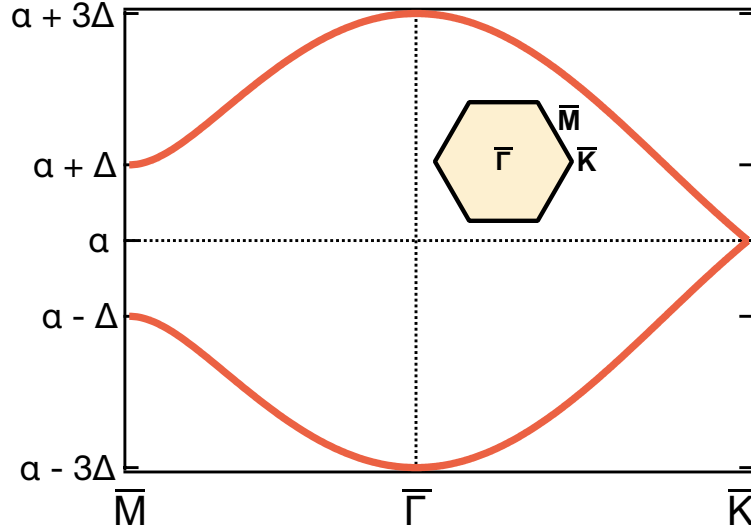


Figure 2-2: Band structure of monolayer graphene along the high symmetry directions,  $\bar{\Gamma}-\bar{K}$  and  $\bar{\Gamma}-\bar{M}$ . Inset shows the location of these high symmetry points.

As shown in Fig. 2-3 (a), the band structure of graphene is composed of the two equivalent bands with a plane of mirror symmetry at  $E(k) = \alpha$ . Especially near the  $\bar{K}$  point, Eq. (2.12) can be expanded in  $E(\mathbf{k}_K) = \pm \hbar\nu_F|\mathbf{k}_K|$ . Here  $\hbar$  is the Plank constant,  $\nu_F$  is the Fermi velocity and  $\mathbf{k}_K$  is the wavenumber measured from the  $\bar{K}$

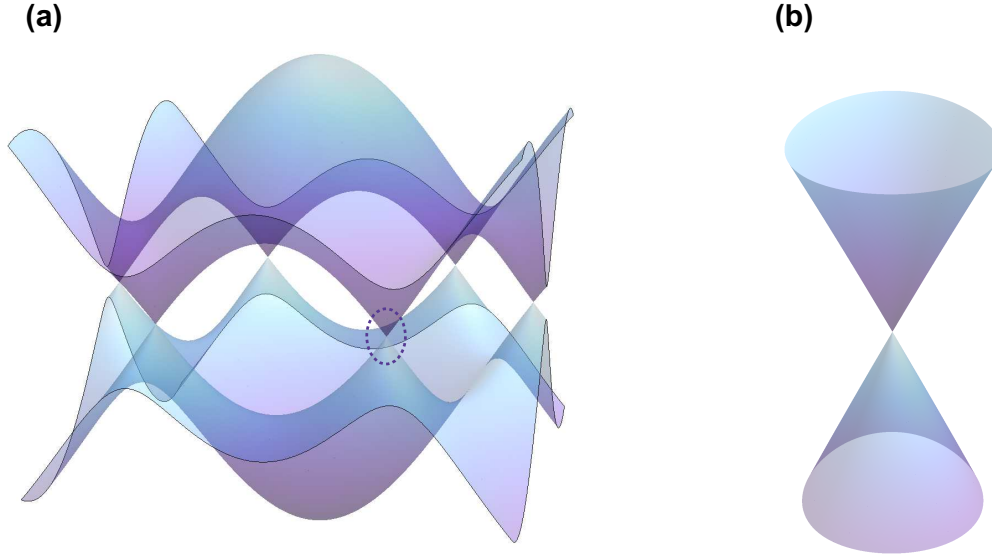


Figure 2-3: Band structure of monolayer graphene; Band structure (a) within the first Brillouin zone and (b) near the Dirac point.

point. The crossing point between the upper cone and bottom cone is the Dirac point. At the Dirac point, the density of state reaches zero and electrons around the Dirac point behave as massless Fermions because the effective mass vanishes. Electrons in graphene occupy one of the two bands because it has two electrons per unit cell, and therefore  $E_F = \alpha$ .

Up to here, we have assumed that carbon atoms at the sites A and B in a unit cell are equivalent. However, if the equivalence between two sites is broken by an external field or a structural defect,  $\alpha \neq \alpha'$  is expected, which opens a band gap  $\Delta E = 2|\alpha - \alpha'|$  at the Dirac point.

### 2.2.2 Bilayer graphene

Unlike a monolayer graphene, the electronic structure of bilayer graphene is significantly modified. Figure 2-4 shows two possible stacking patterns of bilayer graphene: AB (Bernal) and AA stacking. Usually, bilayer graphene forms AB stacking because

it is slightly stabler than AA stacking.

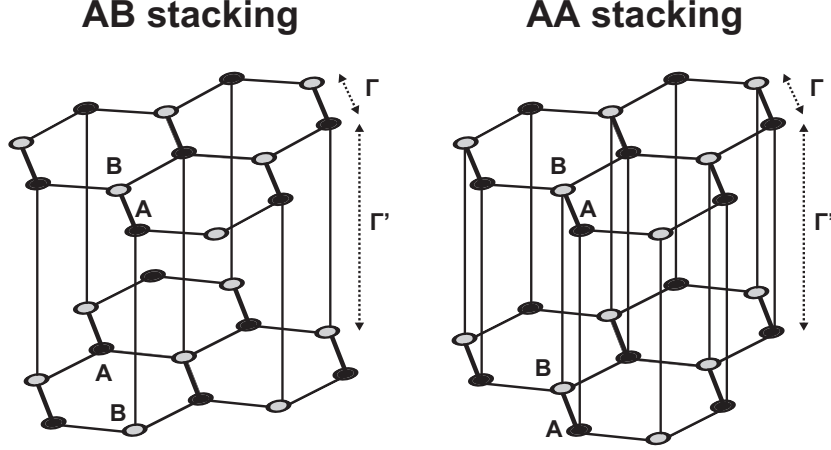


Figure 2-4: The crystal structure of two different stacking patterns; AB stacking and AA stacking.

Figure 2-5 compares the band structures of (a) AB and (b) AA stacking bilayer graphene. In the case of AB stacking, the hopping energy  $\Gamma'$  for interlayer carbon atoms is about 0.4 eV and the band structure is approximately expressed as follows [5]:

$$E(\mathbf{k}) = \pm \left[ \frac{\Gamma'}{2} \pm \sqrt{\left(\frac{\Gamma'}{2}\right)^2 + (\hbar v_F |\mathbf{k}_K|)^2} \right]. \quad (2.13)$$

The entire band is composed of two pairs of electron and hole bands and one of these touches at the Fermi energy and the other has the edges at  $\pm 0.4$  eV from the Fermi energy, respectively. Although the former pair keeps inherent gapless property, its band structure is no longer a linear dispersion but forms a parabolic dispersion which is proportional to the square of wavenumber  $k$ . These parabolic bands are approximated by the following formula in the vicinity of band touching point:

$$E(\mathbf{k}) \approx \pm \frac{(\hbar v_F |\mathbf{k}_K|)^2}{\Gamma'}. \quad (2.14)$$

Contrary to AB stacking, the band structure of AA stacking is composed of the following four linear dispersion bands:

$$E(\mathbf{k}) = \pm \hbar \nu_F |\mathbf{k}_K| \pm \Gamma'. \quad (2.15)$$

These bands are considered to be equivalent to those of monolayer graphene with a shift of  $\pm \Gamma'$ .

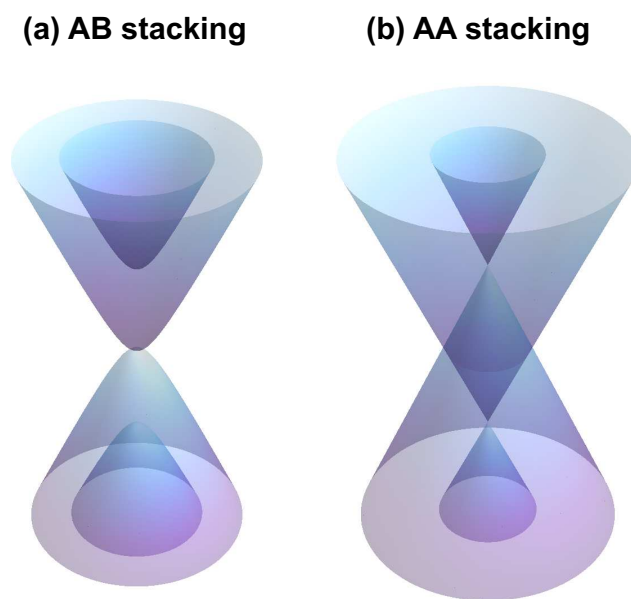


Figure 2-5: Band structures with different stacking patterns; Band structure of (a) AB and (b) AA stacking bilayer graphenes.

## 2.3 Optical properties

Interestingly, in the visible region, optical properties of graphene, such as the optical conductance  $G$ , the transmittance  $T$  and the reflectance  $R$ , are frequency-independent and universally defined by fundamental physical constants [6, 7]:

$$G = \frac{e^2}{4\hbar} \approx 6.08 \times 10^{-5} \Omega^{-1}, \quad (2.16)$$

$$T = \left(1 + \frac{\pi\alpha}{2}\right)^{-2} \approx 1 - \pi\alpha \approx 0.977, \quad (2.17)$$

$$R = \frac{1}{4}\pi^2\alpha^2 T \approx 0.00013, \quad (2.18)$$

where  $e$  is the elementary charge and  $\alpha = e^2/\hbar c \approx 1/137$  (where  $c$  is the speed of light) is the fine structure constant.

As described in Eq. (2.18), the reflectivity of monolayer graphene is negligibly small. Thus, the absorption rate in the visible region is determined to be  $(1 - T) \approx \pi\alpha \approx 2.3\%$ . Experimental results show a perfect agreement with these estimates [7]. As shown in Fig. 2-6 (A) and (B), the absorption rate of monolayer graphene is approximately constant over a wide range of wavelength and proportional to the number of graphene layers.

## 2.4 Epitaxial graphene on SiC substrate

Annealing silicon carbide (SiC) is one of the major methods of preparing graphene sheets on a semi-conducting substrate: when SiC is annealed above 1000 °C, Si atoms are sublimated from the SiC surface and the remaining carbon atoms form a honeycomb structure. Depending on the surface termination of SiC, i.e. Si-terminated (0001) face (Si-face) and C-terminated (000 $\bar{1}$ ) face (C-face), structural and electronic properties of the resulting graphene sheets totally differ from each other. In this

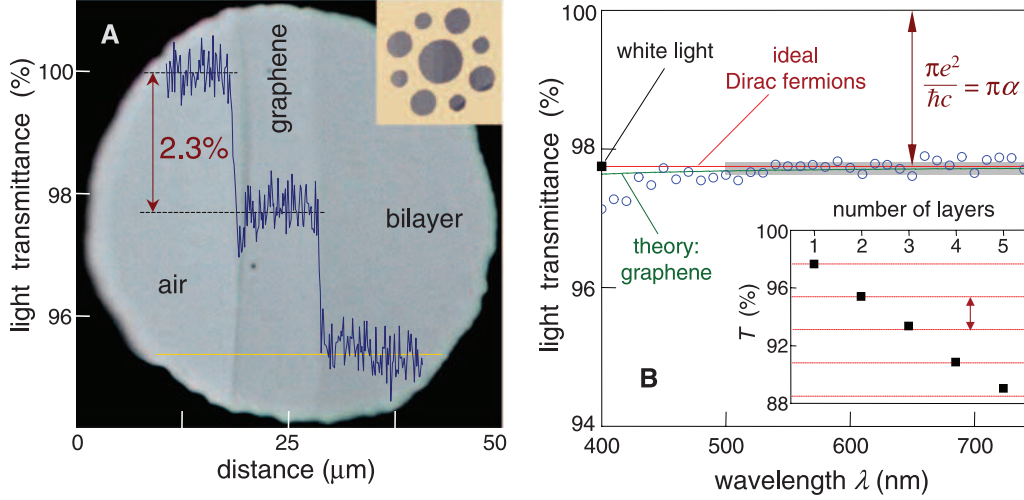


Figure 2-6: Transmittance of graphene sheets in the visible region. (A) Photograph of a graphene sample in transmitted white light in an optical microscope. (B) Transmittance spectrum of graphene. Figure is taken from [7].

section, the crystalline and electronic structures of graphene on Si- and C-faces are introduced and compared in Sec. 2.4.1 (Si-face SiC) and Sec. 2.4.2 (C-face SiC).

### 2.4.1 Epitaxial graphene on Si-face SiC(0001)

On Si-face SiC(0001) surface, graphene layers are epitaxially grown with  $30^\circ$  rotation with respect to the c-axis from the SiC substrate. At the beginning of the growth, Si atoms are gradually sublimated from the topmost layer in several annealing steps [8] at  $1050^\circ\text{C}$  and  $1150^\circ\text{C}$  leading to the Si-rich  $(\sqrt{3} \times \sqrt{3})R30^\circ$  and the carbon-rich  $(6\sqrt{3} \times 6\sqrt{3})R30^\circ$  reconstruction layer, respectively as illustrated in Fig. 2-7 [9].

This reconstruction layer has nearly the same structure as to a graphene layer but some bonds with Si atoms of the substrate still remain. By further annealing, the excess Si atoms are removed from the surface and finally the first graphene layer is formed. At the interface of the first graphene layer and SiC, another graphene-like  $(6\sqrt{3} \times 6\sqrt{3})R30^\circ$  layer appears. This reconstruction layer is called the buffer layer or the zeroth graphene layer. Theoretical studies in 2008 suggested a hypothetical  $(\sqrt{3} \times \sqrt{3})R30^\circ$  surface unit cell at the interface between the SiC substrate and the

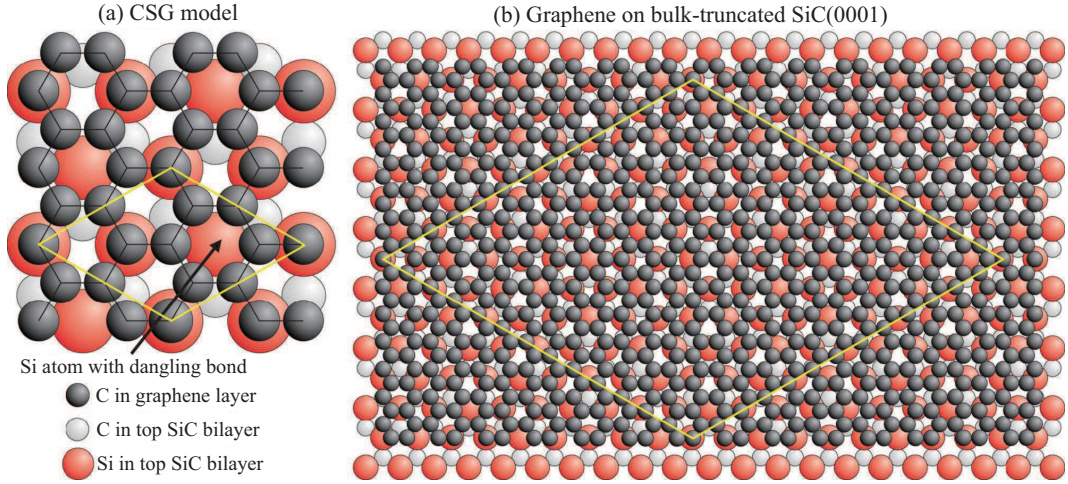


Figure 2-7: Crystal geometry of monolayer graphene grown on a Si-face SiC(0001) substrate. (a) Top view of the covalently bound stretched graphene (CSG) model on SiC(0001). The unit mesh of  $(\sqrt{3} \times \sqrt{3})R30^\circ$  of the model surface is indicated by a large yellow diamond. (b) Top view of a monolayer graphene placed on the  $(6\sqrt{3} \times 6\sqrt{3})R30^\circ$  reconstruction layer. Figure is taken from [9].

first graphene layer [10–12]. This reconstruction requires a dilation of 8 % stretching of the C-C distance and therefore it is referred to as the “covalently bound stretched graphene” (CSG) model in Ref. [9], as shown in Fig. 2-7 (a). Figure 2-7 (b) shows the crystal geometry of monolayer graphene placed on the  $(6\sqrt{3} \times 6\sqrt{3})R30^\circ$  reconstruction layer.

Many researches have been carried out on the electronic structures of the buffer layer and graphene on SiC(0001). Figure 2-8 [9] compares how the graphene-like buffer layer differs from the graphene layer on SiC(0001) electronic-structurally (a, b) and crystal-structurally (c, d). Figure 2-8(c, d) show that low energy electron diffraction (LEED) spots of both buffer and graphene layers appear mostly at the same points with  $30^\circ$  rotated from the SiC substrate. These mean that the buffer layer and graphene are crystal-structurally equivalent.

On the other hand, the electronic band structures of the buffer layer and the graphene layer have quite different  $\pi$  bands, whereas the  $\sigma$  bands are surprisingly similar to each other as described in Fig. 2-8 (a, b). The good agreement between

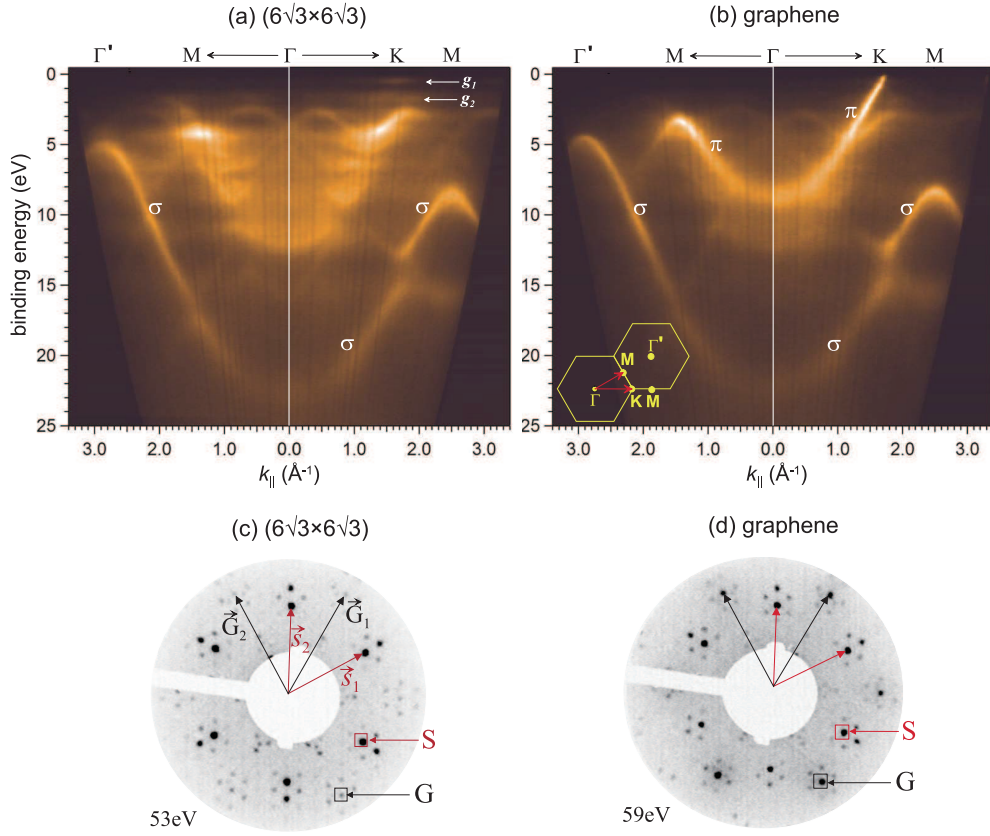


Figure 2-8: Photoelectron intensity map and LEED patterns of buffer layer and single layer graphene [9]. Electronic structure of (a)  $(6\sqrt{3}\times 6\sqrt{3})$  reconstruction layer (buffer layer) and (b) monolayer graphene along  $\Gamma$ -M- $\Gamma'$  and  $\Gamma$ -K-M directions as shown in the inset of (b). LEED patterns of the (c)  $(6\sqrt{3}\times 6\sqrt{3})$  reconstruction layer and (d) monolayer graphene on SiC(0001). The symbols  $\vec{s}_1$  and  $\vec{s}_2$  denote the reciprocal lattice vectors of the SiC ( $\vec{s}_1, \vec{s}_2$ ) and  $\vec{G}_1$  and  $\vec{G}_2$  denote those of the graphene ( $\vec{G}_1, \vec{G}_2$ ). Figure is taken from [9].

the  $\sigma$  bands indicates that the in-plane bonds (e.g. C-C bond length) are almost identical. The difference in the  $\pi$  bands is because the  $p_z$  orbitals (out-of-plane bonds) of C atoms in the buffer layer are partially bound to the substrate. In the monolayer graphene, the Fermi energy is shifted higher about 0.4 eV from a neutral graphene. This electron-doping is attributed to the charge transfer from the substrate [13].

In 2009, a new fabrication method of wafer-size graphene layers was developed by annealing a SiC substrate under precisely controlled atmospheric pressure [14]. By annealing under Ar gas of pressure about 1 bar, the Si sublimation rate is reduced

because some silicon atoms desorbing from the surface are reflected back to the surface after collision with Ar atoms. This allows one to precisely control the Si evaporation rate, and thus morphologically better graphene samples with larger domain sizes are obtained. Compared to a graphene sample grown under the ultra high vacuum condition, for which the domain sizes are typically 30-100 nm in diameter, a graphene sample grown under the Ar gas atmosphere has much larger domain sizes typically about 50  $\mu\text{m}$  long and about 3  $\mu\text{m}$  wide.

Figure 2-9 [14] shows microscopic images taken by (a) atomic force microscope (AFM), (b) low-energy electron microscope (LEEM) and (c) the height profile of the obtained graphene films. As demonstrated in Fig. 2-9, large domain sizes of monolayer graphene is grown perpendicularly to the step direction.

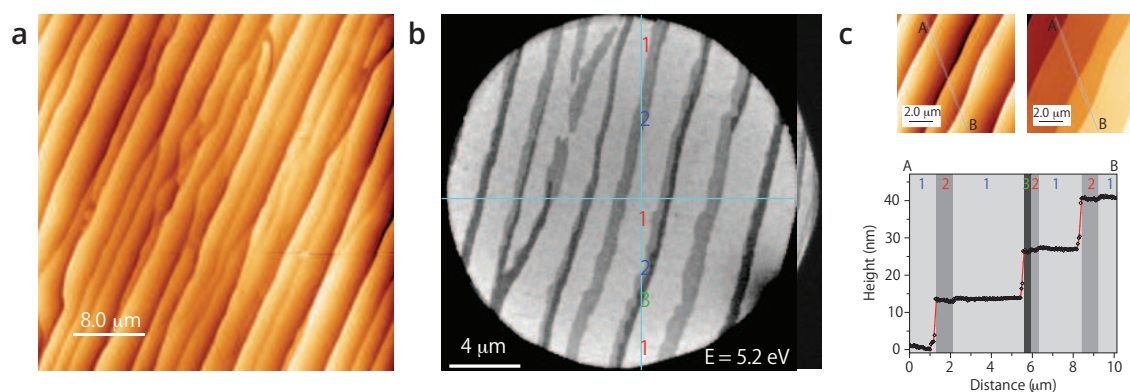


Figure 2-9: Microscopic morphology of growing graphene on the SiC(0001) substrate [14]. (a) AFM image of graphene on SiC(0001) with a nominal thickness of 1.2 layer formed by annealing in Ar gas atmosphere (900 mbar, 1650 °C). (b) Monolayer, bilayer and trilayer graphenes are readily identified by the presence of 1, 2 or 3 reflectivity minima, respectively. (c) The bottom panel shows the height profile along the line from A to B of the upper panels. Figure is taken from [14].

In summary, a graphene grown on SiC(0001) has a buffer layer at the interface between the lowermost graphene layer and the topmost SiC surface. Carbon atoms in the buffer layer are partially coupled to the substrate and as a result, graphene layers are slightly n-doped due to the charge transfer from the substrate. For the crystal

structure, graphene layers on SiC(0001) surface have good crystallinity because the buffer layer plays a critical role as a basal plate for epitaxial growth of graphene layers.

### 2.4.2 Epitaxial graphene on C-face SiC(000 $\bar{1}$ )

Because of the absence of a buffer layer, graphene layers grown on the C-face SiC(000 $\bar{1}$ ) surface are different from those grown on Si-face SiC(0001) in many ways [9, 15, 16]. First, the absence of a buffer layer results in rotational stacking faults within each graphene layer as well as between the first graphene layer and the topmost SiC surface. Second, graphene layers are almost decoupled from the substrate. Therefore the band structure is not affected by charge transfer from the SiC substrate.

Figure 2-10 compares the (a-d) electronic and (e-h) crystal structures of graphene layers at different growth stages. At the beginning of the growth stage (Fig. 2-10 (b)), the  $\pi$  and  $\sigma$  bands which are characteristic of a graphene layer already appear. Then the photoelectron intensity of the  $\pi$  and  $\sigma$  bands gradually increases (Fig. 2-10 (c, d)) and at the same time, the signatures of rotated domains, which are labeled  $\pi'$  and  $\sigma'$ , are observed. This rotational faults also emerged in LEED patterns (Fig. 2-10 (e-h)), appearing as diffraction arcs around graphene ( $1 \times 1$ ) spots. For these reasons, the stacking structure of graphene layers grown on SiC(000 $\bar{1}$ ) is considered not to be AB or AA stacking, but turbostratic stacking.

In 2009, M. Sprinkle *et al.* performed an angle-resolved photoemission spectroscopy (ARPES) measurement on multilayer graphene grown on C-face SiC(000 $\bar{1}$ ) and reported the first direct observation of a nearly ideal graphene band structure [17]. This fact indicates that each layer of multilayer graphene grown on SiC(000 $\bar{1}$ ) can be regarded as an electronically isolated graphene sheet. This result also supports turbostratic stacking.

In 2014, on the other hand, L. I. Johansson *et al.* reported clear evidence of graphite-like AB stacking by using nano-ARPES measurement [18]. This difference in observations may arise from their fabrication procedures, such as the substrate treatment, the annealing temperature and the annealing time.

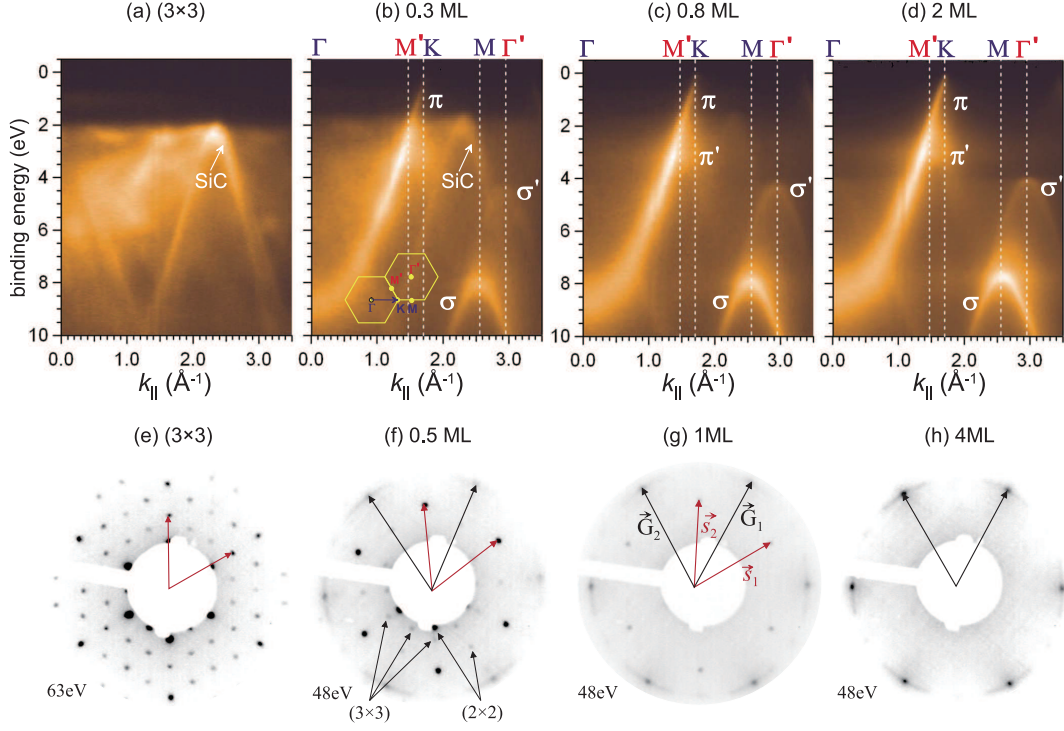


Figure 2-10: (a-d) Photoelectron intensity map at different stages of graphene layers grown on SiC(000 $\bar{1}$ ). (e-h) LEED patterns for various growth stages of graphene layers. Figure is taken from [9].

As for the uniformity of graphene layers grown on C-face SiC(000 $\bar{1}$ ), coexistence of different numbers of graphene layers within several tens of  $\mu$  meters was reported [18] over the range of 2 to 5 layers. This is because compared to slow growth rates of Si-face graphene, high growth rates in C-face graphene make thin film growth much more difficult. Even today, precise control of the number of graphene layers is challenging and fabrication of a uniform monolayer graphene on C-face SiC(000 $\bar{1}$ ) is yet to be realized.

### 2.4.3 Quasi free-standing epitaxial graphene

The presence of the buffer layer in Si-face SiC(0001) is sometimes unfavorable because it modifies the electronic structure and affects transport properties of graphene grown on it. For these reasons, an ideal graphene which is fully decoupled from the SiC substrate is strongly demanded.

Recently, C. Riedl *et al.* succeeded in preparing quasi-free-standing (QFS) epitaxial graphene on a Si-face SiC(0001) surface, i.e., graphene layers are nearly decoupled from the SiC substrate [19]. Figure 2-11 illustrates side-view models for (a) the buffer layer, (b) the buffer layer with monolayer graphene, (c) QFS monolayer graphene and (d) QFS bilayer graphene, respectively. QFS monolayer graphene is prepared by intercalating H atoms into the buffer layer and terminating the dangling bonds of topmost Si atoms as shown in Fig. 2-11 (c). In the same way, QFS bilayer graphene is prepared from monolayer graphene on buffer layer (Fig. 2-11 (d)).

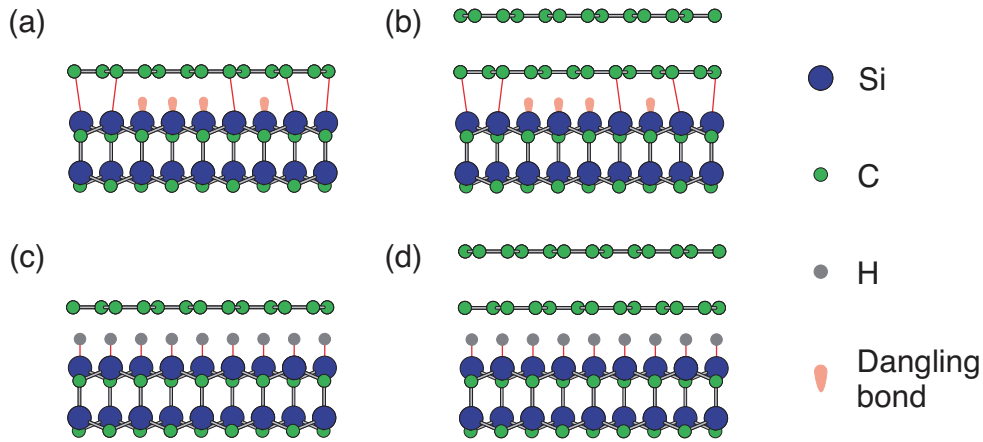


Figure 2-11: Side view models for (a) the buffer layer, (b) the buffer layer with monolayer graphene, (c) QFS monolayer graphene and (d) QFS bilayer graphene. Figure is taken from [19].

Figure 2-12 [19] shows a series of ARPES spectra of QFS monolayer graphene (top panels) and QFS bilayer graphene (bottom panels) at different growing stages. As shown in the top panels of Fig. 2-12, the zeroth-layer graphene (the buffer layer) is gradually decoupled from the SiC substrate, forming nearly decoupled graphene represented by a single Dirac cone in Fig. 2-12 (b). After following annealing steps described in Fig. 2-12 (c-e), intercalated hydrogen atoms are gradually desorbed from the interface resulting in turning back to the original zeroth-layer graphene.

Similarly to the case of QFS monolayer graphene, QFS bilayer graphene is prepared by decoupling the buffer layer from SiC substrate as schematically shown in

Fig. 2-11 (d). After the hydrogen treatment, a double Dirac band appeared (Fig. 2-12 (g)) but then gradually disappeared by the subsequent annealing steps (Fig. 2-12 (h-j)).

Compared to the band structure of monolayer graphene with a buffer layer (Fig. 2-12 (f)), because of the lack of the buffer layer which is partially coupled with the substrate, the band structure of QFS monolayer graphene has a nearly neutral Dirac cone with the Dirac point located near the Fermi energy, indicating no charge transfer from the SiC substrate. However, a small amount of p-doping caused by the spontaneous polarization of the substrate was reported [13]. Because of this, QFS graphene is not regarded as ideal graphene but “nearly” ideal graphene.

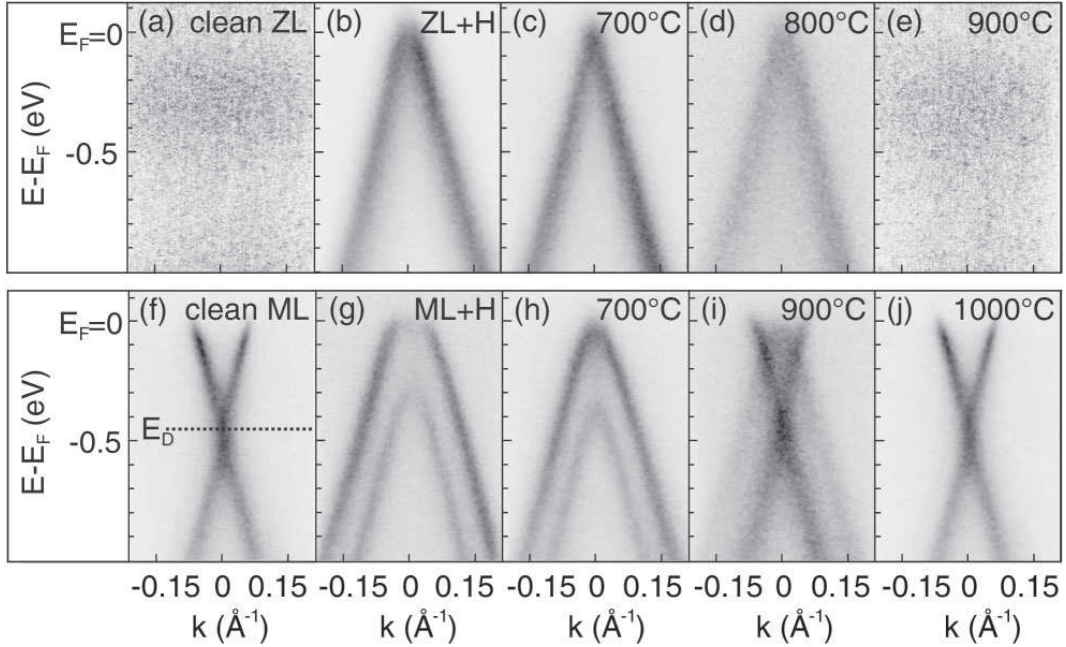


Figure 2-12: ARPES images for a series of annealing processes under hydrogen atmosphere. (a-e) Formation of QFS monolayer graphene and desorption of hydrogen atoms by the subsequent annealing steps. (f-j) Formation of QFS bilayer graphene and desorption of hydrogen atoms by the subsequent annealing steps. Figure is taken from [19].

# Chapter 3

## Experimental method

### 3.1 Measurement

#### 3.1.1 Photoemission spectroscopy

Properties of a material such as the electric conductivity, the thermal conductivity and the chemical reaction are characterized by electrons, especially in a valence band. Therefore, the most important thing in understanding material science is to reveal the electronic structure of the material. Photoemission Spectroscopy (PES) is an experimental technique widely used not only in the field of physics but also in the field of chemistry and engineering in order to investigate an electronic structure of solid-state materials.

When light with specific wavelength is applied to an atom, electrons in the atom absorb the energy  $h\nu$  of photon and can be emitted from a material surface owing to the photoelectric effect, which was primarily explained by Albert Einstein in 1905. In this phenomenon, the total energy of the electron and the photon is conserved as in the following equation:

$$E_k = h\nu - E_b - \phi, \quad (3.1)$$

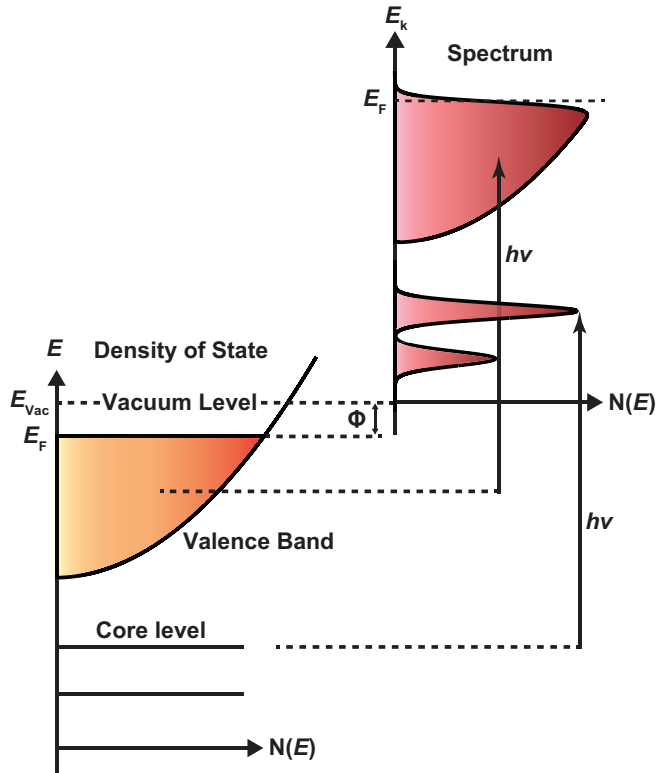


Figure 3-1: Schematic drawing of photoemission spectroscopy [20]. Vertical axes shows (left) the binding energy of electrons in a sample and (right) the kinetic energy of photo-excited electrons from the sample surface. Horizontal axes shows (left) the number of electrons in a sample and (right) the number of photoelectrons reached at the detector.

where  $E_k$  is the kinetic energy of the photoelectron,  $E_b$  is the mechanical energy (the Coulomb and kinetic energy) of electrons at the initial state, which is called the binding energy, and  $\phi$  is the work function of the material. If one already knows the value of the incident photon energy  $h\nu$  and the work function  $\phi$ , the binding energy  $E_b$  is obtained by measuring the kinetic energy  $E_k$  of the photoelectron.

However, in the actual photoemission measurement, the sample and the electron analyzer are electrically grounded, resulting in aligning their Fermi levels with the ground level as shown in Fig. 3-2. The kinetic energy of photo-excited electrons are modified during traveling from the sample to the analyzer and measured as  $E'_k$  at the detector. The relation of the kinetic energy  $E_k$  and the work functions  $\phi$  and  $\phi'$  for

the sample and the analyzer are given by the following:

$$E_k + \phi = E'_k + \phi'. \quad (3.2)$$

Each measurement system has an inherent  $\phi'$  and it can be determined by measuring the kinetic energy  $E'_{k(\text{Fermi})}$  of the electron excited from the Fermi level where  $E_b$  becomes zero, given by  $\phi' = h\nu - E'_{k(\text{Fermi})}$ . The values of  $\phi'$  for the photoemission beamlines described in Sec. 3.3.1 and Sec. 3.3.2 are calibrated to be 4.5 eV and 4.7 eV, respectively. Thus one can know the binding energy  $E_b$  of the sample using the obtained  $\phi'$  and the measured  $E'_k$  as

$$E_b = h\nu - E'_k - \phi'. \quad (3.3)$$

In a usual PES measurement, a He discharge lamp, an X-ray tube, a laser light source, and synchrotron radiation is used as a light source, and the number of emitted photoelectrons which have a specific energy is counted by a detector. By sweeping the energy window of the detector, the density of state in a sample  $N(E)$  can be estimated as described in Fig. 3-1.

Nowadays, a “three-step model” developed by Berglund and Spicer is widely used to explain a photoemission process [21]. As described in Fig. 3-3, the three-step model assumes that the following three processes happen independently:

**Step 1** Photoexcitation process of electrons in a sample;

**Step 2** Transportation of photo-excited electrons to the sample surface;

**Step 3** Photoelectron emission process by penetrating the sample surface.

In the step 1, in the photoexcitation process, the optical transition between electronic levels takes place in the order of  $10^{-16}$  s, which is shorter than atomic oscillation

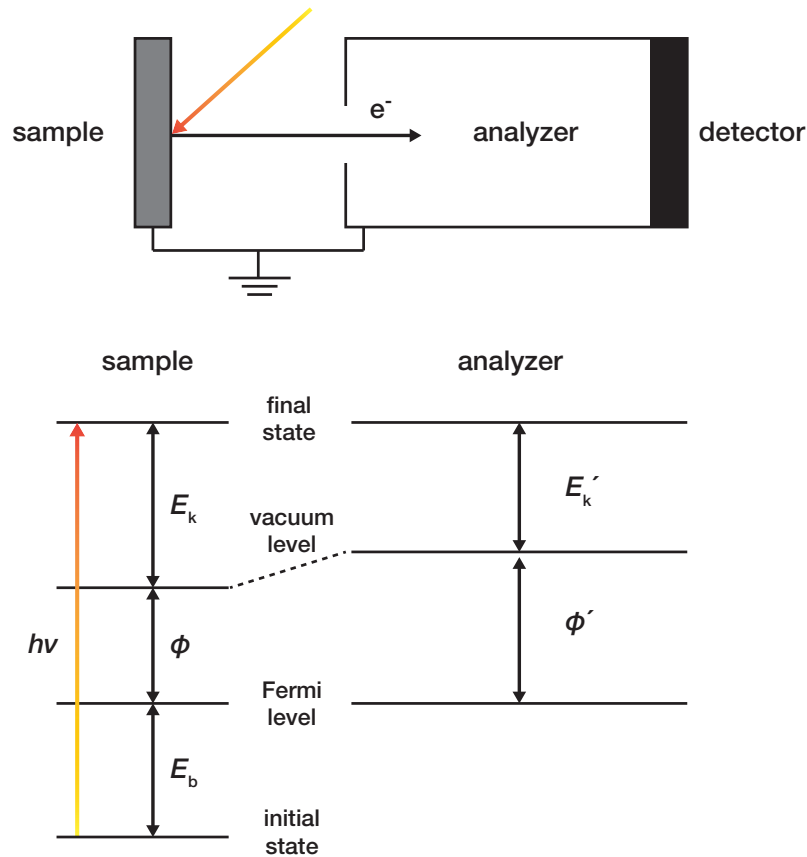


Figure 3-2: Energy diagram of the sample and the analyzer in the photoemission measurement. The sample and the analyzer are grounded each other.

period ( $10^{-12} \sim 10^{-14}$  s). Therefore, one can view atoms in the sample to be static during the photoelectron emission process. For this reason, one does not need to consider the modulation of the electronic structure during a photoexcitation process. This is called the Franck–Condon principle.

In the step 2, during the transport process to the sample surface, some photoelectrons lose a portion of their kinetic energy via scattering with phonons and electrons. Thereby the background of these secondary electrons appears on the photoemission spectrum (see the middle spectrum of Fig. 3-3). On the other hand, photoelectrons which are not affected by the scattering do not loss their energy. Therefore, an actual photoemission spectrum is a superposition of the spectra of the primary electrons and the secondary electrons.

In the step 3, during the penetration process, photoelectrons which have higher kinetic energy than the work function can be emitted from the sample surface to vacuum but others with lower kinetic energy can not. Finally a photoemission spectrum is obtained like the top spectrum of Fig. 3-3.

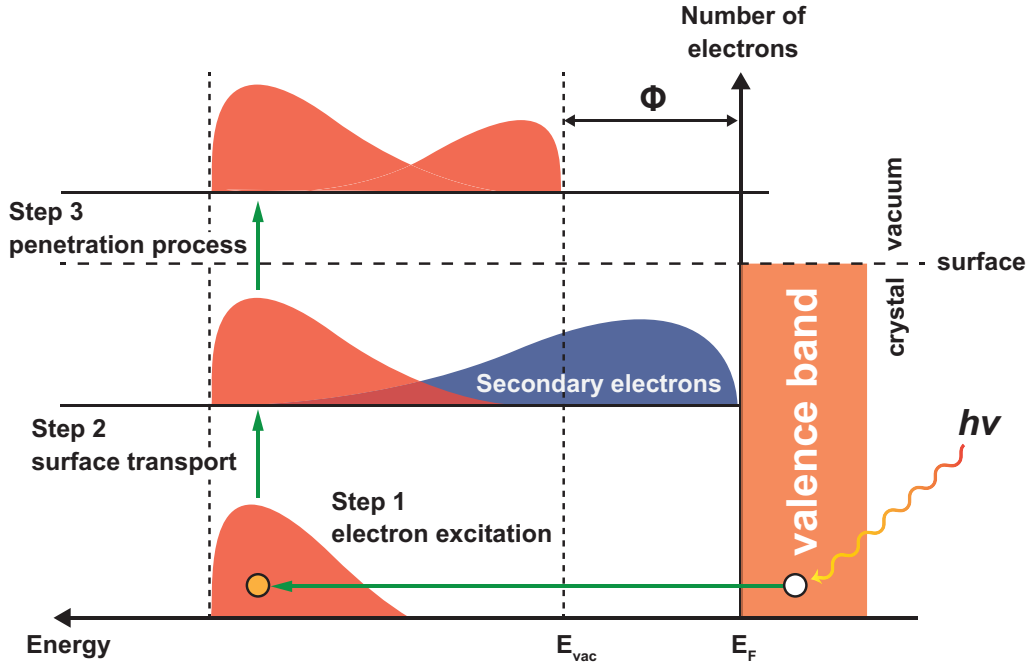


Figure 3-3: Schematic drawing of the three-step model [21]: (step 1) Photoexcitation process of electrons in a sample. (step 2) Transportation of photo-excited electrons to the sample surface. (step 3) Photoelectron emission process by penetrating the sample surface.

### 3.1.2 Angle-resolved photoemission spectroscopy

Angle-resolved Photoemission Spectroscopy (ARPES) is a powerful tool for investigating the energy dispersion in the momentum space i.e. one can experimentally know the band structure of a sample. When an electron on a valence band of a crystal is excited from initial state  $E_b$  to final state  $E_k$  by excitation light with the photon energy of  $h\nu$ , the energy conservation law is given by Eq. (3.1). Given that the final state of the photoelectron is a free electron, the energy of the final state is written by

the following equation,

$$E_k = \frac{\hbar^2(K_{\parallel}^2 + K_{\perp}^2)}{2m}, \quad (3.4)$$

where  $K_{\parallel}$  and  $K_{\perp}$  are the wavenumbers of the emitted photoelectron parallel and perpendicular to the crystal surface (see Fig. 3-4), respectively, and  $m$  is the mass of the electron. Thus,  $K_{\parallel}$  and  $K_{\perp}$  are described by the kinetic energy  $E_k$  and the emission angle  $\theta$  as the following:

$$K_{\parallel} = \frac{\sqrt{2mE_k}}{\hbar} \sin \theta, \quad (3.5)$$

$$K_{\perp} = \frac{\sqrt{2mE_k}}{\hbar} \cos \theta. \quad (3.6)$$

As shown in Fig. 3-4, the parallel component of the momentum vector is conserved along the crystal surface, because of the translation symmetry, we have,

$$k_{\parallel} = K_{\parallel}, \quad (3.7)$$

where  $k_{\parallel}$  is the parallel momentum of the electron in the crystal (see Fig. 3-4). On the other hand, the perpendicular momentum is not conserved during photoemission processes; it is affected by the inner potential of the crystal  $V_0$ . Using these relation, we have the initial energy and the momentum of a photoelectron in the crystal as

follows:

$$k_{\parallel} = \frac{\sqrt{2mE_k}}{\hbar} \sin \theta, \quad (3.8)$$

$$k_{\perp} = \frac{\sqrt{2m}}{\hbar} \sqrt{E_k \cos^2 \theta + V_0}. \quad (3.9)$$

In particular, for two-dimensional materials such as graphene, we can only consider the parallel momentum because  $k_{\perp} = 0$  in two-dimensional materials. Collecting photoelectrons emitted from various angles  $\theta$  and using the relation (3.8), one can obtain the band dispersion ( $E(k_{\parallel})$ ) on a two-dimensional Brillouin zone.

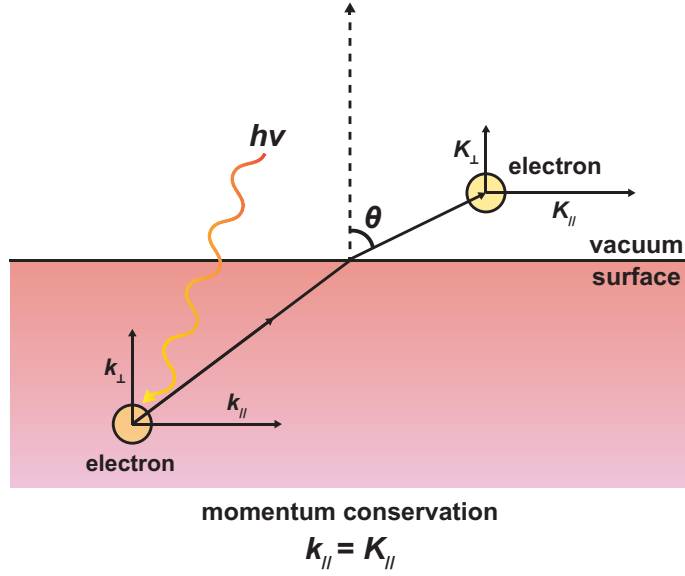


Figure 3-4: Schematics of the in-plane symmetry of the momentum of a photoelectron.

### 3.1.3 Time-resolved photoemission spectroscopy

Time-Resolved Photoemission Spectroscopy (TRPES) is a combined technique of photoemission spectroscopy and a pump-probe method, which requires a pulsed light source. The pump-probe method is a typical experimental technique for various time-resolved measurements. Figure 3-5 shows a schematic drawing of time-resolved photoemission spectroscopy in (a) the real space and (b) the reciprocal space.

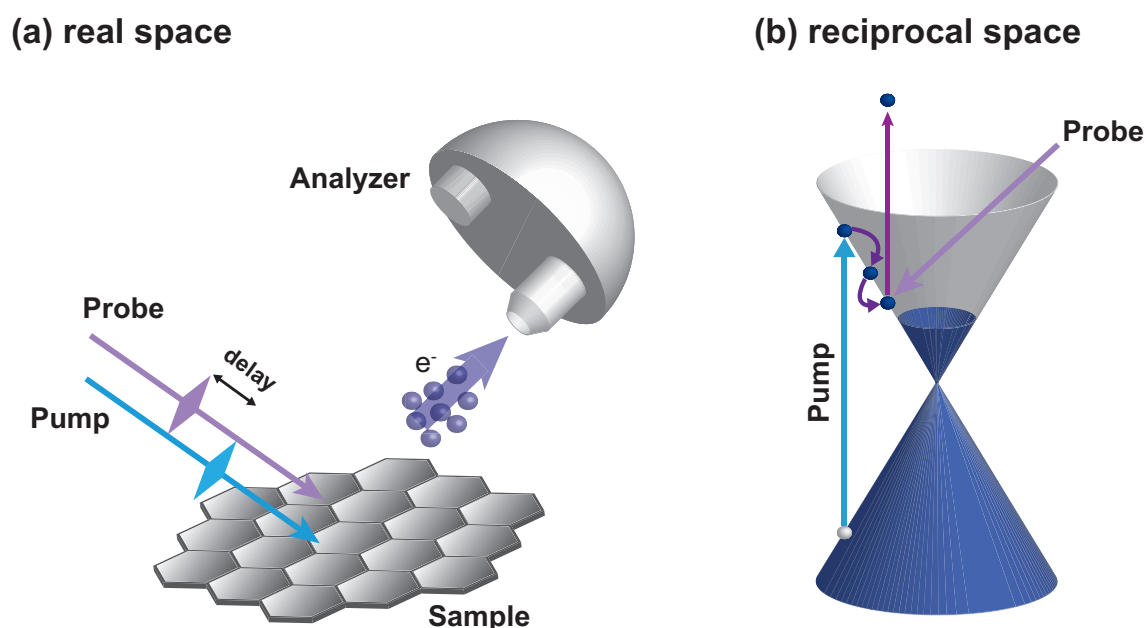


Figure 3-5: Schematic drawing of time-resolved photoemission spectroscopy in (a) a real space and (b) a reciprocal space.

First, a pump light excites an electronic system of a sample and a subsequent probe light having a specific time delay investigates the excited electronic system. By sweeping the delay time, a series of relaxation processes of the electron population is traced in various time scales. In the pump-probe method, there are two ways to make a time delay ; (1) using the same light source for both the probe and the pump light and (2) synchronized different light sources. The former is widely used in laser based

TRPES experiments (laser pump and laser probe) [22–25] and the latter is usually used in synchrotron radiation facilities (laser pump and synchrotron probe) [26–28]. In the case of (1), the delay time is determined by the difference between the optical paths of pump and probe light and usually the delay stage is used to control the difference. Thus, the time resolution is governed by the pulse width of the probe and pump light. On the other hand, in the case of (2), the timing of both lights is electrically controlled. Thus, the time resolution is governed by the production of the pulse width and electrical jitter.

By using TRPES, one can trace a relaxation dynamics of photo-excited electrons on a time scale of femto-seconds to micro-seconds. From the temporal evolution of the relaxation dynamics, such as the carrier distribution, the electronic energy and the momentum, one can know various information including carrier-carrier scattering, carrier-phonon scattering, phonon-phonon scattering, and so on.

## 3.2 Light sources

In this section, light sources used in this thesis are introduced.

### 3.2.1 High-harmonic generation

High harmonic generation (HHG) is an extreme nonlinear process which occurs in a strong field regime. This process requires the laser intensity at least  $10^{13}$  W/cm<sup>2</sup>, which can be obtained by focusing a high power femtosecond laser. Since the discovery of HHG, many theoretical studies have been dedicated to explain the mechanism of the HHG. To precisely describe the HHG process, one has to numerically calculate the time-dependent Schrödinger equation. However, the physical picture of HHG can be understood by a quasi-classical model called the three-step model, which describes the interaction between atoms and strong laser fields and the resulting HHG process [29].

In the first step, a strong laser field modifies a nucleus potential of an atom and accordingly an electron can ionize by tunneling through the modified barrier (Fig. 3-6, step 1). After the tunneling process, the electron is then accelerated in the laser

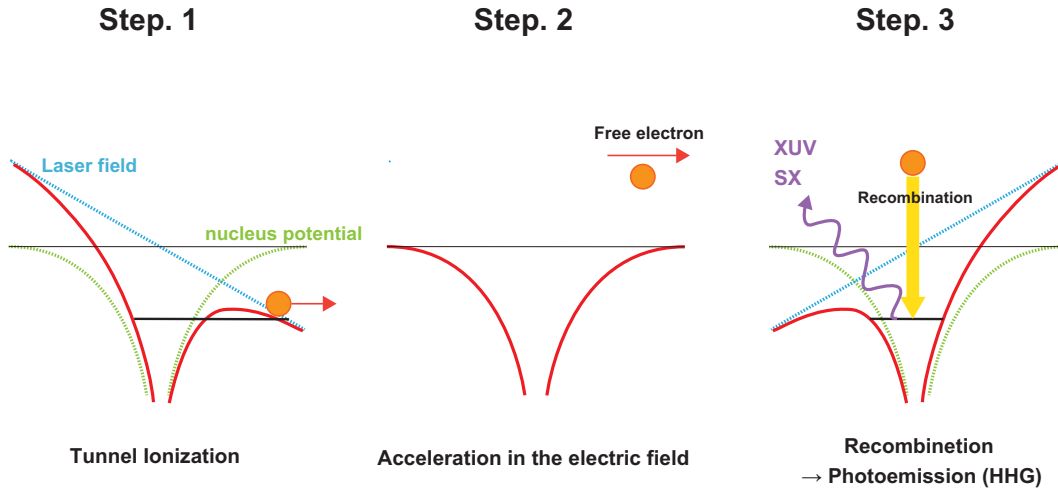


Figure 3-6: Schematic drawing of the three-step model: (step 1) Tunnel ionization induced by a strong laser field; (step 2) Acceleration of the free electron in the electric field; (step 3) Recombination to the ionic parent and resulting photoemission.

field and gains momentum (Fig. 3-6, step 2). After the reverse of the laser field, the electron is accelerated back toward the ionic parent. Resulting in the recombination of the electron with the parent ion, the electron releases a photon in the energy range of extreme ultraviolet (XUV) to soft X-ray (SR) region (Fig. 3-6, step 3). A typical HHG spectrum of our HHG beamline is shown in Fig. 3-8(b), Sec. 3.3.1.

### 3.2.2 Synchrotron radiation

Synchrotron Radiation (SR) is the only light source which can provide tunable wavelength light over the range from infrared light to hard X-ray with high brightness. SR is emitted when the trajectory of an electron accelerated close to the speed of light is bended by a magnetic field (Fig. 3-7). The performance of SR is characterized by relativistic parameters,

$$\beta = \frac{v}{c}, \quad (3.10)$$

$$\gamma = \frac{1}{\sqrt{1 - \beta^2}} = 1957 E \text{ [GeV]}, \quad (3.11)$$

where  $v$  is the velocity of an electron,  $c$  is the speed of light in vacuum and  $E$  is the kinetic energy of an electron. Here,  $\gamma$  is called the Lorentz factor and represents the relative energy compared to a static electron. For example, in SPring-8, electron beams are operated at 8.0 GeV, resulting in  $\beta = 0.999999998$  and  $\gamma = 15656$ . Using these parameters, the divergence angle  $\theta_d$  at SPring-8 is calculated as

$$\theta_d \approx \frac{1}{\gamma} = \sqrt{1 - \beta^2} = 0.06 \text{ [mrad]}. \quad (3.12)$$

Thus, SR has remarkable directionality due to the relativistic effect.

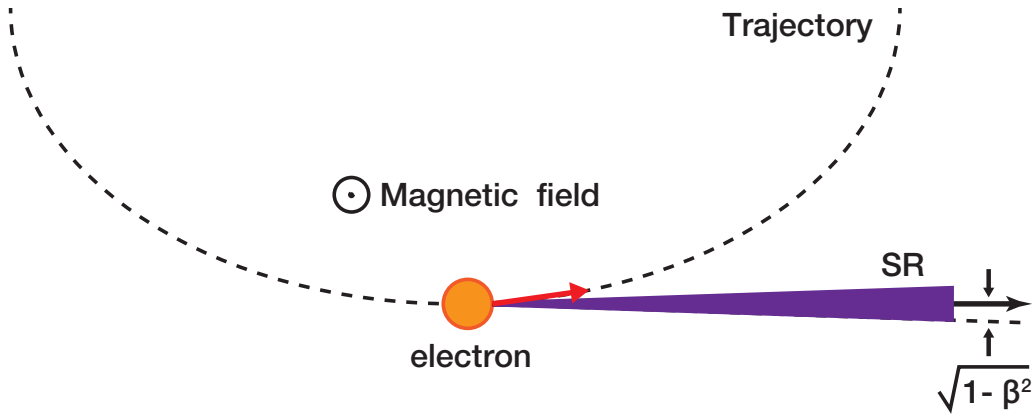


Figure 3-7: Generation of SR from an accelerated electron in a magnetic field.

### 3.3 Measurement systems

In this section, I will present a brief description of photoemission beamlines used in this thesis: the HHG photoemission beamline for Chapters 4 and 5 and the SR

photoemission beamline for Chapter 6.

### 3.3.1 HHG beamline

HHG beamline used in Chapters 4 and 5 belongs to Laser and Synchrotron Research Center at Institute for Solid State Physics, The University of Tokyo. This beamline is mainly composed by the following five components as illustrated in Fig. 3-8.

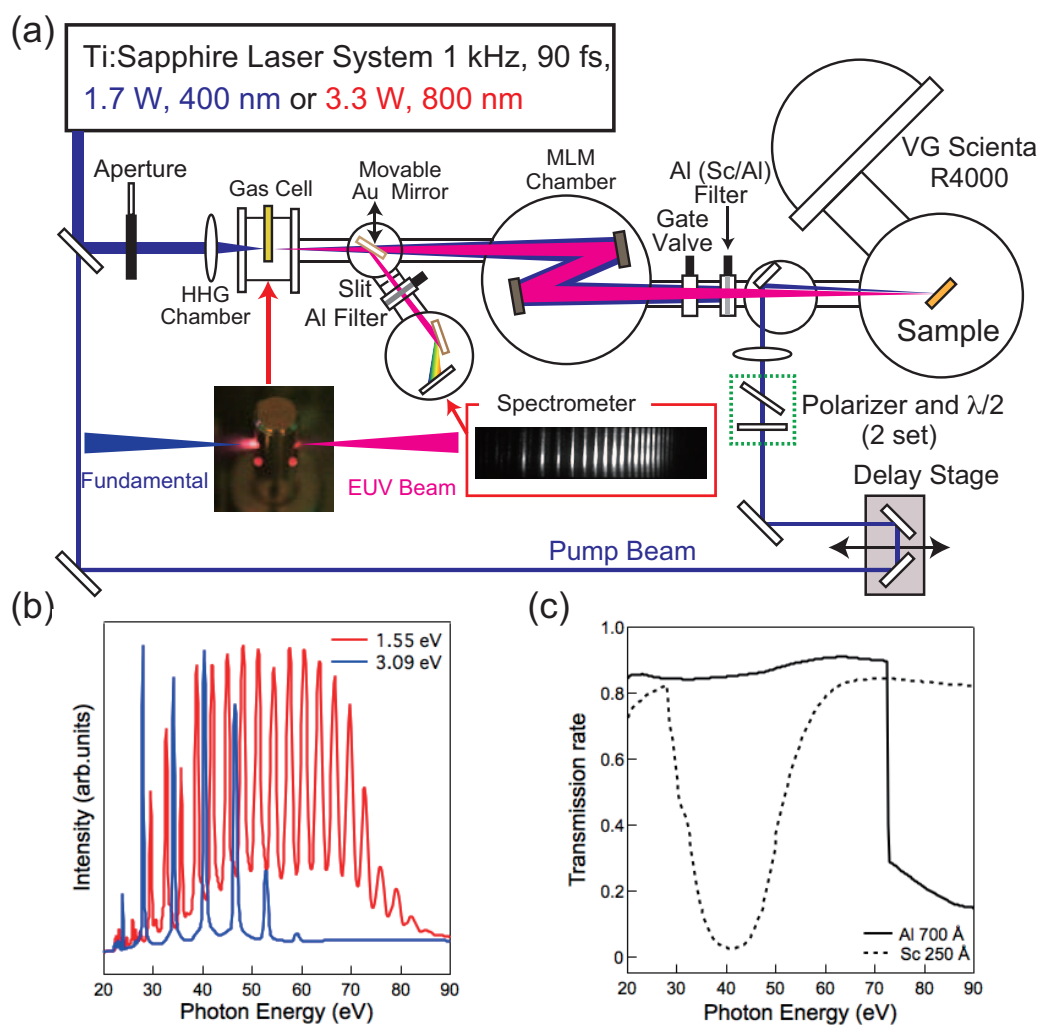


Figure 3-8: Schematic drawing of the HHG beamline [30]. (a) Overall view of the HHG beamline. (b) The energy spectra of high harmonics taken under different conditions. (c) The refractivity spectra of equipped Al and Sc filters.

#### I. Laser source

We use a commercial Ti:Sapphire regenerative amplifier system (Coherent Inc., Astrella) with the central wavelength of 800 nm, the repetition rate of 1 kHz, pulse duration  $\sim 30$  fs, and the laser power of 3.3 W. The fundamental laser can be converted to the second-harmonic wave (laser power : 1.7 W, wavelength : 400 nm) by passing through a  $\beta$ -BaB<sub>2</sub>O<sub>4</sub> (BBO) crystal. At the end of the laser systems, the laser beam is divided into a probing laser and a pumping laser by a perforated mirror.

## II. Gas-cell chamber

Gas-cell chamber contains a plano-convex lens with a focal length of 300 mm. This lens is used to focus the laser beam into a gas-cell. For a gas medium, Ne or Ar are used depending on the required HHG energy. The gas-cell is equipped with xyz-stages, which allow for accurate alignment of the gas-cell with respect to the beam and focus in order to maximize the HHG efficiency. Figure 3-8 (b) shows HHG spectra at different wavelengths using Ne gas. The spectra were taken by the spectrometer located after the gas-cell chamber.

## III. Multilayer mirror chamber

The generated HHG beam is then monochromated at a multilayer mirror (MLM) chamber. This chamber contains a pair of custom-order MLMs (NTT-AT). The reflectance spectrum of the mirror is optimized to the HHG energy depending on the layer period and materials of the mirror (for example, SiC/Mg, Zr/Al and Mo/Si). After the MLM chamber, Al and Sc-doped filters are equipped to cut the fundamental laser while transparent for the HHG energy region (Fig. 3-8 (c)).

## IV. Pumping laser line

The fundamental laser from Ti:sapphire laser systems is divided into two optical paths by a perforated mirror and the initial laser power of 1.7 W is clipped into several hundred milliwatt as a pumping laser. As shown in Fig. 3-8, two sets of a  $\lambda/2$  plate and a polarizer are installed on the pumping laser path to attenuate and continuously adjust the laser fluence. A fine-tunable delay stage is mounted on the fixed plate.

The step size of this delay stage is precisely controlled by a pulse generator with a minimal delay step of  $2 \mu\text{m}$  (6.67 fs for optical path length). In the real case, one has to consider round-trip paths and therefore the actual minimal step is  $4 \mu\text{m}$  (13.3 fs for optical path length). At the end of the pumping laser line, the incident pumping laser is loosely focused by a collective lens.

## V. Photoemission chamber

In the last part of the beamline, the probe and pump lights converge onto a sample both spatially and temporally. The electron analyzer is VG Scienta R4000 with 30 degree acceptance angle. The sample position is precisely and reproducibly arranged by pulse-controlled  $x$ ,  $y$ ,  $z$  and  $\theta$  manipulators. These four-axes ( $x$ ,  $y$ ,  $z$ ,  $\theta$ ) manipulators plus a fixed tilt angle allow one to conduct Fermi surface mapping. In the photoemission chamber, He discharge tube is equipped to perform static photoemission measurement. The photoemission measurement can be performed at various sample temperatures in the range of several Kelvin to room temperature under the control of a temperature regulator.

### 3.3.2 SR beamline

Time-resolved photoemission experiments in Chap. 6 were conducted by using angle-resolved time-of-flight (ARTOF) apparatus in BL07LSU beamline at SPring-8 (Fig. 3-9). In contrast to the HHG beamline, different light sources are utilized: SR for the probing light and laser for the pumping light. The timing between pump and probe are monitored by a high-speed oscilloscope and controlled electrically. Combination of a Ti:Sapphire oscillator and an amplifier provides ultrafast laser pulses with wavelength centered at 800 nm and pulse width of 35 fs. By tuning undulators and a monochromator, the photon energy of 250 to 2000 eV is available. A probe SR and a pump laser are focused on sample position and the timing can be monitored by photodiode (PD) located close to the sample position. The typical energy and the temporal resolution are 400 meV and 50 ps, respectively. More details about ARTOF apparatus can be found in Ref. [28].

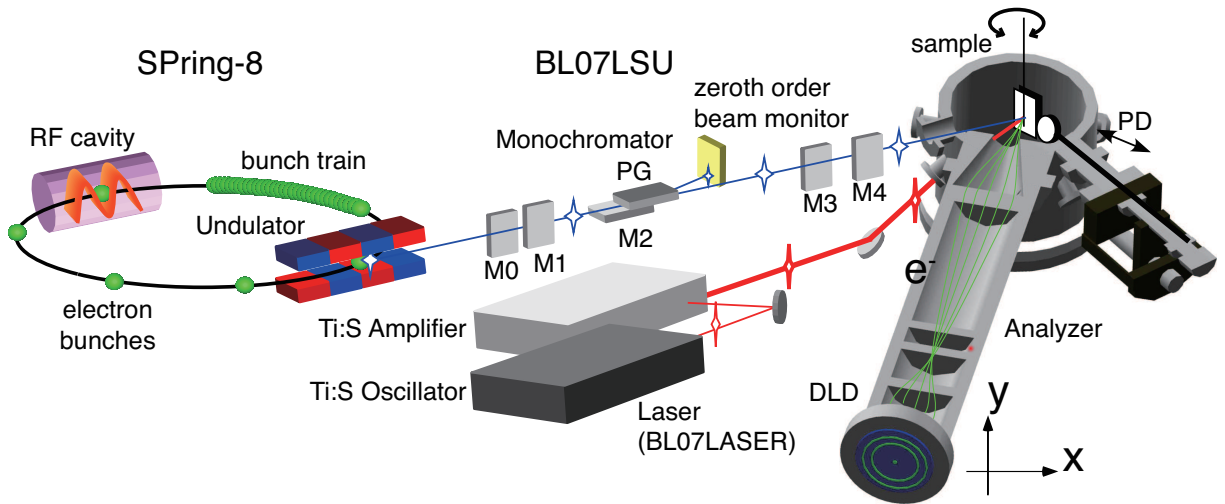


Figure 3-9: Schematic drawing of SR beamline. Figure is taken from [28].



# Chapter 4

## Ultrafast carrier dynamics in epitaxial graphene on Si-face SiC(0001)

### 4.1 Introduction

Monolayer or single-layer graphene [1, 31, 32] has recently attracted attentions in the research and technological fields of optoelectronic devices [2, 3, 7, 33–41]. While it has been necessary to unveil detailed mechanisms of the photo-induced phenomena of graphene [2, 35–38] for the development, the direct study of non-equilibrium carrier dynamics has been still rare. In this chapter, our graphene research on carrier dynamics is presented. We made time-resolved photoemission experiments to track variations of the Dirac electrons in *real time* after optical pumping. Temporal evolution of the spectral features, reflecting the hot carrier distribution of the linearly dispersing band, are well-characterized by the electronic temperature. The relaxation seems to be associated with the cascade carrier multiplication as reported previously [2].

## 4.2 Experimental

We carried out the photoemission experiment with the high-harmonic generation (HHG) laser system described in Sec. 3.3.1. We chose the photon energy at 28.26 eV, which we generated with Ar gas by ultrashort laser pulses of  $h\nu = 3.14$  eV. We recorded the time-resolved data by the pump (3.14 eV, 170fs-pulse duration) and probe (28.26 eV, 170fs-pulse duration) method. We set the repetition rate at 1 kHz. We determined the delay time of 0 by the reference graphite sample [24, 42]. The total time resolution during the experiment was 180 fs.

We prepared epitaxial graphene on an SiC substrate by annealing at 1650 °C under an Ar atmosphere ( $\sim 1$ bar) [14, 43] for one minute. In Fig. 4-1(a), a picture of the graphene sample is shown. After installation into an ultrahigh vacuum chamber, we made the clean surface by annealing at 500 °C. We verified crystallinity of the surface by low-electron-energy diffraction (LEED) (see Fig. 4-1(b)). We associated LEED spots with those of graphene ( $1 \times 1$ ), SiC ( $1 \times 1$ ) and the buffer layer ( $6\sqrt{3} \times 6\sqrt{3}$ ) [14].

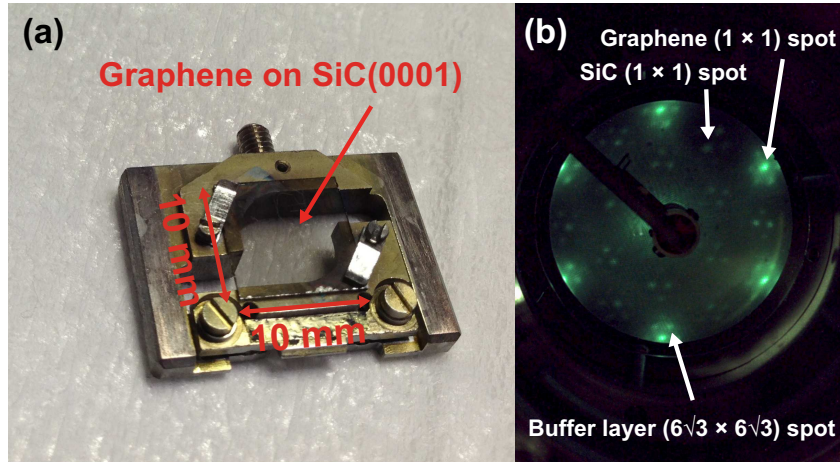


Figure 4-1: (a) Picture of n-type graphene sample on SiC(0001) substrate mounted on the sample holder. (b) LEED pattern of the graphene sample taken at the electron beam energy  $E_{beam} = 77.3$  eV.

## 4.3 Results and discussion

### 4.3.1 Space Charge Effect

A set of time- and angle-resolved photoemission spectra, taken at a delay time of 133 fs, are shown in Fig. 4-2. We recorded the individual data with various pumping powers. As indicated by an arrow in Fig. 4-2(a), the Dirac point (DP) is located at the binding energy of 0.39 eV before the pumping. As apparent in the spectra, the graphene on a SiC(0001) surface is n-type, which is consistent to the previous reports [14, 43].

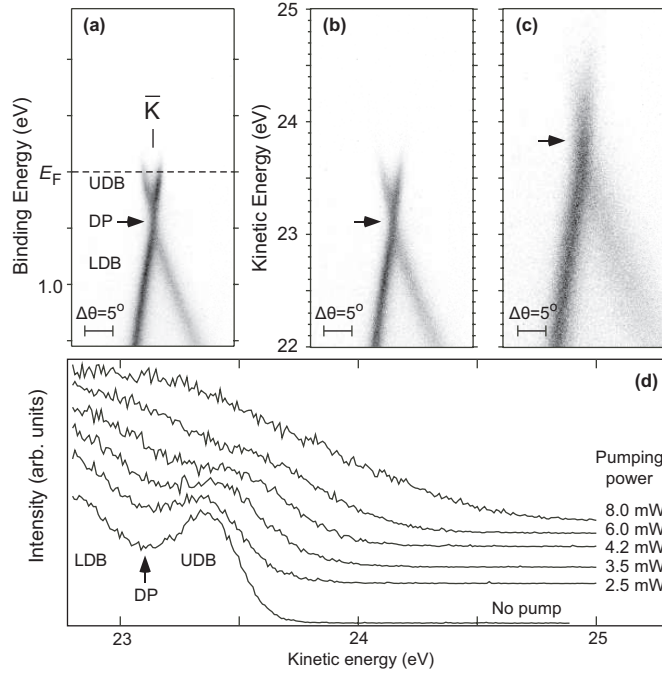


Figure 4-2: (a-c) Time- and angle-resolved photoemission diagrams of epitaxial graphene taken at a delay time of 133 fs and at pumping powers of (a) 0, (b) 2.5, and (c) 8.0 mW [44]. The data correspond to the wavenumber range around the  $\bar{K}$  point (cut along a line vertical to the  $\bar{\Gamma}-\bar{K}$  direction) of the two-dimensional Brillouin zone. The upper Dirac band (UDB) and the lower Dirac band (LDB) are labeled in the figure, and the Dirac point (DP) is indicated by an arrow. (d) Series of angle-integrated spectra taken at a delay time of 133 fs at various pumping laser powers.

As shown in Fig. 4-2(b), the Fermi edge becomes broad with the pumping power of 2.5 mW due to the rise in electronic temperature. When the power is 8.0 mW

(Fig. 4-2(c)), the photoelectron spectrum expands to a higher kinetic energy and, at the same time, the observed Dirac band structure is deformed largely. The spectral change with the pumping laser power can be systematically identified in Fig. 4-2(d). One can find that the spectrum, recorded at 2.5 mW, keeps the spectral feature of the Dirac bands but those with  $\geq 3.5$  mW show a distinctive energy shift and large spectral broadening toward higher kinetic energy. This feature originates from the space charge effect [45]: photo-excited electrons are accelerated by the Coulomb repulsion from other photoelectrons, which are generated by the pumping laser. This space charge effect becomes pronounced with increasing the pumping laser power and becomes non-negligible when pumping power is above 3.5 mW. In order to extract only genuine information from the photoemission data, we carried out time-resolved measurement with a laser power of 2.5 mW.

### 4.3.2 Time evolution of the electronic temperature

Figure 4-3 shows comparison of photoemission spectra at the Fermi level ( $E_F$ ) for two-dimensional fermions calculated using (a-c) the Schrödinger and (d-f) the Dirac-Weyl equations [32]. The density of states  $D(E)$  for the former case is constant with energy  $E$ , while  $D(E)$  for the latter case has linear dependence. The photoemission spectrum is proportional to the product of (a, d)  $D(E)$  and (b, e) the Fermi-Dirac function  $f_{FD}$ . Thus, the spectrum has a slope at the Fermi edge that decreases with increasing temperature and the spectral tail extends to a smaller binding energy, as shown in Fig. 4-3(c). The feature is typically found in metal samples. On the other hand, in the case of the Dirac Fermions in graphene, the Fermi edge has a peak-like structure (Fig. 4-3(f)) and, at higher temperatures, the peak top shifts toward a higher binding energy.

On the other hand, a set of the time-resolved energy distribution curves (EDCs) of a graphene is shown in Fig. 4-3(g). In the figure, raw experimental data are traced with thin colored lines while the fitting results (see Eq. (4.2), described below) are drawn with bold colored lines. At the delay time of 0 fs, the photoemission intensity of the upper Dirac band reduces significantly but that of the lower Dirac

band remains constant. As shown in the inset of Fig. 4-3(g), the slope of the spectral edge simultaneously becomes small, which is apparently confirmed by taking the derivative. Thus, observed spectral changes are identical to the computed results with various temperatures (Fig. 4-3(f)) and therefore, Fig. 4-3(g) describes the time evolution of the electronic temperature (the transient distribution of photo-excited carriers) in graphene.

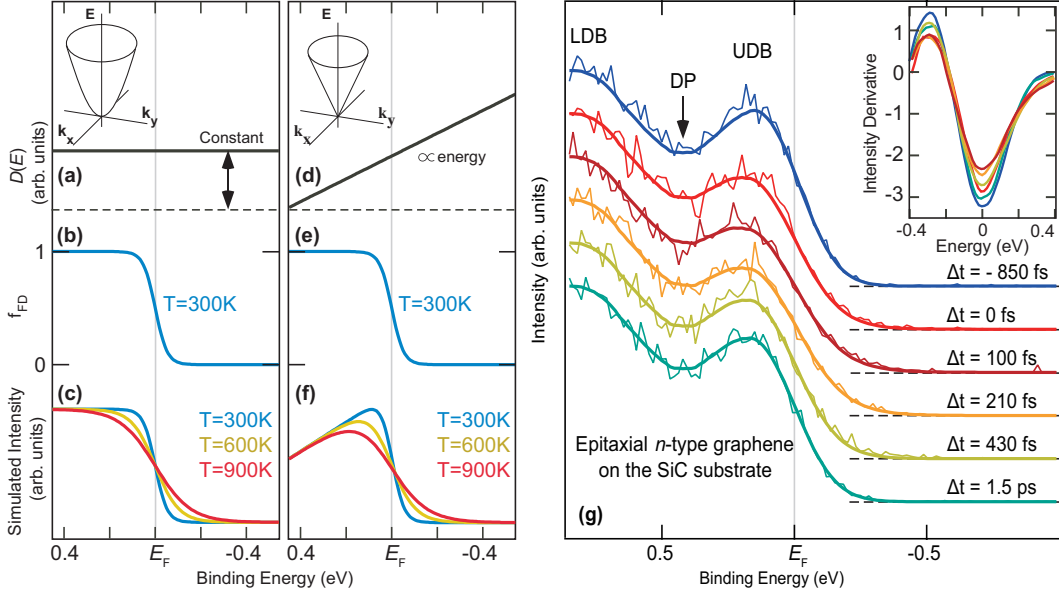


Figure 4-3: Calculation of the energy spectra in the two cases of (a-c) the Schrödinger and (d-f) the Dirac free electrons [44]. The inset shows their two-dimensional band dispersion. (a, d) The density of states ( $D(E)$ ), (b, e) the Fermi-Dirac function ( $f_{FD}$ ), and (c, f) the resulting spectra. (g) Comparison of the spectra at different delay times. The experimental spectra were taken at the photon energy of 28.26 eV at various delay times with pumping laser irradiation ( $h\nu = 3.14\text{ eV}$ , 2.5 mW). The intensity variation for the upper Dirac band (UDB) is clearly reproduced by the simulation result (f) while the intensity for the lower Dirac band (LDB) is unchanged. The inset in (g) shows the derivative spectra near the Fermi level ( $E_F$ ).

### 4.3.3 Transient chemical potential

In the time-resolved photoemission spectra, one can also recognize that there is another interesting phenomenon due to the linear  $D(E)$  shape, namely the “chemical

potential shift” in non-equilibrium states. In the case of the n-type graphene, there is a non-zero slope in the  $D(E)$  at the Fermi level. Thus, as the electronic temperature is raised, the chemical potential  $\mu$  moves towards the Dirac point to maintain the number of electrons within the graphene monolayer.

Figure 4-4(a, b) shows the chemical potential shift. We determined these values of  $\mu$  numerically from the conservation of the electron number described by the equation

$$\int D(E') f_{\text{FD}}(E', 0, 0) dE' = \int D(E') f_{\text{FD}}(E', T, \mu) dE'. \quad (4.1)$$

We thus obtain the  $\mu$ - $T$  curve shown in Fig. 4-4(c). Note that the symbol  $E_{\text{F}}$  so far denoted the equilibrium chemical potential value  $\mu$  (300 K).

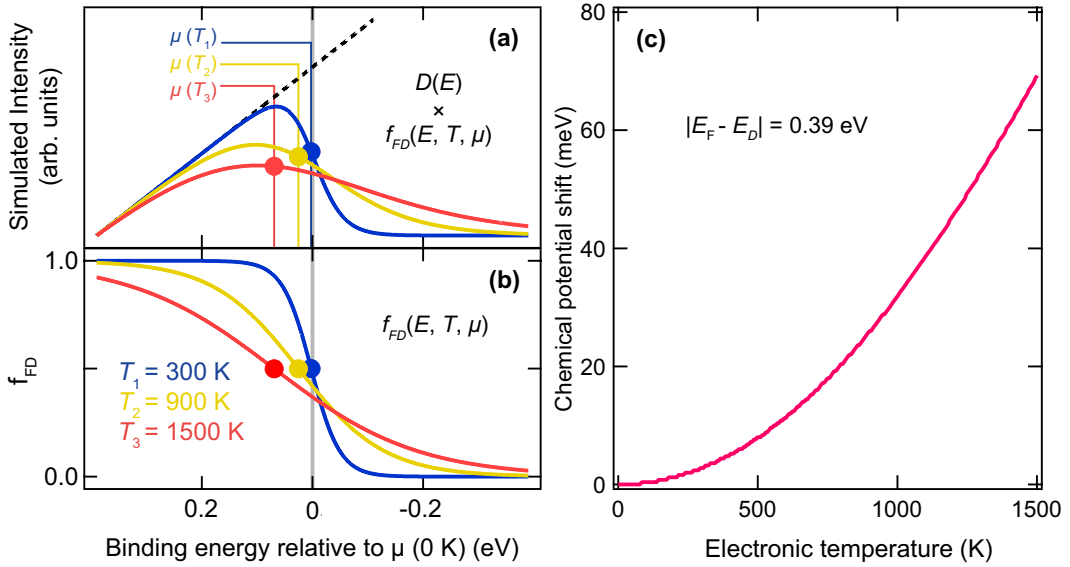


Figure 4-4: (a) Linear density of states (black dashed line) and the calculated spectra at various electronic temperatures (colored lines) calculated from  $D(E)$  and  $f_{\text{FD}}$  [44]. We adjust the chemical potential so that the density of states may be normalized. (b) Fermi–Dirac function for various electronic temperatures and chemical potentials (colored lines). Colored circles in (a, b) represent the position of the chemical potential at the corresponding electronic temperature. (c)  $\mu$ - $T$  curve for our n-type graphene sample. We set  $|E_{\text{F}} - E_{\text{D}}| = 0.39$  eV.

### 4.3.4 Carrier multiplication in n-type monolayer graphene

Figure 4-5(a) shows the delay-time-dependence of the electronic temperature (left axis) and peak intensity of the EDC derivative (right axis, see the inset of Fig. 4-3(g)). We determined the electronic temperature by curve fits of the TRPES spectra  $I(E, t)$  for a specific delay time with the following function [24, 46]:

$$I(E) = \int D(E') f_{\text{FD}}(E', T, \mu(T)) G(E - E', \sigma) dE', \quad (4.2)$$

where  $I(E)$  is the photoemission intensity of the TRPES spectra and  $G(E - E', \sigma)$  is a Gaussian with the width  $\sigma$  which corresponds to the experimental energy resolution, including that of the electron spectrometer and of the laser pulses;  $f_{\text{FD}}(E', T, \mu)$  is the Fermi–Dirac function at the electronic temperature  $T$  and the chemical potential  $\mu$ . The results of the fitting are shown in Fig. 4-3 by bold colored lines over the raw data (thin colored lines).

As shown in Fig. 4-5(a), the electronic temperature becomes as high as 900 K with a pumping laser power of 2.5 mW and, subsequently, relaxes on the fs time scale. The relaxation time, as determined from the exponential fit, was  $\sim 400$  fs for the present n-type graphene layer on the SiC substrate. These results are comparable to the relaxation time of several hundreds fs, which was previously reported for p-type graphene on an H-terminated SiC substrate [3, 39].

From the experimental data  $I(E, t)$ , we also observe the chemical potential shift for each value of the delay time by fitting the data  $I(E, t)$ , as shown in Fig. 4-4(a, b). In Fig. 4-5(b), we show the transient variation of the chemical potential shift from  $E_{\text{F}}$ . To make quantitative evaluation of the shift, the estimated shift values were plotted together with yellow circles in the graph. These values are taken from the  $\mu$ - $T$  curve in Fig. 4-4(c) at the corresponding electronic temperature of Fig. 4-5(a).

From the data, we can clearly identify the chemical potential shift relative to the chemical potential of the electrical ground of the measurement system. In the

equilibrium state, chemical potential of the sample have sufficient time to be aligned to the chemical potential of the ground by charge transfer. The observed chemical potential shift in time-resolved spectra indicates that the carrier redistribution takes longer than picoseconds to reach the equilibrium state.

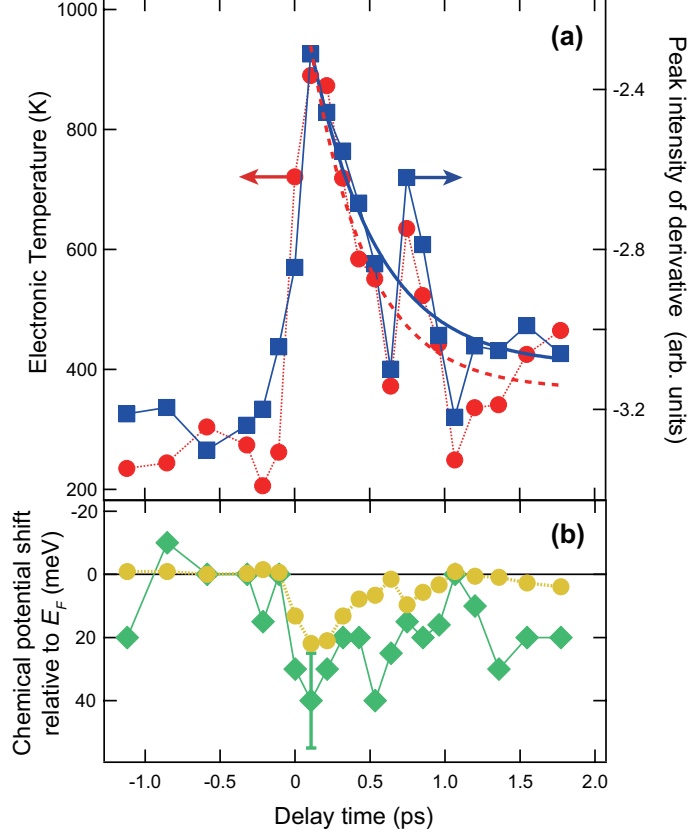


Figure 4-5: (a) Temporal evolution of the electronic temperatures (red circles) and intensity derivative values at the Fermi level (blue squares, taken from the inset of Fig. 4-3(g)) for epitaxial graphene on a SiC substrate [44]. Broken and solid curves are exponential curve-fits,  $\exp(-t/\tau)$ , for the electronic temperatures ( $1/\tau = 2.6 \pm 1.0 \text{ ps}^{-1}$ ) and the derivative values ( $1/\tau = 2.3 \pm 1.0 \text{ ps}^{-1}$ ), respectively. The pumping laser power was set at 2.5 mW. (b) Chemical potential shift corresponding to the electronic temperature at each delay time shown in (a) (yellow circles). These values are determined from the  $\mu$ - $T$  curve in Fig. 4-4(c). Green diamonds indicate the experimental  $\mu$  shift in this work with an error bar of  $\pm 15 \text{ meV}$ .

It has been reported previously that relaxation of photo-excited carriers in graphene accompanies cascade carrier multiplication (CM) via the Auger process [2]: when an electron is photo-excited in n-type graphene, the electron with a high energy (hot elec-

tron) multiply excites other electrons near the Fermi level through electron-electron scatterings, resulting in the generation of multiple carriers. The phenomenon was described in terms of the hot electron distribution that is characterized by the rise of the electronic temperature. The electronic temperature in the previous report [2] was estimated to be  $1215 \pm 165$  K for n-type graphene with  $|E_F - E_D| = 0.17$  eV when the system was optically pumped with  $h\nu = 3.1$  eV and the absorbed photon density of  $10^{11}$  cm $^{-2}$ . Since the present research was made with  $|E_F - E_D| = 0.39$  eV, we have to compensate the electronic heat capacity  $C_{el}$  for a comparison. The electronic heat capacity is given [2] as  $C_{el} = \frac{\pi^2}{3} D(|E_F - E_D|) k_B^2 T$  and  $|E_F - E_D|$  is proportional to energy (Fig. 4-3(d)). Then, the electronic temperature is evaluated to be  $833 \pm 105$  K in the previous study [2], which is close to 900 K that was measured in the present research. The consistency between the previous and present researches indicates that our time-resolved photoemission experiment also traces the hot carrier distribution which involves carrier multiplication process in n-type monolayer graphene.

## 4.4 Conclusion

In the research of this chapter, we made femtosecond time- and angle-resolved photoemission measurements for the Dirac band of epitaxial graphene on a SiC substrate. The delay-time-dependence of the spectra corresponded to the hot carrier dynamics in the linearly dispersing band. The carrier distribution was well-characterized by the electronic temperature. The dynamical phenomena was likely associated with cascade carrier multiplication as reported previously [2].



# Chapter 5

## Ultrafast carrier dynamics in epitaxial graphene on C-face SiC(000 $\bar{1}$ )

### 5.1 Introduction

Continued from Chapter 4, the research in this chapter is devoted to uncovering the carrier dynamics in graphene. To know the carrier dynamics is essential not only for designing graphene-based optoelectronic devices but also for improving their performance [33,47–54]. Understanding carrier dynamics in graphene has been tried by various spectroscopic experiments, such as time- and angle-resolved photoemission spectroscopy (trARPES) [3,39,44,55–58], transient transmissivity (reflectivity) measurements [2,37,59–62], and time-resolved photoluminescence spectroscopy [63–65]. These previous researches unveiled that hot carriers lose most of their energy via electron–optical-phonon scattering in the first several hundred femtoseconds and then get cold through electron–acoustic-phonon scattering or optical-phonon–acoustic-phonon decay [59,60]. However, the reported values on the carrier lifetime in graphene are quite different among literatures. Table 5.1 shows the reported carrier lifetimes of some graphene samples. One can recognize the large variations in carrier lifetime

even for the same type of graphene samples, indicating the existence of extra cooling pathways that may exhibit a strong sample dependence.

Table 5.1: Reported carrier lifetimes in graphene.

| Sample                            | Lifetime (fs) | Measuring method         | Ref. |
|-----------------------------------|---------------|--------------------------|------|
| Si-face graphene                  | 400           | trARPES                  | [44] |
| Si-face graphene                  | 500           | trARPES                  | [56] |
| Si-face graphene (H-intercalated) | 2700          | trARPES                  |      |
| Si-face graphene (H-intercalated) | 700           | trARPES                  | [39] |
| CVD graphene on SiO <sub>2</sub>  | 4000          | transient transmissivity | [62] |

Recently, a new energy dissipation mechanism, called supercollisions (SCs), was predicted by Song *et al.* as a cooling channel in graphene via disorder-mediated electron–acoustic-phonon scattering [4]. The SC is a three-body collision that involves an electron, a defect, and an acoustic phonon. In general, a scattering channel by an acoustic phonon transfer much lower energy than that by an optical phonon. The phase space available for the acoustic-phonon scattering is restricted because of the momentum conservation in the linear dispersion, and hence the acoustic-phonon scattering becomes an inefficient cooling channel. When disorders induce additional exchanges for acoustic phonons to use a much wider phase space, the photo-excited carriers can have a larger energy dissipation. In this way, SC can become an efficient cooling pathway. Observation of the SC channel was indeed reported in suspended [66] and substrate-supported [3, 67–69] graphenes. It has now become highly called to clarify interplays between carriers, optical phonons, acoustic phonons and defects in

photo-excited carrier dynamics in graphene.

We carried out trARPES on graphene on a SiC(000 $\bar{1}$ ) C-terminated surface that has the intrinsic carrier mobility exceeding  $100,000 \text{ cm}^2 \text{ V}^{-1} \text{ s}^{-1}$  [70]. This high carrier mobility indicates the defect density of the graphene is much fewer than other graphene samples studied so far (for example, the intrinsic carrier mobility of Si-face graphene is reported to be  $\sim 1,000 \text{ cm}^2 \text{ V}^{-1} \text{ s}^{-1}$  [14, 71]). Thus, we expect the suppression of the SC cooling process in the high mobility graphene, and this feature make it possible to reveal intrinsic carrier dynamics in graphene such as electron-phonon scattering and phonon-phonon scattering.

## 5.2 Experimental

The experiments were made on trilayer graphene on SiC(000 $\bar{1}$ ). By annealing semi-insulating 6H-SiC(000 $\bar{1}$ ) at 1320 °C for 10 minutes under an Ar atmosphere (1 bar), the trilayer graphene is epitaxially grown on the substrate. The sample was transferred into an ultrahigh vacuum chamber and subsequently cleaned by annealing at 500 °C for removing contamination. We verified crystallinity of the cleaned surface by observation of a low-electron-energy diffraction (LEED) pattern. Analyzing ARPES spectra with a He I $\alpha$  source showed our sample consists of 3 layers of graphene and there is no carrier doping from the SiC substrate i.e.  $E_F = E_D$  where  $E_D$  denotes the energy position of the Dirac point. The intrinsic carrier mobility of the sample was evaluated to be  $100,000 \text{ cm}^2 \text{ V}^{-1} \text{ s}^{-1}$  from transport measurements of a top-gated graphene field-effect transistor [70].

We carried out the photoemission experiment with the high-harmonic generation (HHG) laser system as described [30, 42] in Sec. 3.3.1. In the time-resolved photoemission experiments, we used a pulse of the 27.9-eV HHG laser as a probe and the fundamental laser ( $h\nu = 1.55 \text{ eV}$ ,  $360 - 1650 \mu\text{J}/\text{cm}^2$ ) as a pump. The temporal resolution was 80 fs, while the energy resolution was 250 meV. We made the measurements at 20 K and at room temperature.

## 5.3 Results and discussion

### 5.3.1 Transient hot carrier distribution in the Dirac cone

We present a series of trARPES spectra, measured at room temperature, in Fig. 5-1(a-f). The graphene sample was pumped by 1.55 eV laser ( $660 \mu\text{J}/\text{cm}^2$ ). At the equilibrium state before irradiation, only the lower Dirac cone is visible for the present graphene sample (Fig. 5-1(a)). After optical pumping, the upper Dirac cone appears at the previously unoccupied region (Fig. 5-1(b-f)). In order to highlight the non-equilibrium feature, we subtract trARPES photoemission band diagram from the original equilibrium state. The differential data are displayed in Fig. 5-1(g-k) where the scaled red/blue dots mean the increase/decrease of photoemission intensities from the original. Figure 5-2(b-e) shows a set of the transient electronic temperatures measured under different pumping fluences. The initial temperature was set at 20 K. The electronic temperatures can be extracted from the angle-integrated spectra, as described in the last chapter [24, 44]:

$$I(E) = \int D(E')f(E', T_e)G(E - E', \sigma)dE', \quad (5.1)$$

where  $I(E)$  is the photoemission intensities spectrum,  $D(E')$  is the density of state (DOS) of graphene,  $G(E - E', \sigma)$  is the Gaussian of width  $\sigma$  as determined by the experimental energy resolution and  $f(E', T_e)$  is the Fermi–Dirac function at electron temperature  $T_e$ . The colored dots in Fig. 5-2(b-e) show the fitted results by Eq. (5.1) (see Appendix A for the fitting procedure). One can find two distinctive decay regimes in all fluence data: fast ( $70 \text{ fs} < t < 800 \text{ fs}$ ) and slow ( $t > 800 \text{ fs}$ ) which are apparent from the double exponential fitting in Fig. 5-3. These results help us to unveil energetic interchanges between the electronic and phononic systems including energy dissipation via SCs.

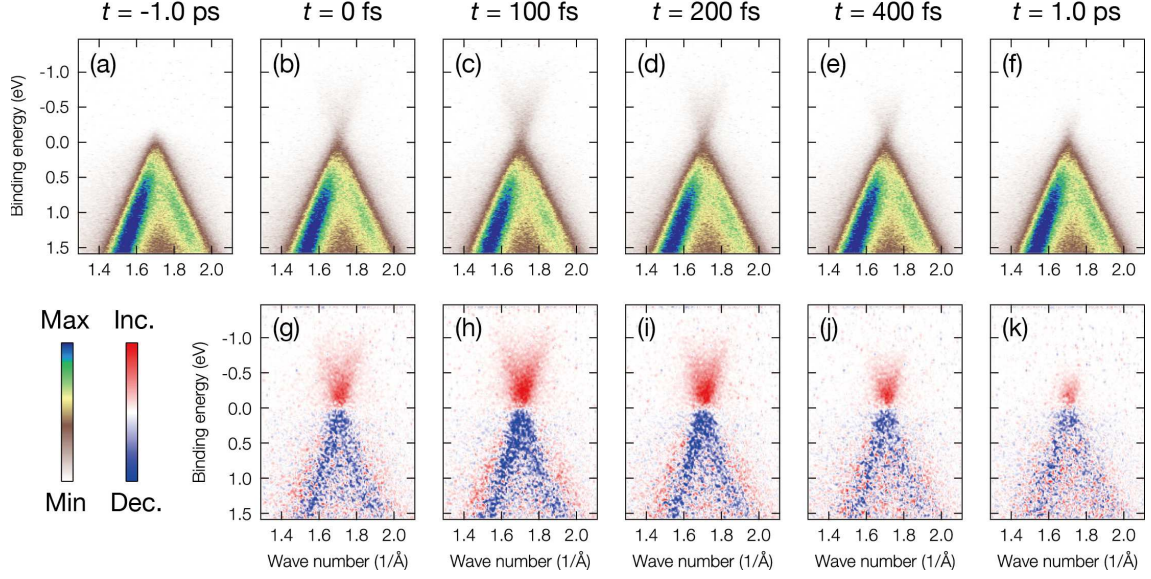


Figure 5-1: Time evolution of ARPES images taken along the  $\bar{\Gamma} - \bar{K} - \bar{M}$  direction. (a–f) Series of trARPES spectra taken at specified delay times [72]. The sample is excited with pumping energy of 1.55 eV at  $660 \mu\text{J}/\text{cm}^2$ . All spectra are measured at room temperature. (g–k) Difference spectra at the corresponding delay times given in (b–f) obtained by subtracting (a) from each spectrum; the scale red/blue dots indicate increase/decrease from the photoemission intensities at the equilibrium state.

### 5.3.2 Relaxation model for electron-phonon and electron-defect scatterings

The optical-phonon modes in electron-phonon scattering in graphene is governed by the doubly degenerate intravalley  $E_{2g}$  modes at the zone center ( $\Gamma$  point) and the intervalley  $A'_1$  mode at the zone corners (K or  $K'$  point). All the other phonon modes at the  $\Gamma$  and K points contribute negligibly [73, 74]. Energies for the intravalley  $E_{2g}$  and intervalley  $A'_1$  modes are 196 meV and 160 meV, respectively. The carrier recombination (optical-phonon emission) rates ( $R$ ) and the carrier generation (optical-phonon absorption) rates ( $G$ ) for electron–optical-phonon scatterings are proposed by Rana *et al.* [74], as in the following expressions (in units  $\text{cm}^{-2}\text{s}^{-1}$ ):

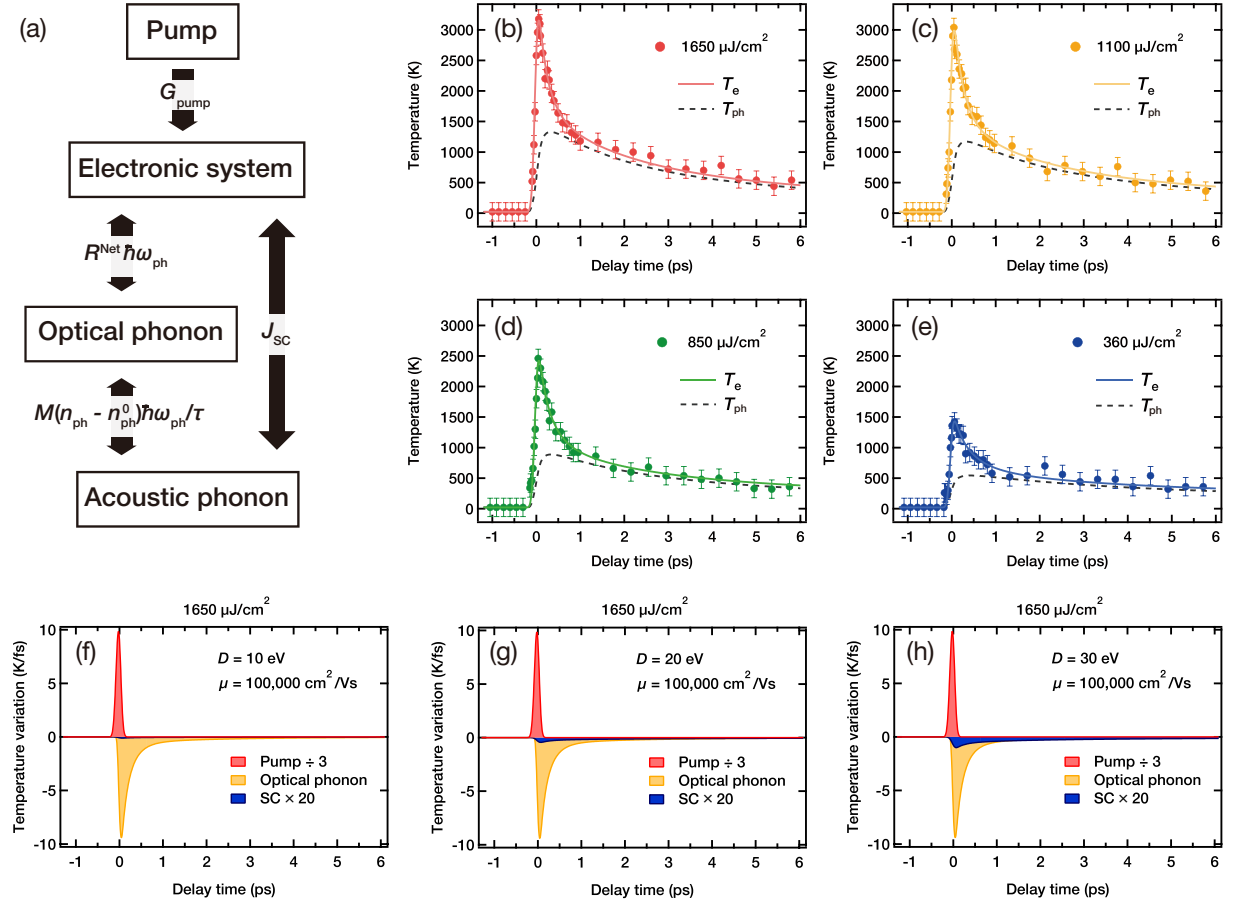


Figure 5-2: Time evolution of the electronic temperatures and the results of the fittings [72]. (a) Energy flow diagrams between the electronic and phononic systems corresponding to the rate equations (5.5)–(5.6). (b–e) The electronic temperature relaxations under several excitation conditions. Electronic temperatures extracted from Eq. (5.1) are shown in colored solid dots with fitting error bars of  $\pm 100$  K. The curves for  $T_e$  and  $T_{ph}$  at each fluence data are obtained by solving the rate Eqs. (5.5)–(5.6), under the carrier mobility  $\mu = 100,000$   $\text{cm}^2/\text{Vs}$  and deformation potential  $D = 30$  eV. (f–h) Influence of the SC process on the cooling of the photo-excited carriers.

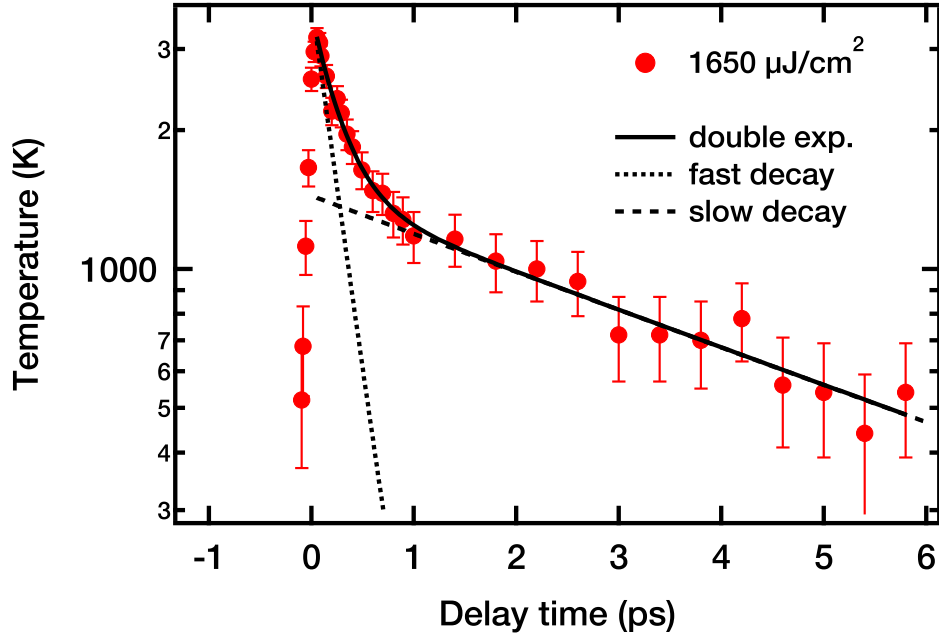


Figure 5-3: Semi-logarithmic plot of Fig. 5-2(b) and the result of the double exponential fitting shown as a solid line consisting of fast and slow components (broken lines). The relaxation time constants for fast and slow decays are  $270 \pm 30$  fs and  $5200 \pm 500$  fs, respectively. The fast decay line is offsetted to follow the double exponential line for eye-guide.

$$\begin{aligned}
 R = \frac{9}{2} \left( \frac{\partial t}{\partial b} \right)^2 \frac{1}{\pi \rho \omega_{\text{ph}} \hbar^4 v_{\text{F}}^4} \int_{-\infty}^{\infty} dE | E || E - \hbar \omega_{\text{ph}} | \\
 \times f(E, T_e) (1 - f(E - \hbar \omega_{\text{ph}}, T_e)) (1 + n_{\text{ph}}), \quad (5.2)
 \end{aligned}$$

$$\begin{aligned}
 G = \frac{9}{2} \left( \frac{\partial t}{\partial b} \right)^2 \frac{1}{\pi \rho \omega_{\text{ph}} \hbar^4 v_{\text{F}}^4} \int_{-\infty}^{\infty} dE | E || E + \hbar \omega_{\text{ph}} | \\
 \times f(E, T_e) (1 - f(E + \hbar \omega_{\text{ph}}, T_e)) n_{\text{ph}}. \quad (5.3)
 \end{aligned}$$

Here,  $v_F = 1 \times 10^6$  m/s is the Fermi velocity,  $\rho = 7.6 \times 10^{-7}$  kg/m<sup>2</sup> is the density,  $\omega_{\text{ph}}$  is the angular frequency for intravalley (196 meV/ $\hbar$ ) and intervalley (160 meV/ $\hbar$ ) optical-phonon modes and  $n_{\text{ph}}$  is the phonon population.  $n_{\text{ph}}$  follows the Bose-Einstein distribution at the phononic temperature  $T_{\text{ph}}$ .  $\partial t/\partial b$  is related to the electronic energy change by the bond length displacement. A quantity  $t$  represents the transfer integral, while  $b$  is the distance between nearest carbon atoms.

It has been argued [4] that carrier dynamics is affected not only by electron-optical-phonon scattering but also by SC cooling events. The energy loss rate of SCs, which we denote by  $\mathcal{J}_{\text{SC}}$ , depends on the electrical transport properties, such as the mean free path, the electric conductivity, and the carrier mobility [4]. The expression for  $\mathcal{J}_{\text{SC}}$  takes the form

$$\mathcal{J}_{\text{SC}} \sim 8.8 \times 10^{14} \times \frac{D^2}{\mu} (T_e^3 - T_{ac}^3) \left[ \frac{\text{eV}}{\text{cm}^2 \text{K}^3 \text{s}} \right], \quad (5.4)$$

where  $D \sim 10 - 30$  eV [67, 75–78] is the deformation potential,  $\mu$  is the intrinsic carrier mobility (with units cm<sup>2</sup>V<sup>-1</sup>s<sup>-1</sup>), and  $T_{ac}$  is the acoustic phonon temperature, which is assumed to be unchanged from the equilibrium state [3] (see Appendix B for details of the derivation of Eq. (5.4)).

Using these factors, we built a comprehensive relaxation model for photo-excited carriers in graphene based on phenomenological two-temperature models [59, 61, 62]:

$$\frac{dT_e}{dt} = \frac{G_{\text{pump}}}{C_e} - \frac{R^{\text{Net}} \hbar \omega_{\text{ph}}}{C_e} - \frac{\mathcal{J}_{\text{SC}}}{C_e}, \quad (5.5)$$

$$\frac{dn_{\text{ph}}}{dt} = \frac{R^{\text{Net}}}{M} - \frac{n_{\text{ph}} - n_{\text{ph}}^0}{\tau}. \quad (5.6)$$

In Fig. 5-2(a), we schematically summarizes the energy interactions (transferred en-

ergy per unit area and unit time) among above coupled rate equations. Here  $R^{\text{Net}}$  is the total balance between the recombination rate and the generation rate;  $R^{\text{Net}} = R - G$ .  $M$  denotes the number of phonon modes in the available phase space for the carrier-phonon scattering. Its magnitude is determined by the pumping laser energy  $E_{\text{pump}}$ , given as [59]  $2 \times [(E_{\text{pump}}/2)/\hbar v_{\text{F}}]^2/4\pi$ .  $G_{\text{pump}}$  represents the energy injected into the sample during laser irradiation that is assumed to be of Gaussian form with a full-width at half-maximum of 70 fs.  $C_e$  represents the specific heat of the electronic system assumed to be proportional to the square of the electronic temperature [79]. Therefore, for undoped graphene,  $C_e = \alpha T_e^2$  where  $\alpha$  equals  $8.14 \times 10^{-17} \text{ J K}^{-3} \text{ cm}^{-2}$ .  $n_p^0$  is the initial phonon population at 20K.  $\tau$  dominates the anharmonic decay process of the optical phonon to the acoustic phonon [80].  $G_{\text{pump}}$ ,  $M$ ,  $\partial t/\partial b$ , and  $\tau$  are the fitting parameters for these rate equations. The phonon population  $n_{\text{ph}}$  is converted to a phononic temperature  $T_{\text{ph}}$  by inverting the equation for  $n_{\text{ph}}$ , specifically,  $T_{\text{ph}} = \hbar\omega_{\text{ph}}/k_B \ln[(1 + n_{\text{ph}})/n_{\text{ph}}]$ .

### 5.3.3 Suppression of supercollision carrier cooling process

Figure 5-2(b–e) presents the fitted results for  $T_e$  and  $T_{\text{ph}}$  for each pumping fluence by setting  $\mu = 100,000 \text{ cm}^2\text{V}^{-1}\text{s}^{-1}$  and  $D = 30 \text{ eV}$ . Applied fitting parameters are almost identical for all fluence data except for  $G_{\text{pump}}$  (see Appendix C for details of fittings). This confirms that Eqs. (5.5)–(5.6) are valid for describing the carrier dynamics in graphene. It is of note that temporal evolution of these temperatures includes a Gaussian function of width 80 fs that corresponds to the temporal resolution. Figure 5-2(f–h) compares individual terms in the calculation results for  $dT_e/dt$  (right-hand side of Eq. (5.5)) at the pumping power of  $1650 \mu\text{J}/\text{cm}^2$ . To be specific, the heating/cooling rates using the pumping laser ( $G_{\text{pump}}/C_e$ ), optical phonons ( $R^{\text{Net}}\hbar\omega_{\text{ph}}/C_e$ ) and SCs ( $\mathcal{J}_{\text{SC}}/C_e$ ) are presented separately. When one compares the cooling power by SCs (integral of the blue area) with respect to the total cooling power (sum of integral of the yellow and blue areas), we found that SCs contribute with carrier cooling ratio of only about 0.1, 0.5, and 1.1 % for deformation potential values of  $D = 10, 20, \text{ and } 30 \text{ eV}$ , respectively. This fact indicates that SCs do not have essential

roles in decreasing the electronic temperature in extremely high-mobility graphene.

The result is reasonable considering the mean free path  $l$  and scattering time  $\tau_s$ . If one assumes  $l$  of the present C-face graphene to be  $\geq 200$  nm, reported previously for highly oriented pyrolytic graphite (HOPG) with mobility  $\mu = 50,000 \text{ cm}^2\text{V}^{-1}\text{s}^{-1}$  [81], we obtain  $\tau_s \geq 200$  fs with the relation  $l = v_F\tau_s$ . This time scale is comparable with the fast decay process found in Fig. 5-2. Namely, SC is expected to occur several times during the fast decay regime. On the other hand, as for a Si-face graphene, the mean free path is estimated at 4 nm [3]. This much shorter scattering time ( $\tau_s = 4$  fs) results in a large energy dissipation via hundreds of SC events. Therefore, the observed transient electronic temperature in the Si-face graphene could not be quantitatively described without including the SC term in their rate equations, as reported previously [3]. It is of note that recent trARPES study [82] showed that optical-phonon decays describe the energy relaxation with no SCs during the carrier cooling in HOPG. This is closely related to the our findings and scenario.

### 5.3.4 Carrier cooling mechanism in high mobility graphene

We can now fairly derive our discussion that the carrier dynamics of the present graphene sample is sufficiently described by considering only electron–optical-phonon and optical-phonon–acoustic-phonon scatterings. Thus, we elaborate the electron–optical-phonon scattering by making evaluation of the  $R$  and  $G$  integrands. In Fig. 5-4(b-f), the calculated emission (absorption) rate of the intravalley  $E_{2g}$  optical-phonon modes is presented at each energy level (value of  $D$  is set to 30 eV). In the case of the optical-phonon emission, three initial electron energy regimes are found in Fig. 5-4(a). They are (i)  $E - E_F > 196$  meV (intraband scattering), (ii)  $196 \text{ meV} > E - E_F > 0$  meV (interband scattering), and (iii)  $0 \text{ meV} > E - E_F$  (intraband scattering).

By making comparisons of the number of electrons emitted at individual energy regime, we can model hot-electron relaxation and explain the origin of the relaxation bottleneck after  $t = 800$  fs. At the initial decay ( $70 \text{ fs} < t < 800 \text{ fs}$ ), the number of the emitted optical phonons (integral of red shaded area) exceeds that of absorbed optical phonons (integral of blue shaded area) (Fig. 5-4(b,c)). This indicates that

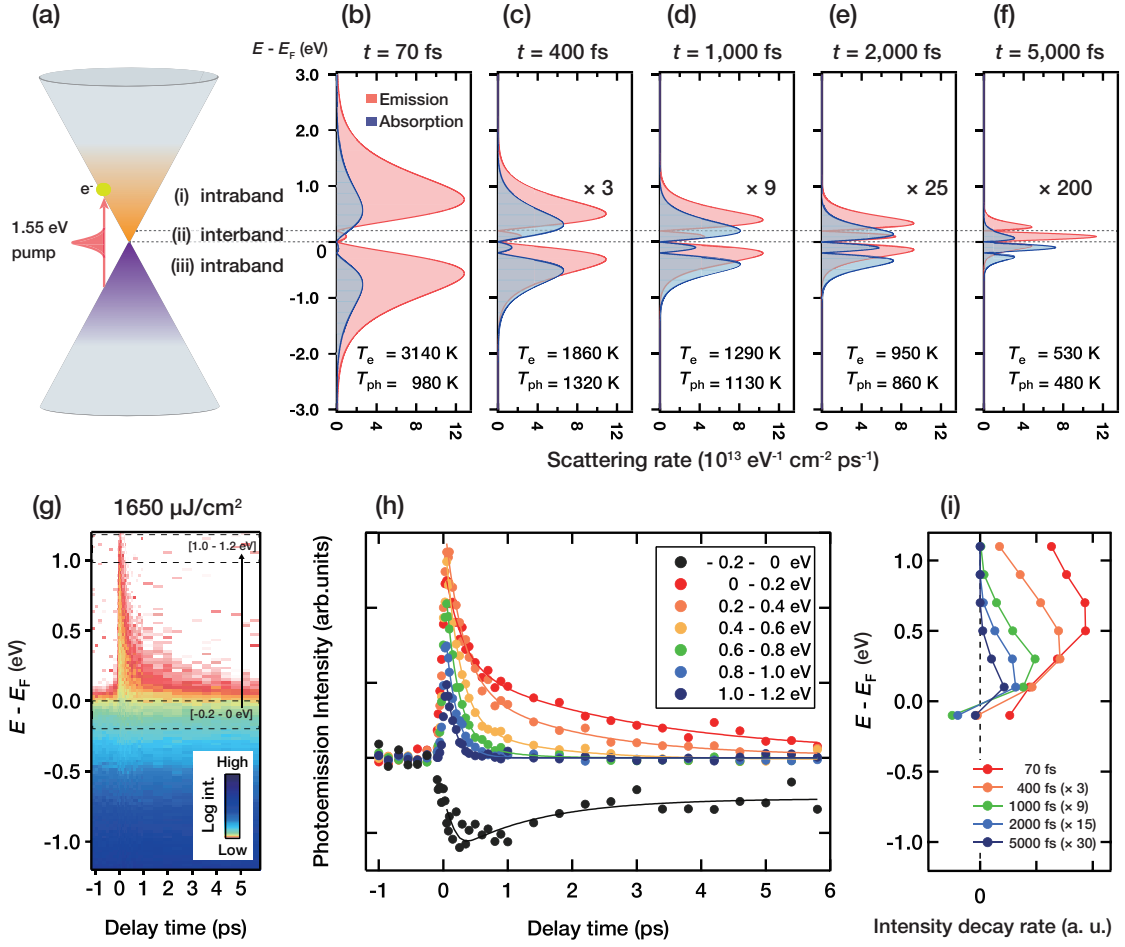


Figure 5-4: Calculated rates for electron–optical-phonon scattering [72]. (a) Schematic curve for the hot electron distribution has three characteristic energy regimes: electrons at energies below  $\hbar\omega_{\text{ph}} = 196$  meV step over the conduction band to valence band via optical-phonon emission (labeled (ii) interband) whereas others are scattered within the same band ((i, iii) intraband). (b–f) The energetic distributions of the number of electrons that participate in optical-phonon emission (red) and absorption (blue) per unit time (ps) and unit area ( $\text{cm}^2$ ) are obtained from the integrand of Eqs. (5.2) and (5.3), respectively, as a function of  $E - E_F$ . (g) Transient energy distribution of emitted photoelectrons excited by a 1.55-eV pumping laser at  $1650 \mu\text{J}/\text{cm}^2$ . (h) Temporal variation of the photoemission intensities (colored circles) collected every 0.2 eV step from -0.2 eV to 1.2 eV, for example, dashed boxes in (g). Colored lines indicate the fitting curves. (i) Photoemission decay rates, i.e., temporal differentiations of (h) at specified delay times are displayed as a function of  $E - E_F$ .

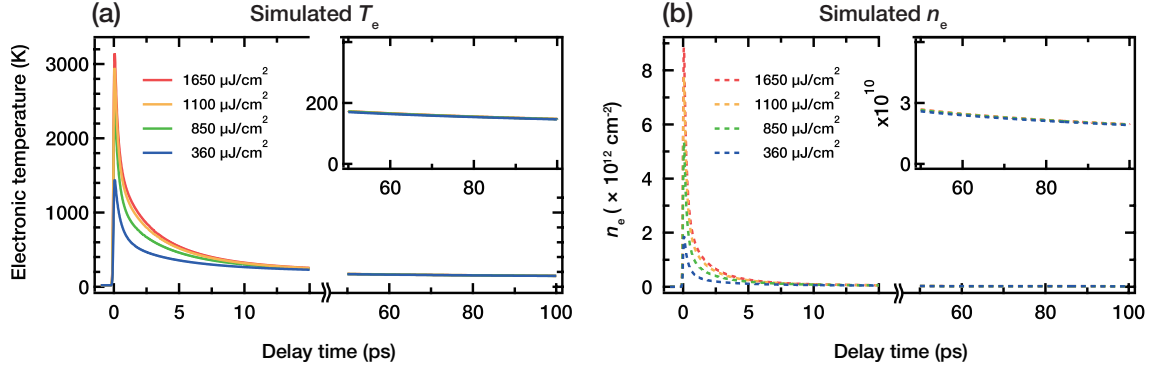


Figure 5-5: (a, b) Calculated electronic temperatures  $T_e$  and carrier densities  $n_e$  for several pump conditions are displayed in the long time domain. The insets show enlarged views for delay times of 50–100 ps.

the optical-phonon system obtains energy from the electronic system, resulting in a rapid rise (fall) in the phononic (electronic) temperature (see Fig. 5-2(b)). On the other hand, after  $t = 800$  fs, the optical-phonon emission and absorption reach almost equal to each other (Fig. 5-4(d-f)). Since the net optical phonon emission decreases, the energy transfer is restrained between these systems. Thus, after  $t = 800$  fs, the relaxation of the electronic temperature is strongly suppressed because of this reason. This is, in fact, also apparent from Fig. 5-2(b-e) where the electronic and phononic temperatures become almost the same at  $t = 800$  fs. It is of note that this kind of the bottleneck effect were also reported in the consistent time scale in the previous studies [3, 59–62].

To make comparisons with results of the calculation, Fig. 5-4(g-i) shows the experimental data of the energy-resolved decay rate for hot electrons excited by fluence of  $1650 \mu\text{J}/\text{cm}^2$  (corresponding to Fig. 5-2(b)). Figure 5-4(h) shows transient photoelectron intensities  $I(t)$  that are separately collected from specified energy region; 0.2-eV step (close to the  $\Gamma$  and K optical phonon energies) from -0.2 eV to 1.2 eV as illustrated by dashed boxes in Fig. 5-4(g). As we evaluate intensity decay rate  $dI(t)/dt$ , we can determine the energy distribution of the hot electron decay rates as displayed in Fig. 5-4(i) where the decay weight moves from intraband ( $t = 70$  fs) to interband ( $t = 5000$  fs) scattering regime. This shows a similar trend to the calculated

electron–optical-phonon scattering rates (Fig. 5-4(b-f)).

In addition, it is of note that when the electron distribution approaches the Dirac point, the cooling of the electronic system may be further reduced through the bottlenecks effect [65,83]. In the condition of  $E_D = E_F$ , an electron in the initial energy state well above the Dirac point can easily relax to a lower energy state. On the other hand, it is not possible for an electron initially near the Dirac point since the DOS of the final state is much smaller than that in the former case. Thus, for the electron distribution at the Dirac point, relaxation of the electronic temperature is significantly limited (see Fig. 5-4(f), for example).

In Fig. 5-5(a, b), the calculated results are shown for the electronic temperatures  $T_e$  and carrier densities  $n_e$  at the pumping fluence of  $360 - 1650 \mu\text{J}/\text{cm}^2$  in the long-time domain ( $-1 \text{ ps} \sim 100 \text{ ps}$ ). These results after 6 ps are calculated from the fitting parameters derived from Figs. 5-2(b-e). As shown in the inset of Fig. 5-5(a),  $T_e$  has still remained unrelaxed from the initial temperature of 20 K even until 100 ps. This is due to the fact that cooling of  $T_e$  further stagnates around 5 – 10 ps where the bottleneck effect of the Dirac point likely becomes effective. The electron distribution indeed accumulates near the Dirac point and the scattering channel is dominated by the interband optical-phonon emission (Fig. 5-4(f)). Results of the long time-domain measurement exhibits fair agreement with Fig. 5-5(b) (see Appendix D).

## 5.4 Conclusion

In this chapter, we describe trARPES experiment on C-face epitaxial graphene on SiC(000 $\bar{1}$ ). The observed transient electronic temperature is composed of fast ( $70 \text{ fs} < t < 800 \text{ fs}$ ) and slow ( $t > 800 \text{ fs}$ ) decay regimes. These temporal features are successfully reproduced by a numerical calculation based on coupled rate equations. The model calculation of the phonon emission/absorption rate shows that the slow decay process originates from the suppression of energy exchanges between carriers and optical phonons as well as from the suppression of zero DOS near the Dirac point (the bottleneck effect). The present research revealed the influence of SCs on carrier cool-

ing in graphene. Through comparison of its effect with competing cooling processes, such as optical-phonon scattering, we proved that the SC has negligible contribution to the carrier cooling in high-mobility graphene. This is the first demonstration of the suppression of SC carrier cooling in graphene. Our results provide apparent guidelines not only for designing graphene-based devices but also for improving their performance.

# Chapter 6

## Charge transfer dynamics at graphene/SiC interface

### 6.1 Introduction

It has been discussed how an interface structure, such as a buffer layer, affects electronic and optical properties of graphene on SiC substrate. In fact, the carrier mobility of graphene grown on C-face SiC(000 $\bar{1}$ ) shows  $\sim 10,0000 \text{ cm}^2 \text{ V}^{-1} \text{ s}^{-1}$  at room temperature, which is close to that of an ideal free-standing graphene, while that of graphene grown on Si-face SiC(0001) is reduced to  $\sim 1,000 \text{ cm}^2 \text{ V}^{-1} \text{ s}^{-1}$  [14, 71]. Recent studies revealed that these large differences originate from interface structures, such as a buffer layer of Si-face graphene [84–86]. According to the microscopic analysis by Yamasue *et al.*, electric polarization arises due to the bonding between a buffer layer and SiC substrate, acting as charge impurities for carrier transport [87]. Thus, electric properties of graphene largely depend on its interface structure.

On the other hand, the presence of an interface layer is also unignorable for optical properties of graphene/SiC system. For instance, charge transfer from SiC to graphene becomes important for SiC photodetector, which utilizes graphene as a transparent electrode [88]. Figure 6-1 shows a band diagram of graphene/SiC system and its photo-excited processes. We assume graphene on an n-doped SiC which is the same as graphene/SiC samples used in Chapters 4 and 5 and these show upward

band bending as described in Fig. 6-1. First, carriers are excited in SiC bulk. Due to the band bending at space charge region, electrons move to the bulk side while holes move to the graphene (Fig. 6-1(a)). As a result of the charge separation, photovoltage emerges at the graphene/SiC interface and cancels the band bending (Fig. 6-1(b)). This is called surface photovoltage (SPV) effect, which is universally observed at a semiconductor surface. Electrons then move back to the surface side due to the diffusion effect (Fig. 6-1(c)). Finally, when an electron overcomes the surface barrier (band bending) by thermal excitation, the electron recombines with a hole at graphene, resulting in the relaxation of SPV. Experimentally, this can be observed as a spectral shift of photoemission spectrum and the charge transfer dynamics can be traced by time-resolved technique.

In this chapter, we investigate the effect of the interface buffer layer on optical properties of graphene/SiC system by time-resolved photoemission spectroscopy utilizing synchrotron radiation (SR) and ultrafast laser.

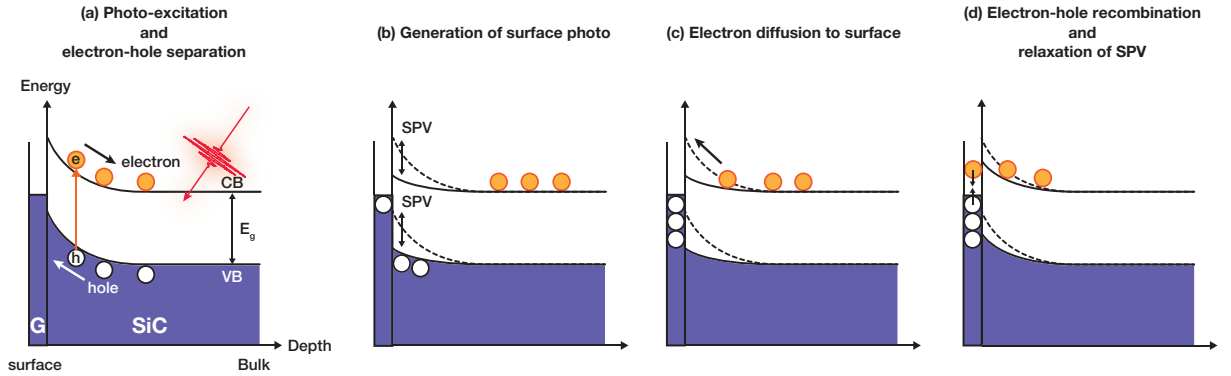


Figure 6-1: Schematic drawing of surface photovoltage effect for graphene/SiC system. (a) Generation of photo-carriers and carrier separation due to the surface band bending. (b) Emergence of surface photovoltage (SPV). (c) Carrier redistribution by diffusion process. (d) Electron-hole recombination results in relaxation of SPV.

## 6.2 Experimental

We prepared epitaxial graphene on SiC(0001) (Si-face graphene) and SiC(000 $\bar{1}$ ) (C-face graphene) for comparison. The sample properties and fabrication methods are

almost similar to the one described in Chap. 4 for Si-face graphene and Chap. 5 for C-face graphene. The samples were annealed at 500 °C for 30 minutes to remove surface contamination.

We performed the time-resolved photoemission experiments at BL07LSU at SPring-8 (see Sec. 3.3.2). For pump light, to excite carriers in SiC, we used second harmonic (3.1 eV) whose energy is close to the band gap of SiC (3.2 eV). For probe light, we set SR energy to 740 eV to sensitively observe photoemission signals of SiC comparable to that of graphene. We set the repetition frequency of the pumping laser to 208 kHz to synchronize with SR period. We performed all measurements at room temperature.

## 6.3 Results and discussion

### 6.3.1 Surface photovoltage effect in Si-face and C-face graphene

Figure 6-2(a,b) shows time-resolved C1s and Si2p spectra of the C-face graphene. Black and colored open circles (lines) represent measured data (fitted results) when pump laser is OFF and ON, respectively. In Fig. 6-2(a), both for graphene (284.5 eV, labeled by G) and SiC (282.5 eV, labeled by SiC) peaks are observed. After the photo-excitation, the spectrum shifts toward high binding energy while the spectral shape is unchanged due to a surface photovoltage effect. The energy shift gradually decreases and goes back to laser OFF position around 100 ps. The same tendency is also observed in Si2p spectra (Fig. 6-2(b)). Figure 6-2(c,d) shows temporal evolution of the SPV shift for C1s and Si2p, respectively, extracted from Fig. 6-2(a,b). We observed almost identical relaxation for C1s and Si2p spectra.

In the same way, Fig. 6-3(a,b) shows time-resolved C1s and Si2p spectra of the Si-face graphene. In Fig. 6-3(a), graphene and SiC peak is not well decoupled within the energy resolution due to the small differences in graphene and SiC binding energies for C1s core levels. Figure 6-3(c,d) shows the temporal evolution of the SPV shift for C1s and Si2p core levels. The SPV relaxation of Si-face graphene is much shorter than that of C-face graphene and relaxes within 10 ns.

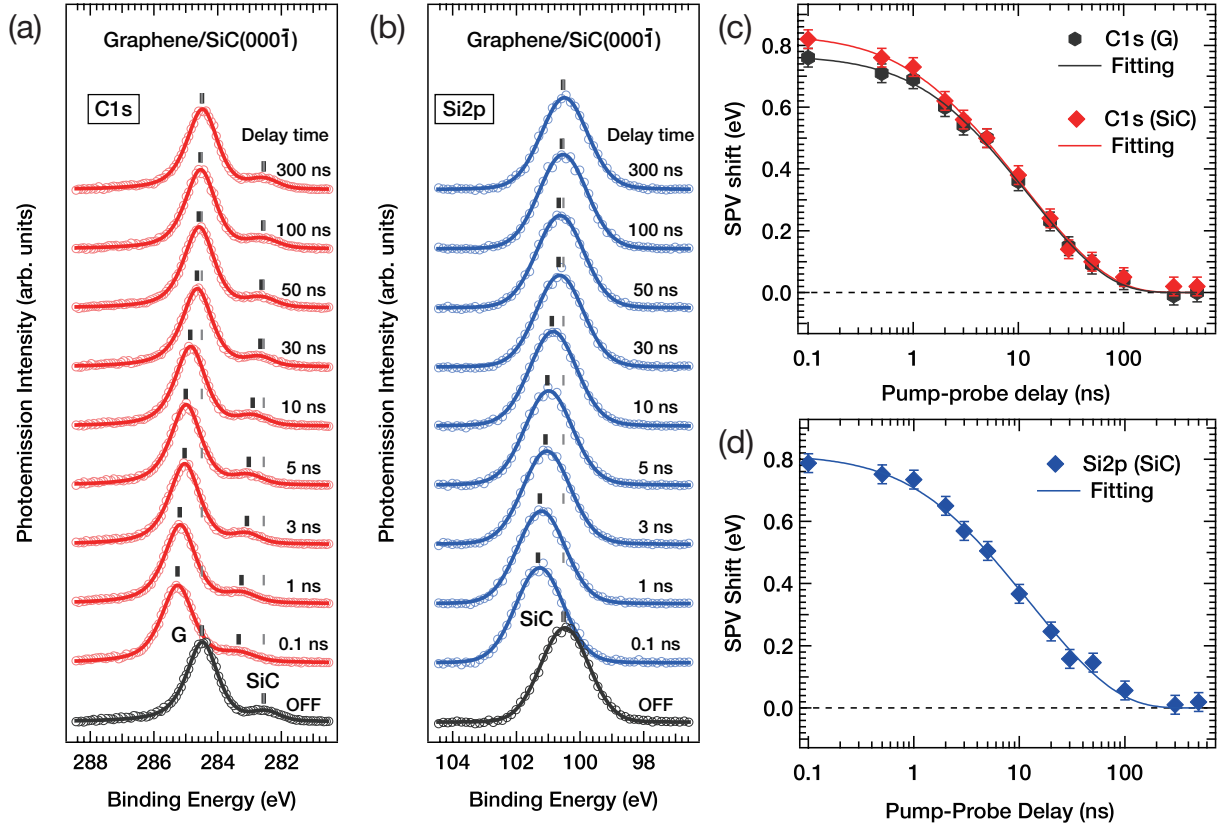


Figure 6-2: Temporal evolution of SPV shift for C-face graphene. Time-resolve photoemission spectra for (a) C1s and (b) Si2p core levels. In (a), graphene peaks (labeled G) and SiC peaks (labeled SiC) were observed due to the large band bending. The spectral shift measured from the laser OFF was extracted and shown as a function of time for (c) C1s and (d) Si2p core levels.

### 6.3.2 Analysis by thermionic emission model

For understanding of these SPV relaxation processes, we assume that photo-excited electrons in SiC bulk side thermally overcome the potential barrier (band bending) at the graphene/SiC interface as shown in Fig. 6-1(d). This process can be well described by the following equation [89,90],

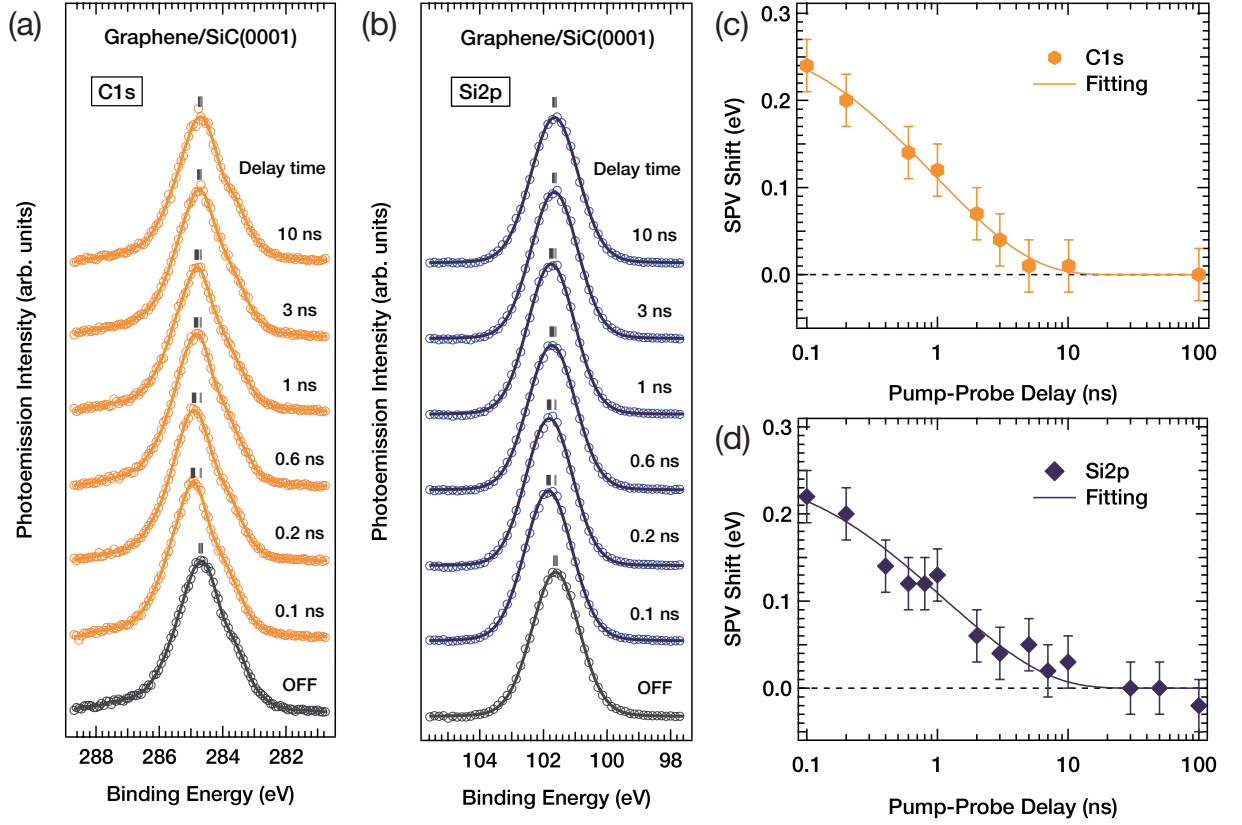


Figure 6-3: Temporal evolution of SPV shift for Si-face graphene. Time-resolve photoemission spectra for (a) C1s and (b) Si2p core levels. The spectral shift measured from the laser OFF was extracted and shown as a function of time for (c) C1s and (d) Si2p core levels.

$$V_{\text{SPV}}(t) = \left| -\eta k_{\text{B}} T \ln \left[ 1 - \left\{ 1 - \exp\left(\frac{-V_0}{\eta k_{\text{B}} T}\right) \right\} e^{-t/\tau} \right] \right|, \quad (6.1)$$

where  $V_{\text{SPV}}(t)$  is the amount of SPV at the delay time  $t$ ,  $\eta$  is an ideality factor in a Schottky diode,  $V_0$  is the initial SPV shift and  $\tau$  is the relaxation time constant when  $V_{\text{SPV}}$  is zero. The experimental results are fitted by Eq. (6.1) as shown in Fig. 6-2 for C-face graphene and Fig. 6-3 for Si-face graphene. The fitting parameters are summarized in Table 6.1 for C-face graphene and Table 6.2 for Si-face graphene.

Table 6.1: List of the fitting parameters for C-face graphene.

|               | C1s (G)         | C1s (SiC)       | Si2p (SiC)      |
|---------------|-----------------|-----------------|-----------------|
| $\eta$        | $10.0 \pm 0.8$  | $9.3 \pm 0.8$   | $9.1 \pm 1.0$   |
| $V_0$ (eV)    | $0.77 \pm 0.01$ | $0.84 \pm 0.02$ | $0.82 \pm 0.02$ |
| $\tau$ (ns)   | $42 \pm 4$      | $46 \pm 6$      | $53 \pm 8$      |
| $\tau_0$ (ps) | 39              | 25              | 24              |

Table 6.2: List of the fitting parameters for Si-face graphene.

|               | C1s (G)         | Si2p (SiC)      |
|---------------|-----------------|-----------------|
| $\eta$        | $3.8 \pm 0.9$   | $3.1 \pm 1.1$   |
| $V_0$ (eV)    | $0.27 \pm 0.02$ | $0.25 \pm 0.04$ |
| $\tau$ (ns)   | $3.1 \pm 0.7$   | $4.2 \pm 1.7$   |
| $\tau_0$ (ps) | 6.3             | 2.1             |

### 6.3.3 Comparison of carrier lifetime and effect of the interface layer

We found that Si-face graphene has shorter carrier lifetime than C-face graphene. However, this comparison is inaccurate because the initial band bending (barrier height for carriers) is different. Therefore, to compare both carrier lifetimes, one has to compensate the initial band bendings. Figure 6-4 describes the energy diagram for graphene/SiC system. The amount of the initial band bendings are obtained from the difference between C1s core position of bulk SiC (284.3 eV [91]) and SiC surface, which are experimentally obtained in this measurement (C-face : 282.5 eV, Si-face : 283.7 eV). We obtained the initial barrier height of 1.8 eV for C-face and 0.6 eV for Si-face graphene. Using these values, the compensated lifetime  $\tau_0$  called ‘‘flat-band lifetime’’ can be defined as,

$$\tau_0 = \tau \exp\left(\frac{-V_0}{\eta k_B T}\right). \quad (6.2)$$

$\tau_0$  describes the lifetime under the flat-band condition (when the initial band bending is zero). We obtained  $\tau_0$  (C-face) = 24 - 39 ps and  $\tau_0$  (Si-face) = 2 - 6 ps as shown in

the bottom lines of Tables 6.1 and 6.2.

As for the flat-band lifetime, we clearly observed large difference. The shorter lifetime in Si-face graphene may mostly come from its interface structure because the bulk properties of SiC are almost identical for both samples, but the interface structure differs substantially. Fig. 6-5 summarizes the expected relaxation pathways for (a) C-face and (b) Si-face graphene. In C-face graphene, electrons and holes recombine through the electronic states of graphene. However, in Si-face graphene, large density of Si dangling-bonds may act as recombination centers for photo-excited electrons and holes. Considering the fact that one-third carbon atoms in the buffer layer bind with Si atoms of the SiC, the density of Si dangling-bonds corresponds to the order of  $10^{15} \text{ cm}^{-2}$ . On the other hand, the density of states of graphene near the Dirac point is in the order of  $10^{12} \text{ cm}^{-2} - 10^{13} \text{ cm}^{-2}$ , that is several orders of magnitude smaller than that of Si dangling-bonds (interface states). Therefore it is plausible that the interface states of the buffer layer promote carrier recombination and determine the relaxation time constant in Si-face graphene.

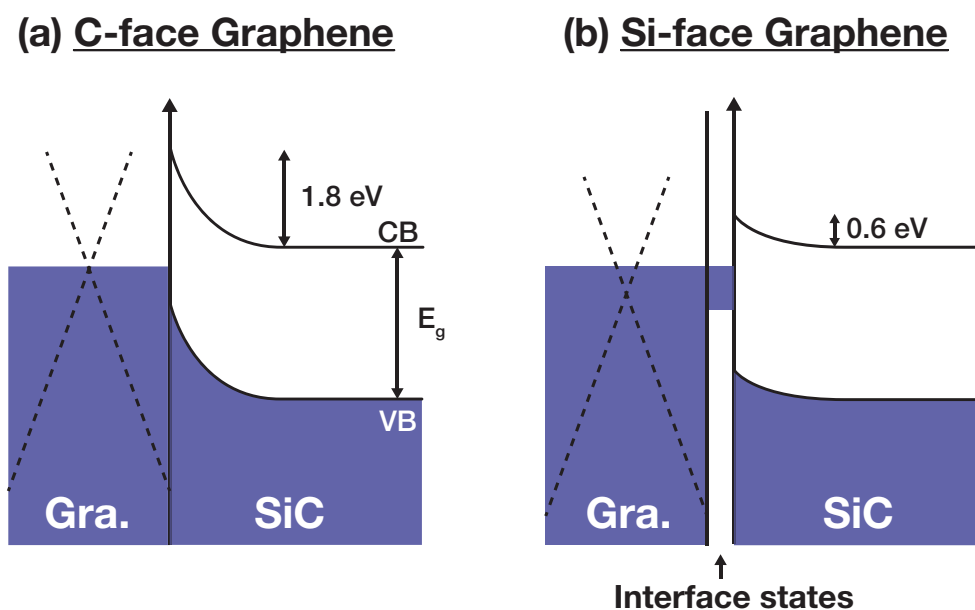


Figure 6-4: Band diagrams for (a) C-face and (b) Si-face graphene. The vertical and horizontal axes show the binding energy and depth, respectively.

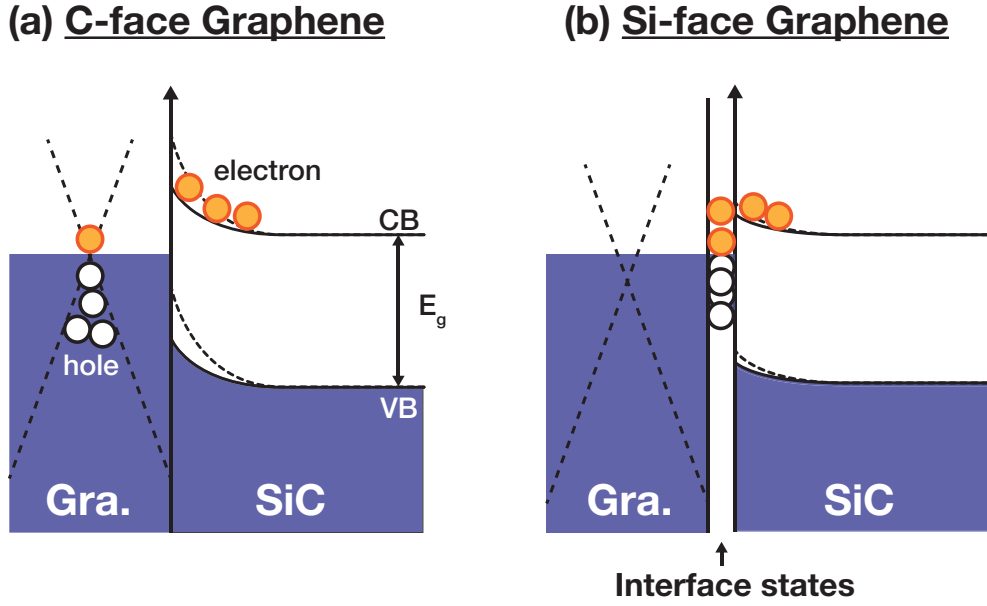


Figure 6-5: Carrier recombination models for (a) C-face and (b) Si-face graphene. The vertical and horizontal axes show the binding energy and depth, respectively.

## 6.4 Conclusion

In this chapter, we investigate the effect of the interface (buffer layer) on optical responses in Si-face graphene. For the comparison, we used Si-face graphene (with buffer layer) and C-face graphene (without buffer layer) and employed time-resolved photoemission spectroscopy on these samples. We successfully observed surface photovoltage effect as a spectral shift of C1s and Si2p core level states. The relaxation time constants are quite different due to the difference between the amount of initial band bendings. By introducing flat-band lifetime, we can clearly observed the difference of the charge transfer dynamics between these samples. The short lifetime observed in Si-face graphene may be attributed to large densities of Si dangling-bonds at the buffer layer, acting as trapping sites for photo-excited electrons and holes. These results are consistent with previous studies reporting that the Si dangling-bonds disturb transport properties of Si-face graphene [84–86].

# Chapter 7

## Summary and future prospect

### 7.1 Summary

In summary, we systematically investigated the whole carrier dynamics in graphene/SiC system.

In Chapter 4, we have observed ultrafast carrier dynamics in an n-type graphene grown on Si-face SiC(0001) for the first time. The observed spectral dynamics reflects both ultrafast changes in the electronic temperature and chemical potential within the time scale of several hundred femtoseconds. The fitting model for the electronic temperature well reproduced the observed spectral features. The obtained electronic temperature was consistent with the previous study by K. J. Tielrooij *et al.* [2], indicating the occurrence of cascade carrier multiplication.

In Chapter 5, we performed time-resolved photoemission measurement on high mobility graphene grown on C-face SiC(000 $\bar{1}$ ). Compared with Si-face graphene as described in Chapter 4, we observed longer carrier lifetime lasting above several picoseconds. To separately analyze each relaxation pathway of photo-excited carrier, we built a comprehensive relaxation model that includes electron–optical-phonon scattering, optical-phonon decay and supercollision. By the fitting of the relaxation model, we reported that the effect of the supercollision cooling is negligible in high mobility graphene whose carrier mobility exceeds  $100,000 \text{ cm}^2 \text{ V}^{-1} \text{ s}^{-1}$  and we can successfully extract the contribution from the cooling rates by electron–optical-phonon scattering.

In Chapter 6, we prepared two graphene samples (C-face and Si-face graphene) with different interface structures and compared charge transfer dynamics of these samples. By comparing the dynamics at flat-band condition, we can clearly find large differences in carrier lifetimes. The shorter carrier lifetime observed in Si-face graphene may be due to Si dangling-bonds at a buffer layer with large density of states, acting as recombination centers which promote the SPV relaxation in Si-face graphene.

## 7.2 Future prospect

In the discussion above, we can know the mechanism of carrier relaxation processes such as carrier–optical-phonon scattering, supercollison, charge transfer dynamics. So far, many studies have been dedicated to carrier dynamics in typical semiconductors (Si, Ge, GaAs, etc.), while research on carrier dynamics in graphene has just started recently. Therefore, as the first comprehensive study of carrier dynamics in graphene/SiC system, this research will help other related studies to understand carrier dynamics in the Dirac Fermions and charge transfer dynamics from a semiconductor to a Dirac material, such as a surface state of a topological insulator and a Weyl semimetal. Our discovery also will help one to design and develop opto-electrical devices utilizing graphene and graphene/semiconductor junctions since carrier dynamics in graphene and charge transfer dynamics between other materials are the most fundamental phenomena in the operation of these devices.

We also mention that, in this thesis, we can not access the detailed mechanism of carrier-carrier scattering, which occur within the time-scale of few femtoseconds. This process is interesting from the aspect of non-equilibrium dynamics, which can not be described by the Fermi-Dirac distribution. It has been theoretically predicted [33, 50, 51] that population inversion can be realized using the gapless Dirac cone, indicating that graphene might be utilized as a laser medium operating at the terahertz (THz) region. Recent trARPES study on Si-face graphene conducted by I. Gierz *et al.* observed the carrier-carrier scattering in graphene with a time resolution of 14 fs.

They observed non-equilibrium dynamics, which can not be described by the Fermi-Dirac distribution function, but they can not observe the population inversion may be because the inherent n-type doping from the SiC substrate maintains large electron density above the Dirac point (small hole density below the Dirac point) and make the population inversion difficult. Based on the result of the previous study, we tried to observe the population inversion in C-face graphene, on which we expected the population inversion due to the electron-hole symmetry originating from its non-doped property. However, we can not observe it may be due to the time resolution is not sufficient to trace such femtosecond dynamics with our time resolution of 80 fs. In the near future, we will again try to observe the carrier-carrier scattering in C-face graphene by improving the time resolution of our HHG system and will completely reveal the whole carrier dynamics of graphene/SiC system from few femtoseconds to nanoseconds time regime.



# Appendix A

## Electronic temperature fitting

Figure A-1 shows some examples of the electronic temperature fittings by using Eq. 5.1 in Sec. 5.3.1. The energy dispersion curves (EDCs) were measured under the pumping fluence of  $1650 \mu\text{J}/\text{cm}^2$  (corresponding to Fig. 5-2(b)) and obtained by integrating photoemission intensities around the  $\bar{K}$  point. The density of states used in Eq. 5.1 were obtained by the following procedures. First, EDCs before  $t = 0$  fs were averaged. Then the averaged EDC was divided by the Fermi-Dirac function  $f(E, T_e = 20 \text{ K})$  which was convolved with the Gauss function  $G(E, \sigma = 250 \text{ meV})$ . Finally, the obtained curve was symmetrized at the Dirac point ( $E = E_F = 0 \text{ eV}$ ) because our graphene sample is non-doped and the density of states should be symmetric with respect to the Dirac point. The inset of Fig. A-1 shows the DOS that we used. By applying this DOS to Eq. 5.1, we successfully reproduced experimental results as illustrated by red circles (raw data) and black solid lines (fittings) in Fig. A-1.

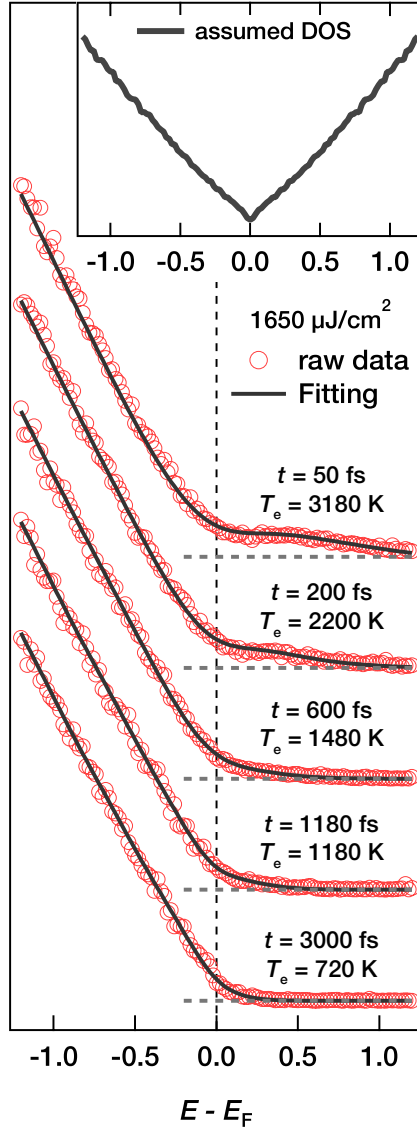


Figure A-1: Examples of the electronic temperature fitting. The raw EDCs (red circles) were measured under the pumping fluence of  $1650 \mu\text{J}/\text{cm}^2$  and at specified delay times. The fitting results by using Eq. 5.1 are illustrated with black solid lines. The inset represents the assumed DOS of the trilayer graphene sample.

# Appendix B

## Derivation of the supercollision cooling rate

We give details of how we derived Eq. (5.4) in Sec. 5.3.2. First, the original expression for the SC cooling rate formulated by Song *et al.* [4] is given in the form

$$\mathcal{J}_{\text{SC}} = A(T_e^3 - T_{ac}^3), \quad A = 9.62 \frac{g^2 \nu^2(E_F) k_B^3}{\hbar k_F l}, \quad (\text{S4})$$

where  $g$  is the electron-phonon coupling constant,  $\nu(E_F)$  is the density of states at the Fermi level, and  $k_F$  is the Fermi velocity measured from the  $\bar{\text{K}}$  point. The electron-phonon interaction originates from the deformation potential interaction,  $g = D/\sqrt{2\rho s^2}$ , where  $s$  denotes the velocity of sound. The density of states at the Fermi energy is approximately represented as  $\nu^2(E_F) \sim n/(\pi\hbar^2 v_F^2)$ , where  $n$  is the carrier density.  $A$  is therefore expressed as,

$$A \approx 2.9 \times 10^{-3} \frac{D^2 n}{k_F l} \quad (\text{W/m}^2\text{K}^3). \quad (\text{S5})$$

Note that in the above equation  $D$  is in eV and  $n$  is in units of  $10^{12} \text{ cm}^{-2}$ . Taking  $k_{\text{F}}l = \sigma(h/2e^2)$  and  $\sigma = ne\mu$ , where  $\sigma$  is the conductivity,  $A$  is expressed as a function of the deformation potential  $D$  and the carrier mobility  $\mu$ ,

$$A \approx 8.8 \times 10^{14} \frac{D^2}{\mu} \quad (\text{eV}/\text{cm}^2\text{K}^3\text{s}), \quad (\text{S6})$$

where  $\mu$  is in units of  $\text{cm}^2 \text{ V}^{-1} \text{ s}^{-1}$ .

# Appendix C

## Details of the fitting parameters

In the rate equations (5.5)–(5.6) in Sec. 5.3.3,  $G_{\text{pump}}$ ,  $\partial t/\partial b$ ,  $M$ , and  $\tau$  are the fitting parameters.  $G_{\text{pump}}$  has a Gaussian form with a full-width at half-maximum of 70 fs:

$$G_{\text{pump}} = G_0 \exp\left[-4\ln 2 \left(\frac{t}{70 \text{ fs}}\right)^2\right], \quad (\text{C1})$$

where  $G_0$  is the scaling parameter (in units of  $\text{J cm}^{-2} \text{s}^{-1}$ ). The fitting parameters for  $T_e$  and  $T_{ph}$  in Figs. 5-2(b–e) in Sec. 5.3.3 are summarized in Table C.1, under  $\mu = 100,000 \text{ cm}^2\text{V}^{-1}\text{s}^{-1}$  and the deformation potential values  $D = 30 \text{ eV}$ .

The total injected energy  $P = \int G_{\text{pump}} dt$  is estimated to be 100, 610, 1190, and 1410  $\text{nJ/cm}^2$  for a pumping fluence of 360, 850, 1100, and 1650  $\mu\text{J/cm}^2$ , respectively. However, an absorption coefficient for graphene on  $\text{SiC}(000\bar{1})$  substrate of 1.3 % per each graphene layer [92] results in the actual injected fluence to be 14, 33, 43, and 64  $\mu\text{J/cm}^2$  for a pumping fluence of 360, 850, 1100, and 1650  $\mu\text{J/cm}^2$ , much larger than what were obtained from the fitting. This large difference may be caused by the absorption saturation, known as Pauli blocking [36]. Similar disagreements between actual applied fluence and observed electronic temperature have been reported in trARPES measurements performed on Si-face p-doped graphene [39] and Si-face n- and p-doped graphene [56].

Table C.1: Fitting parameters used for the calculations of Figs. 5-2(b–e) in Sec. 5.3.3.

| Pump fluence<br>( $\mu\text{J cm}^{-2}$ ) | $G_0$<br>( $\text{J cm}^{-2} \text{s}^{-1}$ ) | $\partial t/\partial b$<br>( $\text{eV nm}^{-1}$ ) | $M$<br>( $\text{cm}^{-2}$ ) | $\tau$<br>(ps) |
|---|---|--|-----------------------------|----------------|
| 360                                       | $1.4 \times 10^6$                             | 100  | $1.6 \times 10^{14}$        | 1.3            |
| 850                                       | $8.2 \times 10^6$                             | 100  | $1.8 \times 10^{14}$        | 1.3            |
| 1100                                      | $16.0 \times 10^6$                            | 100  | $1.6 \times 10^{14}$        | 1.2            |
| 1650                                      | $18.9 \times 10^6$                            | 100  | $1.8 \times 10^{14}$        | 1.3            |

# Appendix D

## Long-delay data

We shall further discuss the carrier relaxation mechanism beyond the delay time of 6 ps. After the electronic and phononic systems reach their thermal equilibrium ( $t > 800$  fs), there are three possible pathways for the cooling of the electronic temperature; specifically, electron–acoustic-phonon scatterings, anharmonic decays of optical phonons, and SCs. However, of these, electron–acoustic-phonon scatterings are very inefficient (with typical decays of nanoseconds [93]) and hence we only consider the other two channels.

In previous studies, debate has arisen over what causes the electronic cooling of graphene after electron–optical-phonon thermalization, and whether SCs [4, 67–69] or optical-phonon decay [59–61], but not both, explains the experimental results. Therefore, taking these previous reports into account, we separately simulated electronic cooling by either SCs or optical-phonon decays. The electronic coolings via these mechanisms are then written as

$$\frac{dT_e}{dt} = -\frac{\mathcal{J}_{SC}}{C_e} \quad (t \geq 1 \text{ ps}), \quad (\text{D1})$$

$$\frac{dT_e}{dt} = -\frac{R^{\text{Net}}\hbar\omega_{\text{ph}}}{C_e} \quad (t \geq 1 \text{ ps}). \quad (\text{D2})$$

For the calculations of net optical-phonon emission rate  $R^{\text{Net}}$  in the Eq. (D2), we used the values of  $T_{\text{ph}}$  obtained by solving Eq. (5.6) in Sec. 5.3.3. Figure D-1(a) and (b) compare the experimental results with the simulated electronic cooling via SCs (Eq. (D1)) and optical-phonon decays (Eq. (D2)), respectively. The values for the fitting parameters used for Fig. D-1(a) are the same as those in Table C.1. Moreover, to fit the experimental results using Eq. (D1) (Fig. D-1(b)), the value of the deformation potential must be 105 eV, for which the value is larger than the reported range of 10–30 eV [67, 75–78]. However, considering the reported fitting value of  $\sim 70$  eV by Betz *et al.* [69], this may not be improbable for the deformation potential of graphene.

We further simulated the electronic cooling beyond  $t > 6$  ps using fitting parameters from Fig. D-1(a) and (b), as seen in Fig. D-1(c). The differences between SC cooling and optical-phonon decay cooling are clear in the long decay regime ( $t > 6$  ps): SCs give a fast decay of  $\sim 20$  ps to the ground state ( $T_e = 20$  K) whereas the decay in electronic temperature with optical-phonon decays has not relaxed after 80 ps. The corresponding carrier densities are also displayed in Fig. D-1(d) obtained using the relation between  $n_e$  and  $T_e$ ; specifically,  $n_e = \pi(k_B T_e)^2 / (6\hbar^2 v_F^2)$ .

In Fig. D-1(e), we present the experimental result of the time-resolved photoemission spectra for the delay range of  $-24$  ps to  $72$  ps (at a pumping fluence of  $360 \mu\text{J}/\text{cm}^2$ ). The averaged spectrum before  $t_0$  is subtracted from all spectra: the scaled red/blue dots indicate the increase/decrease in carrier densities generated by the photo-excitation. The integrated intensities within the dashed rectangle in Fig. D-1(e) are shown in Fig. D-1(f), as a function of the delay time. The simulated result is also shown for comparison. As previously reported in Ref. [58], we note that the sample is pumped again by the reflected light from the back side of the SiC substrate. We observed this multi-pumping signal at least twice as indicated by the red arrows in Fig. D-1(f). Even considering this multi-pumping process, photo-excited carriers have longer lifetimes than the SC expected lifetime of  $\sim 20$  ps. This indicates that, in regard to the electronic cooling of the high mobility graphene, the optical-phonon decay scenario is more likely than SC scenario.

In summary, electronic cooling proceeds with the following steps. Initially the

electronic system rapidly thermalizes with the optical-phonon systems via electron–optical-phonon scattering. As these systems reach their thermal equilibrium, electronic cooling is gradually suppressed with the cooling rate dictated by the decay constant  $\tau$ , which describes anharmonic decay processes of the optical-phonon to acoustic-phonons. Finally the cooling further stagnates because of a bottleneck effect arising from the Dirac point, leading to a long carrier lifetime of more than a hundred picoseconds. This long carrier lifetime indicates a negligible SC influence on electronic cooling in high mobility graphene for which the carrier mobility is above  $100,000 \text{ cm}^2 \text{ V}^{-1} \text{ s}^{-1}$ .

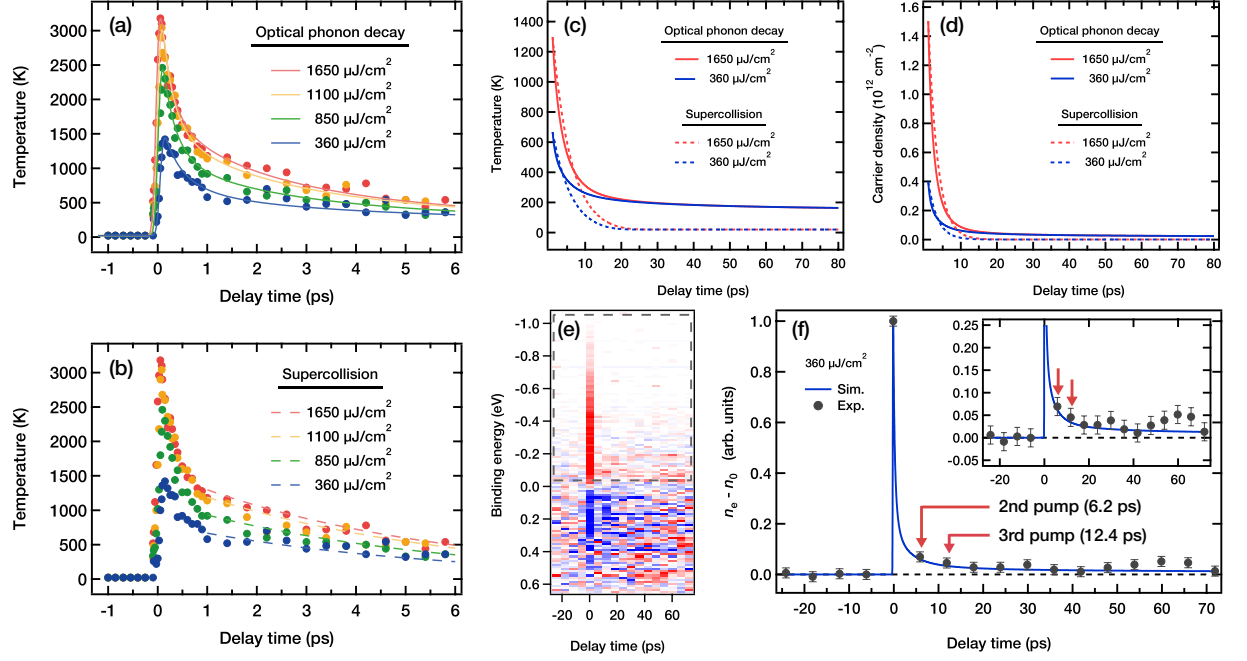


Figure D-1: Comparison of the electronic cooling in the long decay regime: SCs vs optical-phonon decays. (a) Experimentally determined decays of the electronic temperature (colored circles) and simulated results for the optical-phonon decay cooling (colored solid lines) for a specified pumping fluence. The parameters used are listed in Table C.1. (b) Simulated electronic cooling via SCs (colored dotted lines). The values of  $\mu$  and  $D$  are set to  $100,000 \text{ cm}^2 \text{ V}^{-1} \text{ s}^{-1}$  and  $105 \text{ eV}$ , respectively. (c, d) Simulations of  $T_e$  and  $n_e$  beyond  $t \geq 6 \text{ ps}$  for two pumping fluence values. (e) Difference data of time-resolved photoemission spectra for the delay time range of  $-24 \text{ ps}$  to  $72 \text{ ps}$ . The scale red/blue dots indicate increase/decrease from the photoemission intensities at the equilibrium state ( $t \leq 0 \text{ ps}$ ). (f) Comparison of the experimentally determined photo-excited carriers (black circles) and the simulated decay curve (blue solid line) for the pumping fluence of  $360 \mu\text{J}/\text{cm}^2$ . Red arrows indicate the second and third photo-excitation due to the reflected light from the back side of the SiC substrate. The inset presents a magnified plot.

# Publications

## Publication included in this thesis

### Chapter 4

**Observing hot carrier distribution in an n-type epitaxial graphene on a SiC substrate,**

T. Someya, H. Fukidome, Y. Ishida, R. Yoshida, T. Iimori, R. Yukawa, K. Akikubo, Sh. Yamamoto, S. Yamamoto, T. Yamamoto, T. Kanai, K. Funakubo, M. Suemitsu, J. Itatani, F. Komori, S. Shin, and I. Matsuda,  
Applied Physics Letters, **104**, 161103 (2014).

### Chapter 5

**Suppression of supercollision carrier cooling in high mobility graphene on SiC(000 $\bar{1}$ ),**

T. Someya, H. Fukidome, H. Watanabe, T. Yamamoto, M. Okada, H. Suzuki, Y. Ogawa, T. Iimori, N. Ishii, T. Kanai, K. Tashima, B. Feng, S. Yamamoto, J. Itatani, F. Komori, K. Okazaki, S. Shin, and I. Matsuda,  
Physical Review B, **95**, 165303 (2017).

### Chapter 6

**Charge transfer dynamics at graphene/SiC interface studied by time-resolved photoemission spectroscopy,**

T. Someya, H. Fukidome, S. Yamamoto, N. Endo, and I. Matsuda,  
to be submitted for publication.



# Bibliography

- [1] K. S. Novoselov, A. K. Geim, S. V. Morozov, D. Jiang, Y. Zhang, S. V. Dubonos, I. V. Grigorieva, and A. A. Firsov, *Science* **306**, 666 (2004).
- [2] K. J. Tielrooij, J. C. W. Song, S. A. Jensen, A. Centeno, A. Pesquera, A. Z. Elorza, M. Bonn, L. S. Levitov, and F. H. L. Koppens, *Nat. Phys.* **9**, 248 (2013).
- [3] J. C. Johannsen, S. Ulstrup, F. Cilento, A. Crepaldi, M. Zacchigna, C. Cacho, I. C. E. Turcu, E. Springate, F. Fromm, C. Roidel, *et al.*, *Phys. Rev. Lett.* **111**, 027403 (2013).
- [4] J. C. W. Song, M. Y. Reizer, and L. S. Levitov, *Phys. Rev. Lett.* **109**, 106602 (2012).
- [5] E. McCann and V. I. Falko, *Phys. Rev. Lett.* **96**, 086805 (2006).
- [6] A. B. Kuzmenko, E. van Heumen, F. Carbone, and D. van der Marel, *Phys. Rev. Lett.* **100**, 117401 (2008).
- [7] R. R. Nair, P. Blake, A. N. Grigorenko, K. S. Novoselov, T. J. Booth, T. Stauber, N. M. R. Peres, and A. K. Geim, *Science* **320**, 1308 (2008).
- [8] T. Seyller, K. V. Emtsev, K. Gao, F. Speck, L. Ley, A. Tadich, L. Broekman, J. D. Riley, R. C. G. Leckey, O. Rader, *et al.*, *Surf. Sci.* **600**, 3906 (2006).
- [9] K. V. Emtsev, F. Speck, T. Seyller, and L. Ley, *Phys. Rev. B* **77**, 155303 (2008).
- [10] F. Varchon, R. Feng, J. Hass, X. Li, B. N. Nguyen, C. Naud, P. Mallet, J.-Y. Veuillen, C. Berger, E. H. Conrad, *et al.*, *Phys. Rev. Lett.* **99**, 126805 (2007).
- [11] A. Mattausch and O. Pankratov, *Phys. Rev. Lett.* **99**, 076802 (2007).
- [12] A. Mattausch and O. Pankratov, *Mater. Sci. Forum* **556**, 693 (2007).
- [13] J. Ristein, S. Mammadov, and T. Seyller, *Phys. Rev. Lett.* **108**, 246104 (2012).
- [14] K. V. Emtsev, A. Bostwick, K. Horn, J. Jobst, G. L. Kellogg, L. Ley, J. L. McChesney, T. Ohta, S. A. Reshanov, J. Röhrl, *et al.*, *Nat. Mat.* **8**, 203 (2009).
- [15] J. Hass, R. Feng, J. E. Millán-Otoya, X. Li, M. Sprinkle, P. N. First, W. A. de Heer, and E. H. Conrad, *Phys. Rev. B* **75**, 214109 (2007).

- [16] J. Hass, W. A. de Heer, and E. H. Conrad, *J. Phys. : Condens. Matter.* **20**, 323202 (2008).
- [17] M. Sprinkle, D. Siegel, Y. Hu, J. Hicks, A. Tejada, A. TalebIbrahimi, P. L. Fevre, F. Bertran, S. Vizzini, H. Enriquez, *et al.*, *Phys. Rev. Lett.* **103**, 226803 (2009).
- [18] L. I. Johansson, R. Armiento, J. Avila, C. Xia, S. Lorcy, I. A. Abrikosov, M. C. Asensio, and C. Virojanadara, *Sci. Rep.* **4**, 4157 (2014).
- [19] C. Riedl, C. Coletti, T. Iwasaki, A. A. Zakharov, and U. Starke, *Phys. Rev. Lett.* **103**, 246804 (2009).
- [20] S. Hüfner, *Photoemission Spectroscopy : Principles and Applications* (Springer, 2003).
- [21] C. Berglund and W. Spicer, *Phys. Rev.* **136**, 1030 (1964).
- [22] S. Mathias, L. Miaja-Avila, M. M. Murnane, H. Kapteyn, M. Aeschlimann, and M. Bauer, *Rev. Sci. Instrum.* **78**, 083105 (2007).
- [23] L. Dakovski, Y. Li, T. Durakiewicz, and G. Rodriguez, *Rev. Sci. Instrum.* **81**, 073108 (2010).
- [24] Y. Ishida, T. Togashi, K. Yamamoto, M. Tanaka, T. Taniuchi, T. Kiss, M. Nakajima, T. Suemoto, and S. Shin, *Sci. Rep.* **1**, 64 (2011).
- [25] C. L. Smallwood, C. Jozwiak, W. Zhang, and A. Lanzara, *Rev. Sci. Instrum.* **83**, 123904 (2012).
- [26] Y. Tanaka, T. Hara, H. Kitamura, and T. Ishikawa, *Rev. Sci. Instrum.* **71**, 1268 (2000).
- [27] Y. Fukushima, N. Yasuo, J. Kim, H. Murayama, T. Oshima, Y. Tanaka, S. Kimura, H. Kamioka, T. Ishikawa, and M. Takata, *Rev. Sci. Instrum.* **79**, 045107 (2008).
- [28] M. Ogawa, S. Yamamoto, Y. Kousa, F. Nakamura, R. Yukawa, A. Fukushima, A. Harasawa, H. Kondoh, Y. Tanaka, A. Kakizaki, *et al.*, *Rev. Sci. Instrum.* **83**, 023109 (2012).
- [29] P. B. Corkum, *Phys. Rev. Lett.* **71**, 1994 (1993).
- [30] T. Yamamoto, *Development of an EUV laser based time-resolved photoemission spectroscopy system an its application to transition-metal compounds with shallow core levels*, Ph.D. thesis, Tokyo University of Science (2016).
- [31] A. K. Geim, *Science* **324**, 1530 (2009).
- [32] A. H. C. Neto, F. Guinea, N. M. R. Peres, K. S. Novoselov, and A. K. Geim, *Rev. Mod. Phys.* **81**, 109 (2009).

- [33] V. Ryzhii, M. Ryzhii, A. Satou, T. Otsuji, A. A. Dubinov, and V. Y. Aleshkin, *J. Appl. Phys.* **106**, 084507 (2009).
- [34] A. Satou, V. Ryzhii, Y. Kurita, and T. Otsuji, *J. Appl. Phys.* **113**, 143108 (2013).
- [35] T. Winzer, A. Knorr, and E. Malic, *Nano Lett.* **10**, 4839 (2010).
- [36] T. Winzer and E. Malic, *Phys. Rev. B* **85**, 241404 (2012).
- [37] D. Brida, A. Tomadin, C. Manzoni, Y. J. Kim, A. Lombardo, S. Milana, P. R. Nair, K. S. Novoselov, A. C. Ferrari, G. Cerullo, *et al.*, *Nat. Commun.* **4**, 1987 (2013).
- [38] J. C. W. Song, K. J. Tielrooij, and F. H. L. Koppens, *Phys. Rev. B* **87**, 155429 (2013).
- [39] I. Gierz, J. C. Petersen, M. Mitrano, C. Cacho, I. C. E. Turcu, E. Springate, A. Stöhr, A. Köhler, U. Starke, and A. Cavalleri, *Nat. Mat.* **12**, 1119 (2013).
- [40] N. Armbrust, J. Gütde, P. Jakob, and U. Höfer, *Phys. Rev. Lett.* **108**, 056801 (2012).
- [41] S. Gilbertson, T. Durakiewicz, J. Zhu, A. D. Mohite, A. Dattelbaum, and G. Rodriguez, *J. Vac. Sci. Technol. B* **30**, 03D116 (2012).
- [42] K. Ishizaka, T. Kiss, T. Yamamoto, Y. Ishida, T. Saitoh, M. Matsunami, R. Eguchi, T. Ohtsuki, A. Kosuge, T. Kanai, *et al.*, *Phys. Rev. B* **83**, 081104 (2011).
- [43] H. Fukidome, Y. Kawai, F. Fromm, M. Kotsugi, H. Handa, T. Ide, T. Ohkouchi, H. Miyashita, Y. Enta, T. Kinoshita, *et al.*, *Appl. Phys. Lett.* **101**, 041605 (2012).
- [44] T. Someya, H. Fukidome, Y. Ishida, R. Yoshida, T. Iimori, R. Yukawa, K. Akikubo, S. Yamamoto, S. Yamamoto, T. Yamamoto, *et al.*, *Appl. Phys. Lett.* **104**, 161103 (2014).
- [45] S. Passlack, S. Mathias, O. Andreyev, D. Mittnacht, M. Aeschlimann, and M. Bauer, *J. Appl. Phys.* **100**, 024912 (2006).
- [46] Y. Ishida, H. Ohta, A. Fujimori, and H. Hosono, *J. Phys. Soc. Jpn.* **76**, 103709 (2007).
- [47] F. Xia, T. Mueller, Y. M. Lin, A. Valdes-Garcia, and P. Avouris, *Nat. Nanotech.* **4**, 839 (2009).
- [48] T. Mueller, F. Xia, and P. Avouris, *Nat. Photonics* **4**, 297 (2010).
- [49] B. Y. Zhang, T. Liu, B. Meng, X. Li, G. Liang, X. Hu, and Q. J. Wang, *Nat. Commun.* **4**, 1811 (2013).

- [50] V. Ryzhii, V. Mitin, M. Ryzhii, N. Ryabova, and T. Otsuji, *Appl. Phys. Express* **8**, 063002 (2008).
- [51] V. Ryzhii, A. A. Dubinov, T. Otsuji, V. Mitin, and M. S. Shur, *J. Appl. Phys.* **106**, 084507 (2009).
- [52] S. Boubanga-Tombet, S. Chan, T. Watanabe, A. Satou, V. Ryzhii, and T. Otsuji, *Phys. Rev. B* **85**, 035443 (2012).
- [53] T. Watanabe, T. Fukushima, Y. Yabe, S. A. Boubanga-Tombet, A. Satou, A. A. Dubinov, V. Y. Aleshkin, V. Mitin, V. Ryzhii, and T. Otsuji, *New J. Phys.* **15**, 075003 (2013).
- [54] M. Liu, X. Yin, E. Ulin-Avila, B. Geng, T. Zentgraf, L. Ju, F. Wang, and X. Zhang, *Nature* **474**, 64 (2011).
- [55] S. Ulstrup, J. C. Johannsen, F. Cilento, J. A. Miwa, A. Crepaldi, M. Zacchigna, C. Cacho, R. Chapman, E. Springate, S. Mammadov, *et al.*, *Phys. Rev. Lett.* **112**, 257401 (2014).
- [56] J. C. Johannsen, S. Ulstrup, A. Crepaldi, F. Cilento, M. Zacchigna, J. A. Miwa, C. Cacho, R. T. Chapman, E. Springate, F. Fromm, *et al.*, *Nano Lett.* **15**, 326 (2014).
- [57] I. Gierz, M. Mitrano, H. Bromberger, C. Cacho, R. Chapman, E. Springate, S. Link, U. Starke, B. Sachs, M. Eckstein, *et al.*, *Phys. Rev. Lett.* **114**, 125503 (2015).
- [58] S. Ulstrup, J. C. Johannsen, A. Crepaldi, F. Cilento, M. Zacchigna, C. Cacho, R. T. Chapman, E. Springate, F. Fromm, C. Raidel, *et al.*, *J. Phys.: Condens. Matter* **27**, 164206 (2015).
- [59] H. Wang, J. H. Strait, P. A. George, S. Shivaraman, V. B. Shields, M. Chandrashekar, J. Hwang, F. Rana, M. G. Spencer, C. S. Ruiz-Vargas, *et al.*, *Appl. Phys. Lett.* **96**, 081917 (2010).
- [60] J. H. Strait, H. Wang, S. Shivaraman, V. Shields, M. Spencer, and F. Rana, *Nano Lett.* **11**, 4902 (2011).
- [61] K.-C. Lin, M.-Y. Li, L. J. Li, D. C. Ling, C. C. Chi, and J.-C. Chen, *J. Appl. Phys.* **113**, 133511 (2013).
- [62] K.-C. Lin, M.-Y. Li, D. C. Ling, C. C. Chi, and J.-C. Chen, *Phys. Rev. B* **91**, 125440 (2015).
- [63] C. H. Lui, K. F. Mak, J. Shan, and T. F. Heinz, *Phys. Rev. Lett.* **105**, 127404 (2010).
- [64] Y. Liu, L. Zhang, M. K. Brinkley, G. Bian, T. Miller, and T. C. Chiang, *Phys. Rev. Lett.* **105**, 136804 (2010).

- [65] H. Watanabe, T. Kawasaki, T. Iimori, F. Komori, and T. Suemoto, *Chem. Phys. Lett.* **637**, 58 (2015).
- [66] A. Laitinen, M. Oksanen, A. Fay, D. Cox, M. Tomi, P. Virtanen, and P. J. Hakonen, *Nano Lett.* **14**, 3009 (2014).
- [67] T. V. Alencar, M. G. Silva, L. M. Malard, and A. M. de Paula, *Nano Lett.* **9**, 103 (2014).
- [68] M. W. Graham, S.-F. Shi, D. C. Ralph, J. Park, and P. L. McEuen, *Nat. Phys.* **9**, 103 (2013).
- [69] A. C. Betz, S. H. Jhang, E. Pallecchi, R. Ferreira, G. Fève, J. M. Berroir, and B. Plaçais, *Nat. Phys.* **9**, 109 (2013).
- [70] A. Satou, G. Tamamushi, K. Sugawara, J. Mitsushio, V. Ryzhii, and T. Otsuji, *IEEE Trans. Electron Devices* **63**, 3300 (2016).
- [71] J. Jobst, D. Waldmann, F. Speck, R. Hirner, D. K. Maude, T. Seyller, and H. B. Weber, *Phys. Rev. B* **81**, 195434 (2010).
- [72] T. Someya, H. Fukidome, H. Watanabe, T. Yamamoto, M. Okada, H. Suzuki, Y. Ogawa, T. Iimori, N. Ishii, T. Kanai, *et al.*, *Phys. Rev. B* **95**, 165303 (2017).
- [73] S. Piscanec, M. Lazzeri, F. Mauri, A. C. Ferrari, and J. Robertson, *Phys. Rev. Lett.* **93**, 185503 (2004).
- [74] F. Rana, P. A. George, J. H. Strait, J. M. Dawlaty, S. Shivaraman, M. Chandrashekar, and M. G. Spencer, *Phys. Rev. B* **79**, 115447 (2009).
- [75] K. Sugihara, *Phys. Rev. B* **28**, 2157 (1983).
- [76] K. I. Bolotin, K. J. Sikes, J. Hone, H. L. Stormer, and P. Kim, *Phys. Rev. Lett.* **101**, 096802 (2008).
- [77] D. K. Efetov and P. Kim, *Phys. Rev. Lett.* **105**, 256805 (2010).
- [78] C. R. Dean, A. F. Young, I. Meric, C. Lee, L. Wang, S. Sorgenfrei, K. Watanabe, T. Taniguchi, P. Kim, K. L. Shepard, *et al.*, *Nat. Nanotech.* **5**, 722 (2010).
- [79] D. Sun, C. Divin, C. Berger, W. A. de Heer, P. N. First, and T. B. Norris, *Phys. Status Solidi C* **8**, 1194 (2011).
- [80] N. Bonini, M. Lazzeri, N. Marzari, and F. Mauri, *Phys. Rev. Lett.* **99**, 176802 (2007).
- [81] N. García, P. Esquinazi, J. Barzola-Quiquia, B. Ming, and D. Spoddig, *Phys. Rev. B* **78**, 035413 (2008).
- [82] A. Stange, C. Sohrt, L. X. Yang, G. Rohde, K. Janssen, P. Hein, L.-P. Oloff, K. Hanff, K. Rossnagel, and M. Bauer, *Phys. Rev. B* **92**, 184303 (2015).

- [83] S. Butscher, F. Milde, M. Hirtschulz, E. Malić, and A. Knorr, *Appl. Phys. Lett.* **91**, 203103 (2007).
- [84] S. Tanabe, M. Takamura, Y. Harada, H. Kageshima, and H. Hibino, *Appl. Phys. Express* **5**, 125101 (2012).
- [85] S. Tanabe, M. Takamura, Y. Harada, H. Kageshima, and H. Hibino, *Jpn. J. Appl. Phys.* **53**, 04 (2014).
- [86] F. Maeda, S. Tanabe, S. Isobe, and H. Hibino, *Phys. Rev. B* **88**, 085422 (2013).
- [87] K. Yamasue, H. Fukidome, K. Funakubo, M. Suemitsu, and Y. Cho, *Phys. Rev. Lett* **114**, 226103 (2015).
- [88] V. Chava, S. Omar, G. B. S. Shetu, J. Andrews, T. Sudarshan, and M. Chandrashekar, *Appl. Phys. Lett.* **108**, 043502 (2016).
- [89] B. F. Spencer, D. M. Graham, S. J. O. Hardman, E. A. Seddon, M. J. Cliffe, K. L. Syres, A. G. Thomas, S. K. Stubbs, F. Sirotti, M. G. Silly, *et al.*, *Phys. Rev. B* **88**, 195301 (2013).
- [90] M. Ogawa, S. Yamamoto, R. Yukawa, R. Hobara, C.-H. Lin, R.-Y. Liu, S.-J. Tang, and I. Matsuda, *Phys. Rev. B* **87**, 235308 (2013).
- [91] S. A. Reshanov, K. V. Emtsev, F. Speck, K.-Y. Gao, T. K. Seyller, G. Pensl, and L. Ley, *Phys. Status Solidi B* **245**, 1369 (2008).
- [92] A. Drabińska, K. Grodecki, W. Strupiński, R. Bożek, K. P. Korona, A. W. ek, R. Stępniewski, and J. M. Baranowski, *Phys. Rev. B* **81**, 245410 (2010).
- [93] R. Bistritzer and A. H. MacDonald, *Phys. Rev. Lett.* **102**, 206410 (2009).